

**Photoelectron and photoion spectroscopy of atoms,
nanoparticles, and nanoplasmas irradiated with
strong femtosecond laser fields**

by

Daniel D. Hickstein

M.Phil, University of Cambridge, 2008

B.A., Pomona College, 2007

A thesis submitted to the
Faculty of the Graduate School of the
University of Colorado in partial fulfillment
of the requirements for the degree of
Doctor of Philosophy
Program in Chemical Physics

2014

This thesis entitled:
Photoelectron and photoion spectroscopy of atoms, nanoparticles, and nanoplasmas irradiated
with strong femtosecond laser fields
written by Daniel D. Hickstein
has been approved for the Program in Chemical Physics

Henry C. Kapteyn

David M. Jonas

Date _____

The final copy of this thesis has been examined by the signatories, and we find that both the content and the form meet acceptable presentation standards of scholarly work in the above mentioned discipline.

Hickstein, Daniel D. (Ph.D., Chemical Physics)

Photoelectron and photoion spectroscopy of atoms, nanoparticles, and nanoplasmas irradiated with strong femtosecond laser fields

Thesis directed by Professors Margaret M. Murnane and Henry C. Kapteyn

Modern femtosecond lasers can produce pulses of light that are shorter than the vibrational periods in molecules and have electric fields stronger than the Coulomb field that binds electrons in atoms. These short-pulse lasers enable the observation of chemical reactions, the production of attosecond bursts of high-energy photons, and the precision-machining of solid materials with minimal heat transport to the material. In this thesis, I describe three experiments that provide new insight into strong-field ($\sim 10^{14}$ Watts/cm²) femtosecond laser-matter interactions in three important regimes. First, I discuss the strong-field ionization of gas-phase atoms, identify a new structure in the photoelectron angular distribution of xenon gas, and explain this structure by developing an intuitive wave interference model. Second, I describe a new method to perform photoelectron and photoion spectroscopy on single, isolated nanoparticles and demonstrate this technique by observing the directional ion ejection that takes place in the laser ablation of nanostructures. Finally, I present the first experimental observations of shock wave propagation in nanoscale plasmas. These findings will guide future efforts to probe the structure and dynamics of atoms and molecules on the femtosecond timescale, design nanomaterials that enhance light on the subwavelength scale, and produce high-energy ions from plasmas.

Acknowledgements

The work in this thesis would not have been possible if it were not for the assistance of many, many people. My heartfelt thanks goes

- To the best family ever: my parents, Mary and Dennis, and my brother, Matt.
- To Laura Johnson for her love and support.
- To Margaret Murnane and Henry Kapteyn for being the best advisors anyone could ask for.
- To my mentors in the Kapteyn–Murnane Group, especially Predrag Ranitovic, Xibin Zhou, and Wei Xiong.
- To Curtis Stevens, Katie Johnson, and Daisy Johnson for their support and company on the trails.
- To my labmates in the KM Group, past and present, especially Jennifer Ellis, Franklin Dollar, Chengyuan Ding, Paul Arpin, Matt Seaberg, Dan Adams, Tenio Popmintchev, Tory Carr, Craig Hogle, Ellen Keister, Robynne Lock, Chris Mancuso, Bosheng Zhang, Tingting Fan, Ming-Chang Chen, Bill Peters, Patrik Grychtol, Michael Gerrity, Wen Li, Chan La-o-vorakiat, Stefan Witte, and Stefan Mathias.
- To the staff of the JILA Instrument Shop, who do the impossible nearly every day, especially Hans Green, David Alchenberger, Blaine Horner, Kim Hagen, Ariel Paul, Todd Asnicar, and Kels Detra.
- To the JILA Computing Team, especially J. R. Raith, who magically make dealing with a room full of angry Windows computers tolerable.

- To Brad Baxley for his beautiful illustrations that are scattered throughout this thesis.
- To our talented collaborators, who made this work possible, especially Kyle Schnitzenbaumer, Molly Wilker, Gordana Dukovic, Brett Palm, Jose Jimenez, Pedro Campuzano–Jost, Jim Gaffney, Mark Foord, Steve Libby, Ymkje Huisman, Marc Vrakking, Xiao-Min Tong, Ofer Kfir, Oren Cohen, Avner Fleischer, Luis Miaja-Avila, Carlos Hernandez-Garcia, Andreas Becker, and George Petrov.
- To Mikhail Ryazanov and Hanna Reisler at USC for their help with the BASEX Abel transform.
- To our wonderful undergraduate students: Robbie Wright, Jennifer Li, Ethan Scott, Maithreyi Gopalakrishnan, and Leigh Martin.
- To the staff at KMLabs who were always quick to provide advice and assistance, especially Xiaoshi Zhang, Mike Walls, Daisy Raymondson, Neil Anderson, and Sterling Backus.
- To professors David Jonas, Agnieszka Jaron-Becker, Ralph Jimenez, W. Carl Lineberger, for serving on my thesis committee and for their help and advice throughout my years at JILA.
- To the professors at Pomona College that inspired me to pursue a PhD: Dan O’Leary, Wayne Steinmetz, and Alfred Kwok.
- To my previous research mentors, who taught me how to work in a lab: Jacqui Cole (Cambridge), Dan O’Leary (Pomona College), Liz Donley (NIST), Brant Weinstein (NICHD), and Paul Liu (NHGRI).
- To Jason Haas, Hillary Smith, and Julie Phillips, for teaching me how to write.

Contents

1	Introduction	1
1.1	Motivation	1
1.1.1	Seeing the invisible	1
1.1.2	Femtosecond lasers	2
1.1.3	The velocity map imaging (VMI) spectrometer	3
1.1.4	Nanoparticles	4
1.2	Electron dynamics in strong femtosecond laser fields	7
1.2.1	The three step model	7
1.2.2	Strong field ionization with mid-IR fields	9
1.3	Localized light absorption in nanoparticles	10
1.4	Shock waves in nanoplasmas	11
2	Apparatus and methods	12
2.1	Experimental summary	12
2.2	Femtosecond laser system	12
2.2.1	Chirped pulse amplification	12
2.2.2	Light sources	14
2.2.3	Optical parametric amplifier (OPA)	14
2.2.4	Delay line	15
2.3	Velocity map imaging spectrometer	16

2.3.1	Concept and history	16
2.3.2	Theory	17
2.3.3	Implementation	19
2.3.4	Abel transform	24
2.4	Nanoparticle aerosol source	25
2.4.1	Atomizer	25
2.4.2	Electrostatic classifier	27
2.4.3	Aerodynamic lens	27
2.4.4	Light scattering	28
2.4.5	Single particle experiments	29
3	Electron dynamics in strong field ionization	30
3.1	Abstract	31
3.2	Introduction	31
3.2.1	Zeptosecond waveforms	31
3.2.2	HHG and SFI in the mid-IR	32
3.3	Experiment	33
3.4	Photoelectron angular distributions from UV to mid-IR	35
3.5	Plane-spherical wave model	35
3.6	Inner spider structures	39
3.7	Measurement of the quantum tunnel distance	42
3.8	Conclusion	43
4	Plasma Explosion Imaging	45
4.1	Abstract	46
4.2	Introduction	46
4.2.1	Background	46
4.2.2	Experimental approach	48

4.2.3	Summary of findings	50
4.3	Results and Discussion	50
4.3.1	Overview	50
4.3.2	Electron microscopy	51
4.3.3	Photoion spectroscopy	53
4.4	Case studies of nanoscale light enhancement	57
4.4.1	NaCl crystals: nanofocusing in dielectric nanomaterials	57
4.4.2	TiO ₂ nanoclusters: light interaction with a particle ensemble	58
4.4.3	50 nm gold nanoparticles: field enhancement at the surface	59
4.4.4	17 nm gold nanospheres: asymmetric hot-spots	60
4.5	Future directions	60
4.6	Summary	61
5	Shock Waves in Nanoplasma	62
5.1	Abstract	63
5.2	Introduction	63
5.3	Experiment	64
5.4	Results and Discussion	65
5.5	Hydrodynamic Simulations	69
5.6	Conclusion	71
6	Conclusion and outlook	72
6.1	Overview	72
6.2	Outlook	72
6.2.1	Strong-field ionization of gas-phase atoms and molecules	72
6.2.2	Plasma Explosion Imaging	74
6.2.3	Shock waves	75
6.3	Future Directions	76

6.3.1	Extreme ultraviolet probe of nanomaterials	76
6.3.2	Magnetron sputtering nanoparticle source	77
6.4	Conclusion	79
A	Multiple Scattering Structures Appendix	81
A.1	Overview	81
A.2	Details of the Plane-Spherical Wave Model	81
A.3	Calculating the modulation frequency	83
A.4	Extracting the experimental multiple rescattering cutoff	85
A.5	Intensity dependence	86
B	Plasma Explosion Imaging Appendix	89
B.1	Overview	89
B.2	Methods	89
B.2.1	Photoion spectroscopy and aerosol generation	89
B.2.2	Materials	90
B.2.3	Transmission electron microscopy	90
B.2.4	Finite-difference time-domain (FDTD) simulations	91
B.3	Photoelectron Distributions	91
B.4	Plasma Explosion Mass Spectrometry	93
B.4.1	Mass spectrum of a single nanoparticle	93
B.4.2	Time-of-flight experimental details	94
C	Shock Waves in Nanoplasmas Appendix	96
C.1	Overview	96
C.2	Experimental Details	97
C.3	Dependence of shock formation on particle size	98
C.4	Effect of laser intensity on nanoplasma formation	99

C.5 Time-dependence of shock formation rate	101
C.6 Hydrodynamic simulations	102
C.7 Plasma quasi-neutrality	105
References	107

Figures

1.1	Edgerton’s “Bullet Through Apple”	2
1.2	Various sizes of CdSe quantum dots	5
1.3	The three-step model of high harmonic generation (HHG)	8
2.1	Femtosecond light sources from the UV to the mid-IR.	15
2.2	A typical femtosecond pump-probe experiment	16
2.3	Schematic of the velocity map imaging (VMI) spectrometer	19
2.4	Photograph of the VMI electrodes	21
2.5	Alignment of the gas jet to the skimmer	22
2.6	The atomizer and differential mobility analyzer (DMA)	26
2.7	The aerodynamic lens	28
3.1	Illustration of photoelectron rescattering	30
3.2	Summary of multiple rescattering	34
3.3	The plane-spherical wave (PSW) model	36
3.4	Comparison of experiment, simulations, and simple PSW theory	37
3.5	Multiple scattering of the electron with the ion	40
3.6	Measurement of the quantum tunnel distance	43
4.1	Illustration of plasma explosion imaging (PEI) in a single nanoparticle	45
4.2	Summary of PEI in four nanostructures	47
4.3	Apparatus for PEI	49

4.4	Electron microscopy of nanoparticles collected at the interaction region	52
4.5	Photoion angular distributions (PADs) from individual nanostructures	55
4.6	Position of the centers of mass of the PADs	56
4.7	Finite-difference time-domain (FDTD) simulations	57
4.8	Summary of nanoscale light absorption revealed through PEI	61
5.1	Illustration of laser-driven shock wave in a nanoplasma	62
5.2	Apparatus for imaging shock waves in individual nanoplasmas	65
5.3	Experimental observation of shock waves in individual nanoplasmas	66
5.4	Control of shock wave formation using two laser pulses	68
5.5	Mechanism for shock formation, revealed by hydrodynamic simulations	70
6.1	Photoelectrons from circularly polarized driving lasers	74
6.2	Schematic of the NanoGen50.	78
A.1	Electron trajectories that produce interference structures.	84
A.2	Procedure for determining the inner-spider cutoff	86
A.3	The positions of the inner-spider cutoffs.	87
A.4	Effect of the laser intensity on inner spider structures	88
B.1	Comparison of photoelectron and photoion distributions from single nanoparticles	93
B.2	Mass spectrum of a single nanoparticle explosion	95
C.1	Nanoplasma explosions of NaCl nanoparticles with a single pulse.	98
C.2	Effect of particle diameter of the formation of shock waves.	99
C.3	Ion yield and shock wave formation versus laser intensity.	100
C.4	The fraction of ions in the shock controlled with two-pulse delay.	101
C.5	HYDRA simulations at various two-pulse delays.	102
C.6	Scaling of the shock with laser intensity using HYDRA.	103

List of Abbreviations

ATI	Above Threshold Ionization
ADK	Ammosov, Delone, and Krainov [1] – an estimate of tunnel ionization rates
BBO	Beta Barium Borate – a nonlinear crystal
CCD	Charge-Coupled Device – the type of sensor in many digital cameras
CoM	Center of Mass
CPA	Chirped Pulse Amplification
DMA	Differential Mobility Analyzer - A device that produces a size-selected aerosol
EUV	Extreme Ultraviolet (light)
eV	Electron Volt - unit of energy, $1 \text{ eV} \approx 1.602 \times 10^{-19} \text{ J}$
FDTD	Finite-Difference Time-Domain – a simulation method
HHG	High-Harmonic Generation – a method for producing EUV and SXR light
HYDRA	A radiation hydrodynamic code developed at Livermore National Lab
IR	Infrared (light)
JILA	The Institute formerly known as the Joint Institute for Laboratory Astrophysics
MCP	Microchannel Plate – a detector of electrons, ions, and photons
OPA	Optical Parametric Amplifier
PAD	Photoelectron (or Photoion) Angular Distribution
PEI	Plasma Explosion Imaging
PES	Photoelectron Spectroscopy
psig	pounds per square inch gauge – a unit of pressure in excess of atmospheric pressure

PSW	Plane Spherical Wave – a model for SFI presented in this thesis
PVP	Polyvinylpyrrolidone – an organic compound
SFI	Strong Field Ionization
SXR	Soft X-ray
TDSE	Time-Dependent Schrödinger Equation
ToF	Time of Flight
UV	Ultraviolet
VMI	Velocity Map Imaging
VMIS	Velocity Map Imaging Spectrometer

Thesis Outline

This thesis describes three studies, each based on a different publication, and each presented in a separate chapter:

- Chapter 3 is based on a 2012 Physical Review Letter [2] titled “Direct Visualization of Laser-Driven Electron Multiple Scattering and Tunneling Distance in Strong-Field Ionization” and describes the strong-field ionization of atomic gases using femtosecond laser pulses ranging from 262 to 2000 nm. Additional information is presented in Appendix A.
- Chapter 4 is based on a 2014 ACS Nano Article [3] titled “Mapping Nanoscale Absorption of Femtosecond Laser Pulses using Plasma Explosion Imaging” and discusses how strong laser pulses can induce a directional ion ejection in nanostructures, revealing the absorption of femtosecond pulses on the nanometer scale. Additional information presented in Appendix B.
- Chapter 5 is based on a 2014 Physical Review Letter [4] titled “Observation and Control of Shock Waves in Individual Nanoplasmas” and presents an experiment where two laser pulses are used to convert a nanoparticle into a rapidly expanding nanoplasma and subsequently drive a shock wave through the expanding nanoplasma. Additional information is presented in Appendix C.

The introduction (Chapter 1) provides a general motivation for femtosecond laser science and nanoscience (Section 1.1) and a brief motivation for each study (Sections 1.2, 1.3, and 1.4). Chapter 2 provides a detailed discussion of the apparatus and techniques used in this thesis, describing the femtosecond laser systems (Section 2.2), the Velocity Map Imaging Spectrometer (Section 2.3), and

the nanoparticle aerosol source (Section 2.4). After the studies presented in Chapters 3, 4, and 5, Chapter 6 provides a brief synopsis of the findings and presents ideas for future experiments that build upon the developments made in this Thesis. Appendices A, B, and C present additional information relating to Chapters 3, 4, and 5 respectively.

Additional works

In addition to the works highlighted in this thesis, the author was a co-author on the following studies that will be covered in the theses of other JILA graduate students.

- A complete description of the 2013 Nano Letter [5] titled “Photoelectron Spectroscopy of CdSe Nanocrystals in the Gas Phase: A Direct Measure of the Evanescent Electron Wave Function of Quantum Dots” will be presented in the thesis of Jennifer Ellis.
- A complete description of a submitted paper [6] titled “Strong Field Ionization Tomography with Two-color Circularly Polarized Femtosecond Laser Fields” will be presented in the thesis of Chris Mancuso.
- A complete description of a submitted paper [7] titled “Electron transfer dynamics in gas-phase and solvated quantum dots” will be presented in the thesis of Jennifer Ellis.
- A complete description of a forthcoming paper titled “Extreme ultraviolet photoelectron spectroscopy of nanoparticles” will be presented in the thesis of Jennifer Ellis.

Copyright

All images, figures, and illustrations are the work of the author unless otherwise noted. Text and figures are Copyright 2014 Daniel Hickstein unless noted.

Chapter 1

Introduction

1.1 Motivation

1.1.1 Seeing the invisible

One goal of science is to take things that are invisible to human perception and make them visible. This takes many forms, from using statistics to “see” the evolution of genetic diseases across many generations, to using an electron microscope to inspect the nanometer-scale (10^{-9} m) structures that provide the color of a butterfly wing [8]. Objects and phenomena can be “invisible” to human perception for many different reasons. For example, the object may be too small to see with the naked eye, or it may be too large to observe all at once. Alternatively, a process may be difficult to observe because it occurs on a timescale much longer than a human lifetime, or takes place in a split second. The use of new technology to observe such otherwise invisible phenomena allows for breakthroughs in our understanding.

A particularly striking example of how scientists use technological advances to visualize the natural world in revolutionary ways is the work of Harold Edgerton in the 1930s through the 1960s. Among numerous innovations, Edgerton pioneered the use of the xenon flashlamp for high-speed photography. The xenon flashlamp provides bursts of light lasting only 1 microsecond (μs), several orders of magnitude faster than the fastest mechanical shutter. Since a rifle bullet only travels ~ 1 mm per μs , this flashlamp allowed Edgerton to take photographs of speeding bullets impacting various objects as if they were motionless (Figure 1.1).

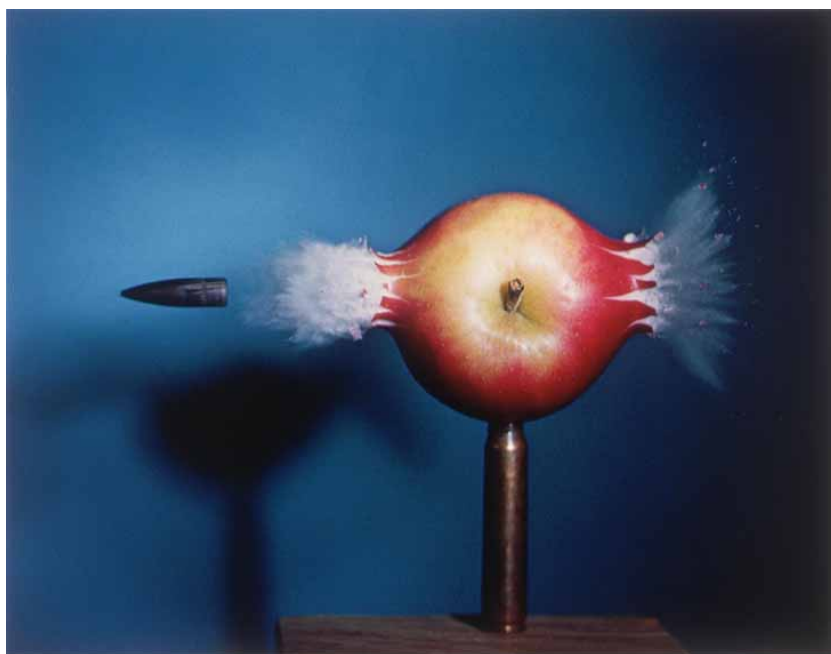


Figure 1.1: **Edgerton’s iconic 1964 photograph “Bullet Through Apple” [9]**. Using a carefully timed xenon flashlamp in a completely dark room, Harold Edgerton was able to photograph a rifle bullet passing through an apple with microsecond time resolution. ©2010 MIT. Courtesy of MIT Museum

1.1.2 Femtosecond lasers

Femtosecond lasers generate bursts of light with durations on the timescale of a few 10s of femtoseconds ($1 \text{ fs} = 10^{-15} \text{ s}$). Thus, they allow for the examination of processes that are $\sim 100,000,000$ times shorter than those that can be resolved using the xenon flashlamp that produced the “Bullet Through Apple” photograph. Light moves only $\sim 300 \text{ nm}$ per fs, meaning that even an object moving at the speed of light would be blurred by only $3 \mu\text{m}$ when photographed using a 10 fs pulse from a femtosecond laser.¹ Thus, a femtosecond laser allows any macroscopic object to be photographed with negligible motion blur, even if it is moving extremely fast. Indeed, the speed of light implies that the only processes that can fully utilize the impressive time resolution of a femtosecond laser pulse occur on the nanometer length scale or smaller. For example, a carbon–oxygen single-bond ($\sim 145 \text{ pm}$) has a vibrational stretching period of $\sim 30 \text{ fs}$, indicating that femtosecond lasers can be used to study chemical reactions on a timescale comparable to the movements of nuclei. Electrons

¹ Of course, this ignores relativistic effects.

(being less massive than nuclei) can move somewhat faster, but electron motion on the nanometer scale is another phenomena that can now be observed with femtosecond laser pulses.

Because a femtosecond laser produces light in such short bursts, the light field can also be extremely intense, allowing unusual regimes of laser-matter interactions to be studied using table-top scale devices. When focused, a 40 fs pulse from an amplified titanium-doped sapphire (Ti:sapphire) laser can easily reach intensities in excess of 10^{14} W/cm², an intensity regime where the electric field of the laser pulse becomes comparable to the Coulomb field binding electrons to atoms. These intense femtosecond laser pulses enable fascinating and useful phenomena on the nanoscale. For instance, electrons can be ripped from atoms, accelerated in the laser field, and returned to the atom to create high-energy photons in a process called high harmonic generation (HHG, Section 1.2.1) [10–12]. In addition, high-density plasmas may be generated on the timescale of only a few femtoseconds. This thesis focuses on finding new methods to use femtosecond lasers to study the motion of electrons and nuclei that take place when intense femtosecond laser fields irradiate atoms, nanoparticles, and nanoplasmas.

1.1.3 The velocity map imaging (VMI) spectrometer

Unfortunately, one cannot simply take a photograph of objects on the nanometer or picometer scale (see Section 1.3). In order to observe electron and chemical dynamics in materials, we utilize a velocity-map imaging (VMI) spectrometer, a device that detects the momentum of the electrons and ions that are generated when a laser pulse irradiates an atom, molecule, or nanoparticle. The VMI spectrometer was developed nearly 20 years ago and has proven itself as a straightforward, yet highly flexible, tool for observing both chemical and electronic structure. The VMI spectrometer can record the complete momentum distribution of either photoelectrons or photoions, which provides the flexibility to study a wide range of processes, including the attosecond dynamics of electrons driven by a strong laser field (Chapter 3), ion ejection in laser-ablated nanoparticles (Chapter 4), and the picosecond dynamics of shock waves propagating through a dense laser-produced nanoplasma (Chapter 5).

Though the VMI spectrometer can now be considered a mature technology, the field has been re-invigorated by utilizing new light sources and new samples. This thesis presents three different examples of how combining femtosecond light sources and nanostructured targets with a VMI spectrometer led to new observations. First (Chapter 3), we record the photoelectron spectra from atoms and molecules using strong-field femtosecond lasers with wavelengths ranging from 266 nm to 2000 nm. While each of these wavelengths has been explored individually in the VMI, this constitutes the first efforts to systematically study the effects of strong laser fields across such a large wavelength range. Second, we replace the typical gas-jet source with a nanoparticle aerosol source that can inject high-concentration nanoparticles into the interaction region of the VMI spectrometer while minimizing the amount of background gas present. This technique allows us to study the directionality in ion ejection from nanoparticles of different compositions and morphologies (Chapter 4). Third, we use the VMI to explore the regime of single, expanding nanoplasmas (Chapter 5) by using one femtosecond laser pulse to transform a nanoparticle into a nanoplasma and a second laser pulse to drive shock waves through the nanoplasma.

1.1.4 Nanoparticles

1.1.4.1 Nanomaterials: a frontier of science and technology

Historically, technologies have existed to observe matter on the scale of bulk materials as well as on the scale of atoms and molecules. However, the nanometer scale has remained largely elusive to measurement and manipulation until recently, where technological advances have made it possible to observe and fabricate materials on the nanometer scale. The nanoscale is especially interesting, because this is where materials undergo the transition from atomic- or molecular-like properties to bulk-like properties, a regime that is not completely understood and currently represents a frontier of science. Often, the properties of nanomaterials are somewhere between the properties of the constituent atoms and the bulk material, but frequently the nanomaterials exhibit properties that are entirely unexpected – and potentially very useful!

For example, a macroscopic sphere of gold has the usual color and luster that we expect from a

piece of bulk gold. However, a solution of 50-nm diameter gold spheres suspended in water is not gold colored, but instead appears a deep blood-red color. In a more spectacular example, nanocrystals of semiconductor materials (quantum dots or QDs) fluoresce vivid colors under ultraviolet illumination and the color of the fluorescence can be tuned, simply by varying the size of the nanoparticles (Figure 1.2), which is easily achieved during synthesis. Their unusual properties have made nanomaterials prime candidates to enable breakthrough technologies as diverse as inexpensive photovoltaic panels, cancer treatments, and efficient catalysts.



Figure 1.2: **Cadmium selenide quantum dots (CdSe QDs)**. (left) Each vial contains the same chemical composition (CdSe QDs and toluene), but the different sizes cause the nanocrystals to fluoresce different colors. The bandgap increases with decreasing particle size, so the vials on the left contain the smallest QDs (largest bandgap) and the vials on the right contain the largest QDs (smallest bandgap). Image courtesy of NN-Labs Inc. (right) An illustration of CdSe quantum dots shows the individual atoms clustered into faceted nanocrystals.

1.1.4.2 Nanoparticles in vacuum

Motivated by the unusual (and, in many cases, unexplained) properties and numerous applications of nanomaterials, there is a pressing need for spectroscopies that probe the fundamental physics of nanoparticles and nanostructures. However, almost all previous studies on nanoparticles have been conducted on nanoparticles that are in close physical contact with other materials, such as nanoparticles suspended in a liquid solvent, nanoparticles embedded in a bulk material, or nanoparticles attached to a surface. All such studies face the fundamental limitation that any observed effect cannot be unambiguously attributed to the nanoparticle itself, since it could be a result of the interaction between the nanoparticle and the solvent/substrate/surface. Most of these exper-

iments also study the same nanoparticles over a long period of time (multiple laser shots), so the particles may become damaged, charged, or stuck in a long-lived excited state. Most importantly, studying nanoparticles that are in contact with other materials prevents the use of many powerful spectroscopies that can only take place with isolated particles in high-vacuum conditions, such as photoelectron spectroscopy and photoion spectroscopy.

One notable exception to this generalization is a handful of pioneering efforts that have used photoemission spectroscopy to study QDs attached to metal surfaces [13–15]. While these studies have produced valuable insights into the electronic structure and dynamics of QDs, they are fundamentally limited in that they must always ensure good electronic contact between the nanoparticle and the metal substrate in order to return electrons to the nanoparticle to counteract the charging that takes place through the photoionization process. When there is good electrical contact between the nanoparticle and the surface, the electronic wavefunction of the nanoparticle is likely distorted from its original state and the measurement cannot be interpreted as a faithful representation of the intrinsic wavefunction of the nanoparticle.

In contrast to previous efforts, we study “gas phase” nanoparticles that are isolated in vacuum. It may be argued that these studies are not relevant to the practical applications of nanoparticles, which involve nanoparticles that are embedded in bulk materials, attached to a surface, or suspended in a liquid. However, the motivation for studying nanoparticles in the gas phase is to gain an understanding of the fundamental properties of the particles and how those properties can be accurately calculated using theoretical models. Just as studying molecules in the gas-phase provided the benchmark for the computational chemistry methods that have, in turn, revolutionized our understanding of chemical reactions in solution, it is possible that the study of nanoparticles in vacuum will provide similar benchmarks for theoretical methods that simulate properties on the nanoscale. In addition, by comparing how the properties of nanoparticles change as they are moved from the gas-phase to the condensed phase, we can gain insight into one of the most important topics in nano-science: how nanomaterials interact with their environment.

In order to investigate the inherent (unperturbed) electronic structure of nanomaterials, we

choose to work with a collimated beam of isolated nanoparticles that are flying through a high-vacuum chamber. Fortunately, many years ago, researchers in the field of atmospheric science had the same desire to study sub-micron aerosol particles in the absence of carrier gas.² These scientists designed an “aerodynamic lens,” a tube containing several small orifices, that “focuses” a nanoparticle aerosol, forming a collimated beam of nanoparticles, while leaving the carrier gas divergent, enabling the separation of the nanoparticles from the gas. Thus, through an unusual combination of techniques and apparatus borrowed from physical chemistry (the VMI spectrometer), optical physics (femtosecond laser pulses), and atmospheric science (the aerodynamic lens), we have made some of the first measurements of the femtosecond dynamics of isolated nanoparticles.

1.2 Electron dynamics in strong femtosecond laser fields

This section provides a broad picture of the motivations for the study of strong-field ionization (SFI) using UV through mid-IR lasers presented in Chapter 3.

1.2.1 The three step model

The interaction of strong laser fields ($\sim 10^{14}$ W/cm²) with atoms and molecules is of great scientific and technological interest because of two related phenomena: high-harmonic generation (HHG) [10] and strong field ionization (SFI) [16]. HHG makes it possible to use tabletop lasers to generate coherent beams of extreme ultraviolet (EUV) and soft X-ray (SXR) light, [11, 12, 17–19] and it has found applications across a broad range of science. For example, HHG makes it possible to observe chemical reactions in real time [20–22], to uncover correlated thermal [23] and magnetic dynamics [24] in materials with elemental specificity, and for coherent imaging on the nanometer scale near the wavelength limit [25, 26]. Similarly, recent studies have revealed that the photoelectron distribution from SFI records information about molecular structure [27–29], suggesting that it may serve as a new technique for understanding molecular dynamics. Both HHG and SFI result from tunnel-ionization of an electron from an atom or molecule (Figure 1.3). The free electron is then

² Interestingly, these efforts also used photoion spectroscopy techniques, though not with femtosecond lasers or angle-resolved detectors.

accelerated to high velocities in the laser field [30]. HHG occurs when the electrons that are driven back towards the parent ion by the laser field recombine radiatively with the parent ion, emitting high-energy photons. SFI corresponds to those electrons that do not recombine; however, they may still re-encounter their parent ion and scatter.

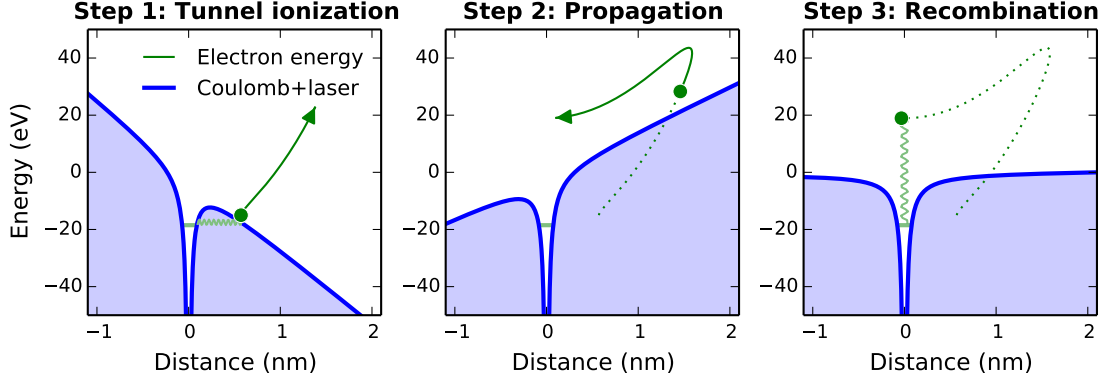


Figure 1.3: **The semi-classical three-step model of high harmonic generation (HHG).** The blue line shows the combined energy of the laser and Coulomb potential, which is changing as a function of time. The green line shows the total energy of the electron (kinetic energy plus potential energy of the laser field) plotted as a function of the distance from the ion. (a) In the presence of a strong laser field (in this case 1×10^{14} W/cm²), the Coulomb potential of an atom (or molecule) is strongly deformed. Under these conditions, a valence electron can tunnel through the barrier and emerge into the continuum (Step 1). (b) In Step 2, the free electron is now driven by the laser field, first away from the ion and then (depending on the phase of the field when the electron tunnels) driven back towards the ion. (c) In Step 3, the electron recombines with the ion emitting a high-energy photon. In the case of strong-field ionization (SFI), the electron does not recombine, but can scatter from the ion.

This semi-classical model of tunnel ionization, propagation in the laser field, and recombination with the ion is known as the “three-step model”. The three-step model ignores the Coulomb potential during the propagation of the electron and only includes the Coulomb potential during the recombination/rescattering step. Consequently, the three-step model is more accurate in cases where the electron are driven a long distance from the ion, making the influence of the Coulomb potential on the propagation of the electron negligible.

1.2.2 Strong field ionization with mid-IR fields

The three-step model makes an important prediction about HHG: the highest possible (cutoff) photon energy (E_{cutoff}) scales with the ponderomotive potential (U_p) as [30]

$$E_{\text{cutoff}} \approx 3.2U_p + I_p, \quad (1.1)$$

where I_p is the ionization potential of the atom (or molecule) and the ponderomotive potential is given by [31]:

$$U_p = \frac{e^2 E^2}{4m_e \omega^2} = \left(9.337 \times 10^{-14} \frac{\text{eV}}{(\text{W}/\text{cm}^2)(\mu\text{m})} \right) I \lambda^2, \quad (1.2)$$

where e is the electron charge, E is the laser electric field, m_e is the electron mass, ω is the angular frequency of the laser, I is the intensity of the laser (in W/cm^2), λ is the wavelength of the laser (in μm), and U_p is in terms of eV.

The important practical implication of Equations 1.1 and 1.2 is that the cutoff energy of high-harmonic generation can be increased either by increasing the laser intensity or increasing the laser wavelength. In practice, a critical ionization level of the gas cannot be exceeded without a severe loss of conversion efficiency, and so the laser intensity cannot be increased past a certain level [12]. Thus, the only available method for scaling HHG to higher photon energies is to use longer wavelength driving lasers. Indeed, recent experiments have demonstrated that driving lasers in the mid-IR can generate photon energies past 1 keV [19] and that driving lasers with wavelengths of 2.0 μm or longer can easily generate isolated attosecond pulses [32]. However, the mechanisms of HHG in the mid-infrared region are not fully understood.

SFI is the “sister process” to HHG, since it corresponds to electrons that tunnel ionize in the same manner and are driven in the same strong laser field, but do not recombine with the atom or molecule. Historically, a careful analysis of SFI has built the foundation for understanding the HHG process. In Chapter 3, we continue this tradition, by observing structures in the photoelectron angular distributions using mid-IR driving lasers. These structures correspond to the multiple rescattering of field-driven electrons with the ion, a process that has recently been suggested as a possible avenue for generating zeptosecond waveforms [33].

1.3 Localized light absorption in nanoparticles

This section provides the broad motivations for the study of Plasma Explosion Imaging (PEI) presented in Chapter 4.

The ability to focus light tightly is immensely useful, enabling numerous innovations in science and technology, including high-resolution microscopy, spectroscopy of small objects, and precision laser-machining. Considering the wide-ranging applications of a small focus, it is not surprising that an incredible amount of effort has been expended to manufacture lenses that minimize aberrations and laser light sources that exhibit good mode quality. However, there is a fundamental lower limit to the diameter of the focus (d) that can be achieved:

$$d = \frac{\lambda}{2n \sin \theta}, \quad (1.3)$$

where λ is the wavelength of the light, θ is the half-angle of the lens, and n is the index of refraction of the medium. Equation 1.3 serves as a limit for how localized a certain wavelength of light can be. Unless, of course, you cheat.

Equation 1.3 applies for lenses and curved mirrors which attempt to focus light at a distance, but nanoparticles can be used to “cheat” this limitation by locally enhancing the light field, sometimes by many orders of magnitude. The most famous example of this enhancement is probably the strong enhancement of the electric field that takes place at the surface of metal nanoparticles and allows the surface enhanced Raman spectroscopy technique (SERS) to evaluate the Raman spectrum of single molecules [34, 35]. More recent studies have successfully utilized the subwavelength focusing of “photonic nanojets” that form behind transparent nanospheres irradiated with laser light to machine features on the sub-wavelengths scale [36]. However, despite the numerous applications of local-field enhancement in nanostructures, there are no techniques to evaluate the local field enhancement that takes place when an intense femtosecond laser pulse irradiates a single, isolated nanostructure. Chapter 4 presents the development of a high-repetition-rate technique capable of observing the local field enhancement that takes place in a range of different nanostructures.

1.4 Shock waves in nanoplasmas

This section provides the motivations for the study of shock waves in nanoplasmas presented in Chapter 5.

When an intense ($>10^{14}$ W/cm²) femtosecond laser pulse is focused into a material, the material is rapidly converted into a plasma and high energy electrons, ions, and electrons are ejected. This is not only useful as a way to study an extreme state of matter using tabletop scale apparatus, but can also serve as a source of high-energy electrons, ions, and photons. The energy of the emitted photons and particles depends on how much of the laser energy can be transferred into the material and how confined the interaction can be made. In order to generate the highest energy interaction, the majority of the laser energy must be coupled into a very small area. This sounds straightforward, but it is not. For example, gas targets are not appropriate because they are not dense enough to absorb the laser light in a small area. Solid surfaces also present a problem, because they are quickly converted to a plasma, at which point they become metallic and reflect most of the laser pulse.

Nanoplasmas, which are formed by laser-irradiating isolated nanoparticles, can serve as the perfect solution, since they are both highly absorbing of laser light [37] and can localize that light on an extremely small scale. The absorbed laser energy is then trapped in the nanoplasma and cannot dissipate, leading to much higher plasma temperatures. Previous experiments have observed the ejection of ions with kinetic energies exceeding 1 MeV [38], and even nuclear fusion [39] in laser-irradiated nanoplasmas. With this motivation, theoretical studies suggested that shock waves could be driven through these nanoplasmas [40–42] and that these shock waves could be used to further enhance the energies of the ejected nanoparticles. However, in the intervening decade, no experimental observation of shock waves propagating through nanoplasmas has taken place. Chapter 5 discusses the first experimental observation of shock waves propagation withing a single nanoplasma and demonstrates how a second “heating” laser pulse can be used to tailor the plasma density profile to optimize the yield of quasi-monoenergetic ions.

Chapter 2

Apparatus and methods

Hofstadter's Law: It always takes longer than you expect, even when you take into account Hofstadter's Law. –Douglas Hofstadter

2.1 Experimental summary

The experiments presented in this thesis explore different physical phenomena, but share several techniques and apparatus in common. In particular, all of the experiments were completed using similar femtosecond laser systems and the same velocity map imaging (VMI) spectrometer.¹ The studies involving nanoparticles and nanoplasmas were conducted using the same nanoparticle generation and delivery system. Thus, this chapter provides a description of the femtosecond laser systems (Section 2.2), the VMI spectrometer (Section 2.3), and the nanoparticle aerosol source (Section 2.4).

2.2 Femtosecond laser system

2.2.1 Chirped pulse amplification

In order to study processes on the femtosecond timescale, we use femtosecond laser pulses obtained from titanium-doped sapphire (Ti:sapphire) laser systems. Ti:sapphire is a material especially suited for the generation of high-intensity femtosecond pulses due to its broad gain bandwidth and high thermal conductivity. Kerr-lens modelocked Ti:sapphire oscillators operate with repetition

¹ It should be noted that, while the laser systems are similar, two different laser systems were used. In addition, the spectrometer evolved over the course of the studies presented in this thesis, such that it now contains very few of its original parts.

rates of 80 to 100 MHz and generate ~ 10 fs pulses with pulse energies on the nJ scale. This allows the focused laser to achieve peak field intensities of $< 10^{13}$ W/cm², even with diffraction-limited focusing. This laser field is still weak compared to the Coulomb field. To move into the strong-field regime, the laser intensity must be increased by at least an order of magnitude.

To decrease the repetition rate and increase the average power (thereby greatly increasing the energy per laser pulse), we use a Ti:sapphire amplifier system. The amplifier cannot directly amplify the 10 fs pulses from the oscillator, since attempting to do so would expose the Ti:sapphire crystal to peak laser intensities above its damage threshold. Instead, amplifiers are designed around the principle of chirped pulse amplification (CPA). In the CPA scheme, the pulses from the oscillator first pass through a grating-based stretcher which frequency disperses the laser pulses in time (“temporally chirps” the pulses) until they have a duration of more than 100 ps [43]. A Pockels cell then selects a single pulse from the 80–100 MHz pulse train and allows this pulse to proceed to the Ti:sapphire crystal. The pulse is then amplified by passing through the Ti:sapphire crystal many times. After the pulse energy has been increased, the ~ 100 ps pulse can then be recompressed to 20–50 fs by passing through a grating-based compressor, which compensates the temporal chirp introduced by the stretcher. The pulse typically cannot be compressed to the original 10 fs pulse duration that it emerged from the oscillator due to the gain-narrowing of the spectral bandwidth that takes place in the amplifier.

In the experiments presented in this thesis, two different laser amplifier systems were used. The strong-field ionization experiments (Chapter 3) were completed using a two-stage multipass amplifier (KMLabs Red Dragon). The nanoparticle experiments (Chapters 4 and 5) utilized a breakthrough high-pulse-energy one-stage regenerative amplifier: the KMLabs Wyvern HE [44, 45]. At first glance, the laser systems seem very similar: the Red Dragon produced 7 mJ, 25 fs pulses at 1 kHz, and the Wyvern HE produces 8–10 mJ,² 40 fs pulses, also at 1 kHz. However, the advantage of the single-stage regenerative amplifier (Wyvern HE) over the two-stage multipass amplifier is

² While the Wyvern HE is capable of producing pulse energies of 10 mJ, the output mode quality ($M^2 \geq 1.3$) is not as good compared to operation at 8 mJ ($M^2 \approx 1.2$). Because a good mode is important for the subsequent frequency conversion steps and minimizes the risk of damage to the optical systems of both the amplifier and the experiment, the amplifier was typically operated near 8 mJ for the experiments described in this thesis.

seen in the reliability of the laser system. The >95 percent up-time of the Wyvern HE is a breakthrough achievement in 10-mJ-class laser systems and was crucial for successfully obtaining data from nanoparticles. More information about the Wyvern HE is presented in Ref 44, as well as in the PhD thesis of Chengyuan Ding [45], who designed and build the amplifier in cooperation with Xiaoshi Zhang and other staff at KMLabs, Inc.

2.2.2 Light sources

A unique aspect of the study of SFI of atomic gases presented in Chapter 3 is that the study was conducted using a wide range of driving laser wavelengths, ranging from the deep-UV at 267 nm, to the mid-IR at 2000 nm. The Ti:sapphire laser can only be tuned over a narrow range near 800 nm, so the other wavelengths must be generated using non-linear light conversion techniques (Figure 2.1). The 400 nm pulses were generated using a beta-barium borate (BBO) crystal, with a thickness of 200 μm . The 267 nm light was generated from sum-frequency generation of 400 nm and 800 nm light in a second BBO crystal. A calcite plate is placed in the beam to compensate for the small time-delay between the 400 nm and 800 nm pulses. The mid-IR pulses at 1300 nm and 2000 nm are generated using parametric amplification techniques described in the following section. This unusually large range of laser wavelengths allowed us to explore how the physics of SFI scale with the driving laser wavelength.

2.2.3 Optical parametric amplifier (OPA)

The optical parametric amplifier (OPA) system used to generate the mid-IR light in Chapter 3 converts the 800 nm output of the Ti:sapphire laser system into mid-IR light at 1300 nm and 2000 nm. The OPA [44, 46] was designed and built at JILA by Matt Seaberg, Paul Arpin, and Stefan Witte and adapted to the higher pulse energies and longer pulse durations of the Wyvern HE by Chengyuan Ding, Tingting Fan, and Wei Xiong.

Recent experiments have demonstrated that high harmonic generation (HHG) can generate much higher photon energies when longer laser wavelengths are used to drive the process [12, 47].

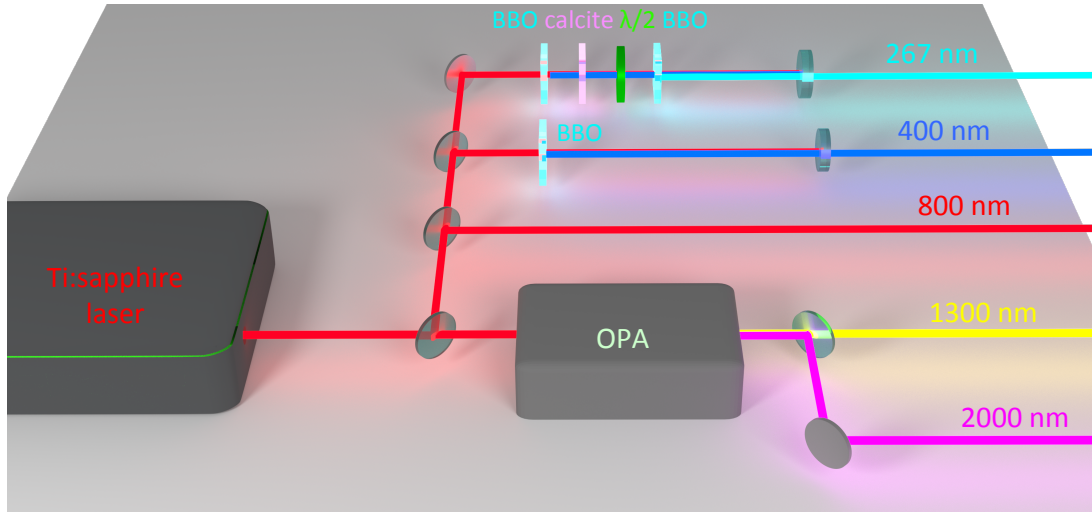


Figure 2.1: **Femtosecond light sources from the UV to the mid-IR.** An unusually large range of wavelengths were available for the experiments described in this thesis. The 800 nm pulses were obtained directly from the amplifier, and 400 nm pulses were obtained through generation of the second harmonic in a BBO crystal. The 267 nm pulses were generated through sum-frequency generation in a second BBO crystal. The 1300 nm and 2000 nm mid-IR pulses were obtained using an optical parametric amplifier (OPA).

Using a driving laser wavelength of 3900 nm, Popmintchev and coworkers [19] were able to generate photon energies in excess of 1 keV. But the advantages of mid-IR driving lasers are seen well before 3900 nm – a 1300 nm driving laser can generate soft X-ray light to the carbon edge at 285 eV [47], and 2000 nm light has recently been shown to generate single attosecond pulses when appropriate phase-matching conditions are used [32]. This breakthrough in using longer wavelength driving lasers for HHG motivated the construction of the OPA and motivates the studies of strong-field ionization using longer driving wavelengths presented in Chapter 3.

2.2.4 Delay line

The time-resolved experiments presented in Chapter 5 were completed using a simple Mach-Zehnder-geometry delay-line setup similar to that shown in Figure 2.2. The dichroic mirrors used to separate and recombine the 400 and 800 nm light were obtained from Lattice Electro-Optics. The translation stage is a model NST-100 from Thorlabs and was controlled in concert with the VMI camera using Matlab 2012b (32-bit version). In Figure 2.2, a single lens is shown focusing both

beams into the interaction region of the VMI. However, in practice separate lenses were typically placed in each beam in order to independently control the focal spot size, as well as to correct for chromatic aberration.

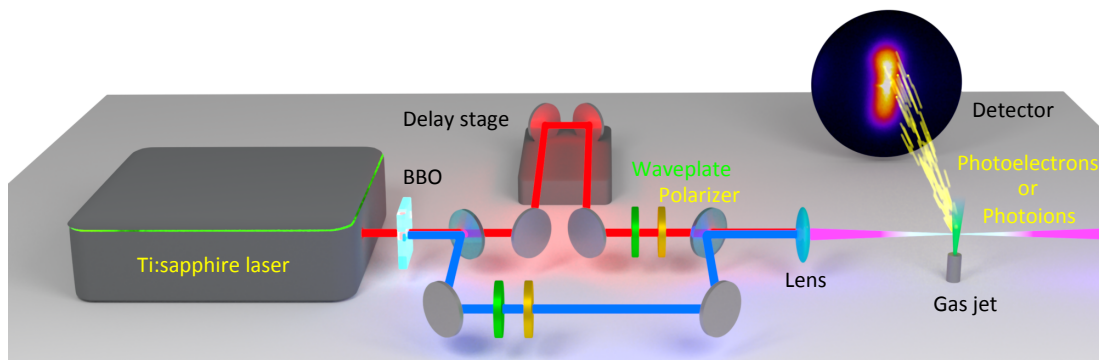


Figure 2.2: **A typical femtosecond pump-probe experiment.** The Ti:sapphire amplifier produces 25–40 fs pulses of 800 nm light (red beam). In this example, a BBO crystal converts the 800 nm light to 400 nm. Dichroic mirrors are used to split and later recombine the two laser pulses. A waveplate and polarizer placed in each arm are used to control the intensity of each beam. A motorized delay stage in the 800 nm arm is used to control the relative path length and thereby control the relative time delay of the two pulses. In the velocity-map imaging (VMI) spectrometer, the intense laser pulses ionize atoms/molecules in a gas jet (or nanoparticles in a particle beam) and the electrons (or ions) are projected onto a microchannel-plate–phosphor-screen detector by a static electric field.

2.3 Velocity map imaging spectrometer

2.3.1 Concept and history

The concept of charged particle imaging is refreshingly simple - charged particles (either electrons or ions) are simply projected onto a position sensitive detector using an electric field, making a two-dimensional picture of the momentum distribution. The field of photoion imaging was born in 1987 when Chandler and Houston [48] used a position-sensitive detector to record the angle-resolved ion momentum distribution resulting from the dissociation of CH_3I by a 266 nm laser pulse. Due to its simple implementation and powerful capabilities, photoion imaging became a popular method for studying gas-phase chemical reactions. In the mid-1990s, the first photoelectron images were recorded by Helm [49] and Bordas [50].

Eppink and Parker [51] improved upon the methods of Chandler and Houston by implementing an electrostatic lens that could compensate for the extended interaction region formed by the intersection of the ionizing radiation with the particle beam. Since this method maps the velocity of each particle to position on the detector irrespective of the exact location where the particle originated, this method was termed Velocity Map Imaging (VMI) and the apparatus has become known as a VMI spectrometer. The VMI spectrometer provides an additional advantage over the original photoion spectrometer invented by Chandler and Houston [48]; by removing the metal meshes that all previous studies had placed between the interaction region and the detector, Eppink and Parker increased the fraction of electrons or ions that reach the detector and further increased the resolution of the instrument [52].

The standard “Eppink and Parker” VMI geometry consists of three circular electrodes: a repeller plate, an extractor plate that features a hole through which the electrons pass, and a ground plate that features a somewhat larger hole. As suggested by the name, the ground plate is typically held at 0 V, though this is not always the case [52]. The relative ratio between the repeller and extractor plates sets the “focus” of the spectrometer. The exact ratios needed for the best focus depend on the geometry of the spectrometer, and can be used to select between velocity map imaging mode (repeller-to-extractor ratio of ~ 0.75) [52] and spatial imaging mode (repeller-to-extractor ratio of ~ 0.98) [53, 54]. When the repeller-to-extractor ratio is set somewhere between these two extremes, the image produced on the VMI is a convolution the spatial and momentum profiles of the generated electrons.

2.3.2 Theory

Complete treatments of the principles of VMI can be found in numerous sources, with the most eloquent being the original 1997 Review of Scientific Instruments article by Eppink and Parker [51], Whitaker’s 2003 textbook Imaging in Molecular Dynamics [52], and a wonderful 2004 Master’s thesis by Sara Thorin [55] that provides extensive details on the practicalities of constructing and operating a VMI spectrometer.

In brief, the basic principles of VMI can be understood from a simple analysis of the equations of motion. Under the assumptions that the acceleration region is small compared to the free-flight region and that the initial kinetic energy of the particles is small compared to the energy imparted by the static electric field of the spectrometer,³ the radial position of the electrons on the detector R is given by [51, 52, 55]

$$R \approx NL\sqrt{\frac{E_r}{qV}}, \quad (2.1)$$

where N is a magnification factor particular to the geometry of the spectrometer and the relative voltages of the electrodes, L is the length of the free-flight region, E_r is the radial component of the kinetic energy of the particle, q is the charge of the particle, and V is the potential through which the particle is accelerated. If we ignore the terms from the spectrometer, we can express the radial position of the ions as

$$R \propto \sqrt{\frac{E_r}{Z}}, \quad (2.2)$$

where Z is the charge number of the particle. This expression makes it clear that the term “*velocity map imaging spectrometer*” is something of a misnomer, since particles of the same velocity but different masses (or different charges) will not map to the same position on the detector. Astute readers will therefore read the term “VMI spectrometer” as “square-root of kinetic energy divided by charge imaging spectrometer,” but will accept that fact that the latter term is too cumbersome for common usage, and would require a more stylish acronym before gaining popularity.

The above theory makes the assumption that the only field acting on the spectrometer is the electric field of the spectrometer. Any additional fields will affect the trajectory of the particles in the spectrometer and must be avoided. One of the most problematic is Earth’s magnetic field. In order to avoid affects from Earth’s field, a VMI spectrometer must be enclosed within one or more layers of μ -metal, an alloy (composed primarily of Ni and Fe, with a few percent Cu, Cr, and Mo) that significantly attenuates magnetic fields. Any parts of the VMI spectrometer that are placed

³ The assumptions of a long free-flight region and slow initial momentum are good approximations in regime of threshold-ionization where VMI is typically applied. In the regime of strong-field ionization, higher kinetic energy electrons are generated, making numerical modeling (using a program such as SIMION [56]) more important to check the linearity and resolution of the instrument.

within the μ -metal must be non-magnetic in order to avoid introducing any additional magnetic fields into the VMI or free-flight regions.

2.3.3 Implementation

The VMI spectrometer in the Kapteyn–Murnane group (Figure 2.3) was designed and partially assembled in early 2010 by Xibin Zhou, Bosheng Zhang, Predrag Ranitovic, and Chengyuan Ding. The design of the spectrometer assembly (the electrodes and their support structure) is based largely on the VMI spectrometer in the Weber lab at JILA [57], which is, in turn, based on the VMI spectrometers in the Lineberger Group at JILA and Sanov Group at the University of Arizona [58, 59]. All of these spectrometers share the standard three-electrode design of Eppink and Parker [51]. In late 2010, the author took over the construction of the VMI spectrometer with the help of Chengyuan Ding and Predrag Ranitovic. The author designed the gas jet assembly and the skimmer assembly, fixed the virtual leaks caused by non-vented screws and vacuum-incompatible Kapton tape, and re-designed the electrode support assembly to support voltages up to 5 kV.

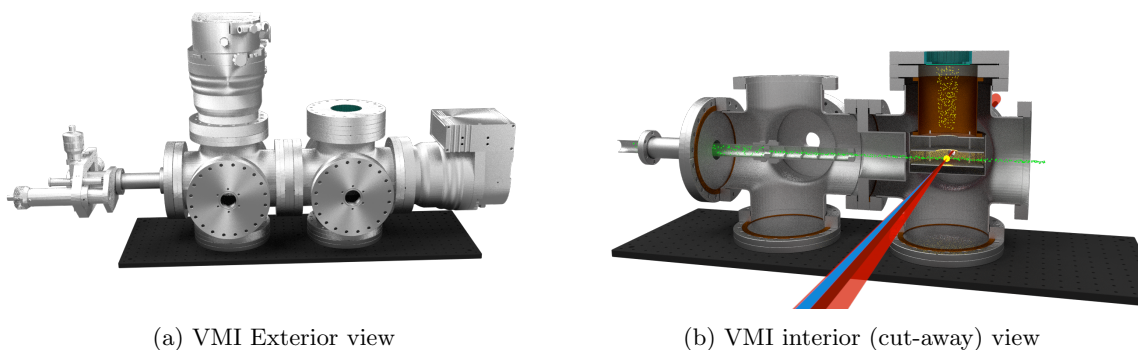


Figure 2.3: **Schematic of the VMI spectrometer** (a) Exterior view of the VMI spectrometer, showing the ~ 500 L/s turbopumps that are used to maintain medium-vacuum ($< 10^{-2}$ Torr) in the source chamber (left) and high-vacuum ($< 10^{-6}$ Torr) in the spectrometer chamber. The XYZ manipulator on the left side of the apparatus allows for aerodynamic lens (or gas jet) to be positioned relative to the skimmer that separates the two chambers. (b) Interior view of the VMI spectrometer, showing the aerodynamic lens forming a collimated beam of nanoparticles. The nanoparticle beam passes through the tube-skimmer and into the spectrometer chamber. The laser beam ionized the nanoparticles and creates electrons (and often ions) that are projected onto the detector by the electric field generated by three stainless steel electrodes.

2.3.3.1 Spectrometer assembly

The “spectrometer assembly” is the term given to the electrodes, the structure that supports them, and the μ -metal that surrounds them. This is the part of the instrument that required the most custom machining, and also the most iterations before it was fully operational. Since most VMI spectrometers only collect electrons with kinetic energies below 10 eV, the electrodes are typically not designed to support voltages higher than 1 kV. In contrast, since the strong-field ionization process can easily produce electrons in excess of 50 eV, this instrument needed to support higher voltages on the electrodes while avoiding arcing or corona discharge.

In the first iteration, the electrodes were made from copper, since it is a readily machinable material that is not magnetic. The original copper electrodes could only support ~ 2 kV due to the roughness and contamination of the surface [60]. To increase the supportable potential of the electrodes to the full 5 kV of the PS350 power supplies (Stanford Research Systems), the copper electrodes were replaced with stainless steel electrodes. Because some varieties of stainless steel can be slightly magnetic, it is typically considered an inappropriate for spectrometer construction. However, new electrodes were made of austenitic stainless steel (Type 316) which is not magnetic. The electrodes were polished with progressively finer-grit sandpaper up to 2000 grit, but it’s likely that the electrodes could support even higher voltages with electropolishing.⁴ Additionally, the hole in the ground plate was expanded from 1 inch to 1.5 inches in order to allow higher kinetic energy photoelectrons to be collected on the detector.

For the experiments presented in Chapter 3, the spectrometer assembly was rotated 90 degrees from the orientation shown in Figure 2.3b to allow the gas jet to pass through a ~ 1 mm hole in the repeller plate. This allowed the skimmer to be positioned less than 1 inch from the interaction region, which minimized the expansion of the gas and therefore maximized the gas density probed by the laser. For the nanoparticle experiments (Chapters 4 and 5), it was deemed undesirable to use a geometry where the nanoparticle beam impacted the detector, since it would likely deposit a spot of

⁴ Indeed, a new “high energy” VMI assembled in KM-Group features electropolished electrodes and can support up to 15 kV before arcing.

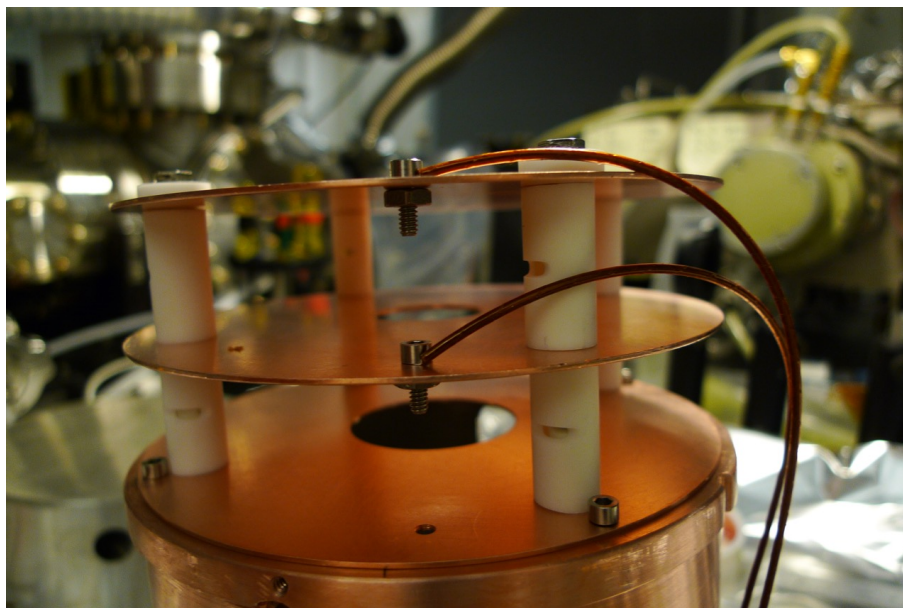


Figure 2.4: **The VMI electrodes.** This photograph shows the spectrometer assembly with the μ -metal removed to reveal the copper electrodes, which were later exchanged for stainless steel electrodes. The electrode support structure consists of threaded molybdenum rods (not visible) surrounded by an inner ceramic tube. One-inch sections of larger diameter tube (the white cylinders) fit over the inner tubes and provide the appropriate spacing between the electrodes.

nanoparticles in the center of the detector. Thus, for these experiments, the spectrometer assembly and detector flange were rotated by 90 degrees to the configuration shown in Figure 2.3b. Since the nanoparticle beam is only slowly diverging after exiting the aerodynamic lens, the additional 2 inches that the beam must pass before reaching the interaction region does not cause an appreciable decrease in the particle density.

2.3.3.2 Gas jet

For the strong-field ionization experiments described in Chapter 3, the target was gas-phase atoms and molecules obtained via supersonic expansion of a gas in vacuum. The gas (backing pressure of ~ 700 Torr) is introduced into the “source” chamber through a $30 \mu\text{m}$ nozzle. The expanding gas then passes through a $300 \mu\text{m}$ skimmer (Beam Dynamics, Inc. [61]) and into the differentially pumped “spectrometer” chamber. The gas jet increases the pressure in the source chamber to around 10^{-4} Torr and increases the pressure in the spectrometer chamber to approximately 10^{-7} Torr, from

base pressures of 10^{-9} Torr. The exact pressure in the spectrometer chamber depends on the exact position of the gas jet relative to the skimmer.

The gas jet must be precisely aligned with the skimmer, so that the beam of gas exiting the skimmer will pass cleanly through the small hole in the repeller plate. To achieve good alignment, the gas jet assembly is mounted on an XYZ manipulator that allows for precise positioning in three dimensions. It would be very difficult to attempt to align the focused laser beam and the gas jet simultaneously. Therefore, the gas jet is aligned first, by moving the position to optimize the pressure in the spectrometer chamber. To roughly find alignment, it is possible to simply examine the pressure in the spectrometer chamber as a function of the gas jet position and align by hand. Once rough alignment is obtained, fine alignment can be completed by taking small steps in each dimension transverse to the flow of gas and fitting the resulting pressures to a Gaussian function. Using this method, the gas jet can be aligned to within a few μm and the gas beam can easily be found with the focused laser. Further optimization of the gas jet position is then completed by iteratively moving the gas jet position and the finding the new position of the interaction region using the laser.

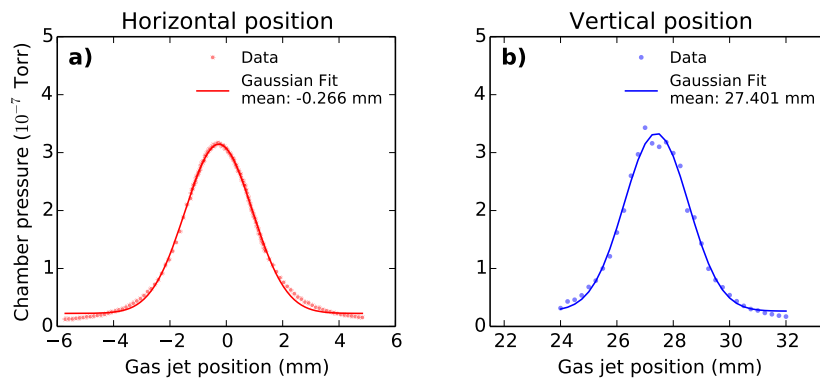


Figure 2.5: **Alignment of the gas jet to the skimmer.** The $30\ \mu\text{m}$ gas jet must be carefully aligned to the $300\ \mu\text{m}$ skimmer so that the skimmed beam of gas passes directly through the interaction region. Coarse alignment can be accomplished by moving the gas jet to optimize the pressure in the spectrometer chamber. Precise alignment is achieved by moving the gas jet in small increments and recording the pressure in the spectrometer chamber as a function of the micrometer position. This is performed in the horizontal (a) and vertical (b) directions. A Gaussian fit allows the center point to be precisely extracted.

2.3.3.3 Detector

The electrons and ions are detected using a phosphor screen behind two microchannel plates (MCPs) in a chevron stack. Each MCP is biased with up to 1.2 kV per plate⁵ and ejects many electrons each time an electron or ion collides with a channel. The gain is extremely high, such that up to 10^7 electrons emerge from the backside of the MCP stack for each electron that impacts the front of a channel. The electrons that leave the MCP are accelerated onto a phosphor screen, that converts the electrons into visible light, with a wavelength that depends on the material coating the phosphor screen. We used two different phosphor screens: P43, which emits at 545 nm and has a lifetime of 1 ms, and P47 which emits at 400 nm and has a lifetime of 55 ns [62]. The P43 phosphor produces more photons per electron impact (it's "brighter"), but the faster response time of the P47 phosphor makes it more appropriate for time-of-flight studies. The light on the phosphor screen passes through a $f/1.4$ camera lens (Fujinon) and is recorded with a CCD camera (Pike 145b, Allied Vision Technologies).

The assembly that holds the MCP and phosphor is a 75 mm Beam Observation System (BOS-75), manufactured by Beam Imaging Solutions (Longmont, CO). Since all of the experiments described in this thesis involved unusually high electron/ion flux, the MCPs were damaged rapidly and several sets of MCP plates and phosphor screens were used:

- The study described in Chapter 3 used two Imaging Grade 60:1 MCP plates and a P47 phosphor screen that were installed in 2011 and replaced in 2012.
- The study described in Chapter 5 used two Detection Grade 40:1 MCP plates and a P43 phosphor screen that were installed in 2012 and replaced in 2014.
- The study described in Chapter 4 used a matched set of two Imaging Grade 60:1 MCP plates and a P47 phosphor screen. These were installed in mid-2014 and are the MCP plates and phosphor screen that are currently installed as of December 2014.

⁵ The 60:1 length-to-diameter ratio plates can support 1.2 kV, the 40:1 plates can only support 1.0 kV. When setting the voltage across the MCP stack, keep in mind that any voltage divider will obscure the true voltage being applied to the plates. Most pairs of plates do not have the same resistance, and so a different voltage divider is needed.

The phosphor screens (75 mm diameter) were obtained from Beam Imaging Solutions and the MCP plates (75 mm) were obtained from Photonis, Inc. via Beam Imaging Solutions.

2.3.4 Abel transform

The VMI spectrometer records a 2D projection of the 3D photoelectron (or photoion) angular distribution (PAD). Several techniques exist for providing the desired full 3D PAD, or, simply a slice of the 3D PAD. For some experiments where ions are detected, rapid gating of the detector can be used to capture only a small slice of the expanding Newton sphere [52, 63], but this technique cannot be used for photoelectrons, because the detector gating is not nearly fast enough. Another approach relies on the fact that sometimes the PAD can be rotated in the laboratory frame, as is the case for SFI, where a waveplate can be used to rotate the electric field of the laser and consequently rotate the PAD. If many 2D projections of the PAD are captured at many different angles of rotation, then the 3D PAD can be reconstructed using tomographic methods.

However, the vast majority of VMI images are recorded of PADs that exhibit cylindrical symmetry about the laser polarization, and the axis of rotational symmetry lies in the plane of the recorded image. In this case, the Abel transform may be applied. The Abel transform utilizes the cylindrical symmetry of the PAD to provide a 3D reconstruction from the 2D projection recorded by the VMI spectrometer. While the Abel transform has an exact mathematical definition, it is nearly impossible to apply because it is extremely sensitive to the noise and imperfect symmetry present in real-world VMI datasets [52, 64]. Consequently, several different numerical approximations have emerged to allow 3D PADs to be conveniently reconstructed from experimental VMI data. The most well-known methods include Vrakking’s Iterative Inversion method [65], the BASEX algorithm [64], and the Polar Onion Peeling (POP) method [66]. While all of these three methods produced low-noise transforms on our datasets, the BASEX algorithm proved to be the fastest and most convenient,⁶ and was used to transform the data in Chapter 3. The PADs recorded from nanoparticles

⁶ Specifically, the BASEX algorithm was the most convenient because the Reisler group at USC kindly provided the Matlab implementation of the BASEX algorithm, which the author could port to Python. The reconstruction is then scriptable and can be applied to large, multi-image datasets, taking less than 1 second for each 1 megapixel image.

(Chapter 4 and 5) do not depend on the laser polarization and do not exhibit cylindrical symmetry, so the Abel transform cannot be used.

2.4 Nanoparticle aerosol source

A high-concentration of isolated nanoparticles in the VMI spectrometer is achieved by preparing a nanoparticle aerosol and then injecting the aerosol into a high-vacuum chamber via the aerodynamic lens. The integration of aerosol technologies with the VMI spectrometer was enabled through a collaboration with the Jose Jimenez group in the CU Chemistry Department, especially Jimenez-Group members Brett Palm and Pedro Campuzano-Jost.

2.4.1 Atomizer

The nanoparticle aerosol is generated using a Collison-type⁷ atomizer (TSI, Model 3076), which uses compressed gas to make a fine mist of droplets from a liquid solution (Figure 2.6). As the droplets evaporate, they leave behind whatever material is suspended or dissolved in the starting solution. In the case of a colloidal nanoparticle solution, the droplets will contain one or more nanoparticles, and when they evaporate, will leave behind single nanoparticles or clumps of many nanoparticles. In the case of a salt solution, the droplet will evaporate to leave behind either a single crystal or an amorphous clump, depending on the properties of the material. As discussed in Section 4.3.2, electron microscopy reveals that a solution of NaCl produces mostly single crystals, though some amorphous clumps can also be seen.

The performance of the atomizer depends on the liquid used and the pressure of the carrier gas. The recommended operating pressure of the atomizer is 30 psig when air is used as a carrier gas. We found that the pressure required to generate a high concentration of nanoparticles decreased with the viscosity of the solvent – both hexane and acetone produced the highest concentrations of nanoparticles with pressures of about 20 psig. An additional advantage of using lower pressures is that there is less solvent loss through evaporation. We used several different carrier gases – including

⁷ Often miswritten as “collision-type”, the Collison-type atomizer is named after W. E. Collison, who presented the design at a 1932 meeting of the British Medical Association [67].

He, N₂, Ar, Ne, and CO₂ – and there was not a detectable difference in the particle concentrations when different gases were used. Thus, different carrier gases could be used depending on which gas minimized the background signal in the VMI spectrometer.

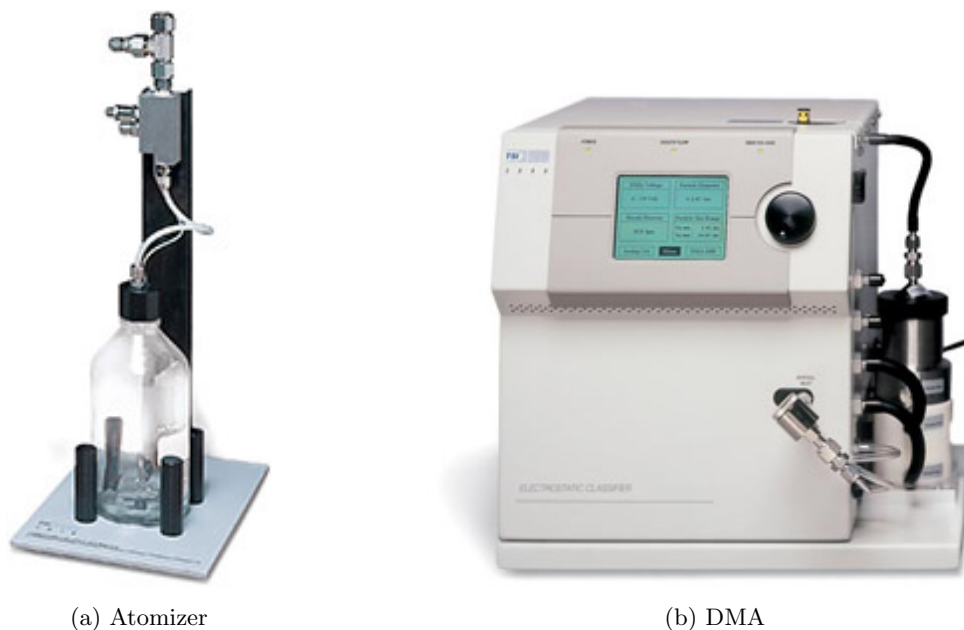


Figure 2.6: **The atomizer and differential mobility analyzer (DMA).** (a) The atomizer uses compressed gas to prepare an aerosol of droplets, which quickly evaporate to leave behind the material in solution. (b) The electrostatic classifier and DMA column (the cylindrical steel object on the right) select only a specific size of particles. Photographs courtesy of TSI, Inc.

A significant problem with the atomizer is that it relies on the evaporation of $\sim 1 \mu\text{m}$ diameter droplets⁸ to generate nanoparticles. Since we are interested in studying nanoparticles that are 50 nm or smaller, the vast majority of the volume of a $1 \mu\text{m}$ droplet must evaporate. In order to generate nanoparticles that are not coated with a thick layer of contamination, a very high level of solvent purity is necessary, and the level of solvent purity required increases as the final particle size is decreased. A striking example of this effect is seen in Chapter 4, where the 50 nm gold nanoparticle sample is coated with a layer of contamination that is larger than the particle itself. This problem is compounded as we move to experiments that are more surface sensitive, which causes even a thin layer of surface contamination to have a large effect. For these reasons, we have plans to switch the

⁸ The atomizer produces a wide distribution of droplet sizes, which is centered around $1 \mu\text{m}$ diameter and depends on the solvent and pressure of the carrier gas.

nanoparticle source to a magnetron sputtering source, as discussed in Section 6.3.2.

2.4.2 Electrostatic classifier

Nanomaterials often exhibit properties that vary with the dimensions of the nanoparticle, making it is very useful to be able to prepare a nanoparticle sample with a controllable size. This is achieved by passing the aerosol through a differential mobility analyzer (DMA) column connected to a control box known as an electrostatic classifier (TSI 3080, Figure 2.6b). Two different DMA columns were used, a short column optimized for particles ranging from 2 to 150 nm (TSI 3085) and a long column (borrowed from the Jimenez Group) optimized for particles ranging from 10 to 1000 nm (TSI 3081).

2.4.3 Aerodynamic lens

The aerodynamic lens (Figure 2.7) was invented in 1995 by a team at the University of Minnesota [68, 69] and creates a collimated beam of particles from an aerosol. By passing the aerosol through a series of small orifices, where the diameters and distances are carefully chosen, the aerodynamic forces drive the particles to follow straight paths while leaving the gas divergent at the exit of the lens.

Each aerodynamic lens is designed around a certain flow rate, which is controlled by varying the pressure at the input of the lens. The lens used in this thesis requires ~ 1.5 Torr, which is typical of aerodynamic lenses in general. In order to drop the pressure from atmospheric pressure to 1.5 Torr, a small flow-limiting “critical orifice” is required. In our preliminary studies, we used a thin steel disk-orifice (SPI, Inc.) with a $100\ \mu\text{m}$ hole, as is commonly used in instruments studying atmospheric aerosols. This achieved the appropriate pressure drop, but it clogged within about one hour when we used solutions with concentrations of 1 g/L. In order to reduce clogging, we switched to a glass capillary tube with an inner diameter of $250\ \mu\text{m}$ and a length of about 15 cm, dimensions that offer a similar conductance to the $100\text{-}\mu\text{m}$ disk-orifice. This tube-style critical orifice increased the time before clogging to about 20 hours of continuous operation. It is not clear what aspect of

the glass tube prevents clogging, since it could be the increased inner diameter of the glass tube, the smoother microscopic surface of glass compared with steel, the non-reactive chemical nature of glass, or the long length of the tube, which may produce a less turbulent flow at the tube exit.

When using the aerodynamic lens, we also had problems with clogging the skimmer that separates the source and spectrometer chambers and allows for differential pumping. So, using a similar solution to the critical orifice, we swapped the thin $300\ \mu\text{m}$ orifice for a long “tube-skimmer”. The 1.5 mm inner diameter of the tube skimmer allowed the $\sim 0.5\ \text{mm}$ nanoparticle beam to pass cleanly through the skimmer without clogging, and the longer length (35 mm) provided a sufficiently low conductance to permit effective differential pumping of the spectrometer chamber.

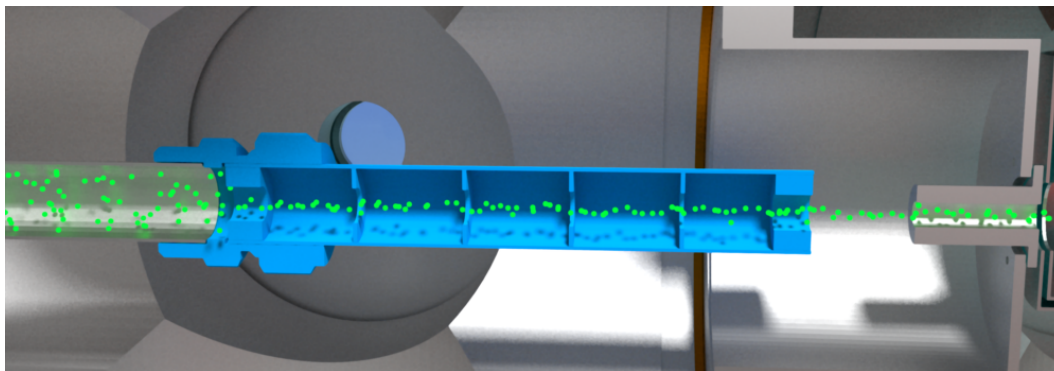


Figure 2.7: **The aerodynamic lens.** The nanoparticle aerosol enters the left side of the aerodynamic lens (blue) and, after passing through a series of orifices, the aerosol emerges from the right side of the lens as a collimated beam with low divergence. The carrier gas (not shown) is still divergent and does not pass through the skimmer (right). This allows the laser to interact with a concentrated beam of nanoparticles in the absence of carrier gas. This drawing is not to scale and the aerodynamic lens is slightly compressed in the horizontal dimension. The exact dimensions of the lens used in this study are provided in Table 1 and Figure 1 of Ref. 70.

2.4.4 Light scattering

In order to check that the particle beam is passing through the spectrometer, we implemented a simple light-scattering experiment. Though the particles are smaller than the wavelength of visible light, they are still large enough to scatter strongly. Thus, when the particle beam is crossed with a green laser pointer (5 mW), a faint glow is visible to the naked eye. To improve the sensitivity of the measurement, we illuminate the particle beam with an unfocused (but collimated) 0.75 W, 532 nm

laser (Wicked Lasers) and observe the light scattering using a CCD camera. Once the nanoparticle beam is aligned through the spectrometer, it can easily be intersected by a focused laser beam by looking at the photoelectron or photoion signal on the VMI spectrometer.

2.4.5 Single particle experiments

The number concentration of nanoparticles emerging from the aerodynamic lens is on the order of 10^5 particles/cm³ by the time the nanoparticle beam reaches the interaction region. For many of the experiments, the volume of the interaction region (the intersection of the laser beam and the particle beam) is on the order of 10^{-7} cm³. In this scenario, there is, on average, less than one nanoparticle in the focal volume for each laser shot. Thus, most laser shots do not hit a nanoparticle. When a laser shot does hit a nanoparticle, there is only a small chance that it will hit two nanoparticles. This technique allows the observation of a single nanoparticle. The caveat is that the interaction of one laser pulse with one nanoparticle needs to produce enough electrons or ions to produce a reasonable signal. This condition is met when a plasma is formed in the nanoparticle, as is demonstrated in Chapters 4 and 5 of this thesis.

Chapter 3

Electron dynamics in strong field ionization

This chapter is adapted, with permission, from:

- D. D. Hickstein, P. Ranitovic, S. Witte, X.-M. Tong, Y. Huismans, P. Arpin, X. Zhou, K. E. Keister, C. Hogle, B. Zhang, C. Ding, P. Johnsson, N. Toshima, M. J. J. Vrakking, M. M. Murnane, and H. C. Kapteyn. Direct Visualization of Laser-Driven Electron Multiple Scattering and Tunneling Distance in Strong-Field Ionization. *Phys. Rev. Lett.*, 109, **2012**, 073004. DOI: 10.1103/PhysRevLett.109.073004
©2012 American Physical Society

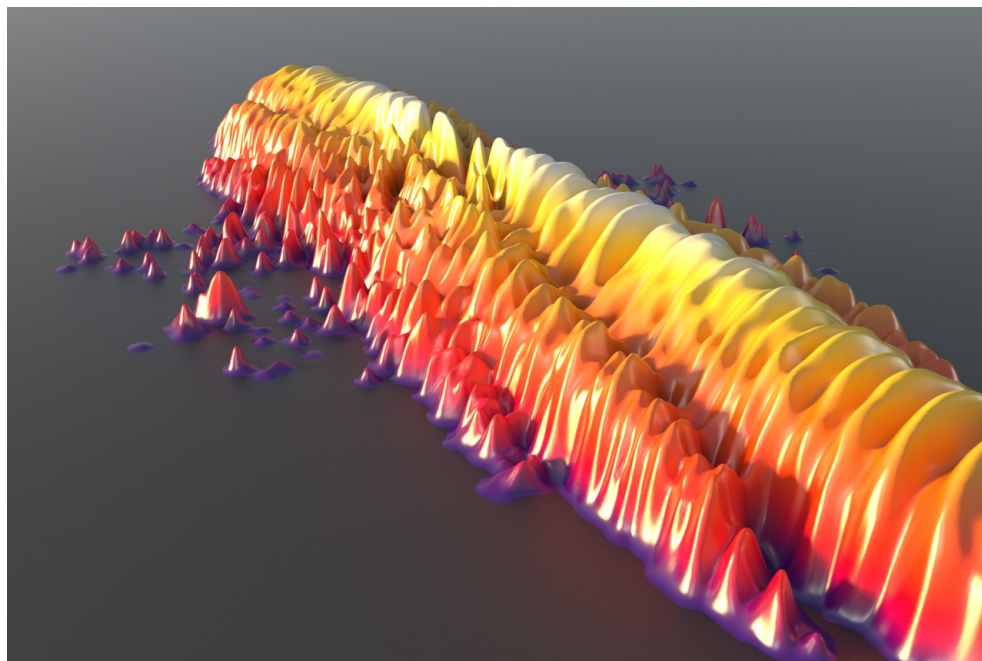


Figure 3.1: **Illustration of photoelectron rescattering.** (a) This numerical simulation of the strong field ionization of xenon (using a 1300 nm laser) illustrates the numerous interferences that take place in the field-driven electron wavepacket. Calculation by Xiao-Min Tong, Tsukuba University, art by Brad Baxley, JILA.

3.1 Abstract

By systematically recording the photoelectron angular distributions (PADs) resulting from the strong field ionization of gas-phase atoms and molecules with laser wavelengths ranging from 262 nm to 2000 nm, we observe distinct structures in the PADs that correspond to the multiple rescattering the field driven electron with the parent ion. Using a simple scattering-wave model of strong-field ionization, we show how the interference patterns that result from electron-ion scattering can be understood using straightforward methods. The shape of these structures can be associated with the specific number of times the electron is driven past its parent ion in the laser field before scattering. Furthermore, a careful analysis of the cutoff energy of the structures allows us to experimentally measure the distance between the electron and ion at the moment of tunnel ionization. This work provides new physical insight into how atoms ionize in strong laser fields, and has implications for further efforts to extract atomic and molecular dynamics from strong-field physics.

3.2 Introduction

3.2.1 Zeptosecond waveforms

Recent theoretical work [33] has shown that when the high-harmonic generation (HHG) process is driven with mid-IR lasers, the generated soft X-ray waveforms exhibit modulations on the zeptosecond timescale, suggesting a possible path for generating laser pulses on the sub-attosecond timescale. The origin of the zeptosecond modulations is the interference of harmonics generated from electrons that recombine on the first time they are driven past the ion (the first “revisit”) with electrons that recombine on subsequent ion revisits. Thus, there is considerable motivation to understand the role of this “multiple rescattering” process¹ as it may be serve as the next breakthrough in generating the shortest laser pulses. In this chapter, we study strong field ionization (SFI), the complementary process to HHG, in order to gain an understanding of multiple rescattering in strong

¹ In strong-field physics, even the first time that the electron is driven past the ion is commonly referred to as “rescattering”. The rational for adding “re” is that the tunnel ionization process is assumed to be the first electron-ion “scattering” process.

laser fields and investigate how this process changes as we tune the wavelength of the driving laser over nearly an order-of-magnitude, from the UV to the near-IR.

3.2.2 HHG and SFI in the mid-IR

When an atom or molecule is illuminated with a strong ($\sim 10^{14}$ W/cm²) femtosecond laser field, an electron wavepacket will tunnel-ionize and accelerate in the field. Depending on the phase of the laser field when the electron tunnels, it may be completely turned around and returned to the parent ion (Section 1.2.1). The returning electron can either recombine with the parent ion, releasing its kinetic energy as a high-energy photon [10, 16, 71], or elastically scatter from the potential of the ion. The photons and electrons generated by these strong-field processes have the potential to probe the dynamic structure of molecules and materials on the sub-nanometer length scale and femtosecond-to-attosecond time scale. Recent studies have suggested that structures seen in angle-dependent photoelectron spectra may be useful for determining time-resolved molecular structures [28, 29, 72, 73], characterizing attosecond electron wavepackets [74, 75], and studying the dynamics of electron wavepacket propagation [76, 77]. However, despite extensive analyses [30, 78–81], many features observed in angle-resolved photoelectron spectra still lack a simple physical explanation.

The recent development of high pulse energy (>1 mJ) femtosecond lasers [82] in the mid-infrared (mid-IR) and angle-resolved detection schemes [51] has enabled new advances in visualizing strong-field physics. Electrons that are ionized in a mid-IR laser field reach higher velocities due to the larger ponderomotive energy, $U_p \propto I\lambda^2$, where I is the intensity and λ is the wavelength of the driving laser. The possibility of harnessing the high-energy electrons that are first ionized and then driven back to a molecule by a strong laser field has inspired several theoretical and experimental efforts to use strong field ionization to probe molecular structure [27, 28, 83, 84]. Recently, Huisman and coworkers [85] used 7 μm mid-IR lasers in combination with angle-resolved detection to observe angular interference structures in the photoelectron spectra of metastable xenon atoms. They presented a theoretical model that explains these structures based on the difference in phase between the two different paths that electrons can take to reach the same final momentum: either proceeding directly to

the detector, or rescattering from the ion before reaching the detector. In other work, Blaga and coworkers [86] irradiated atoms and molecules with 1.7–3.4 μm lasers and discovered an unexpected spike in the (non-angle-resolved) photoelectron energy spectrum that they refer to as the low-energy structure (LES). Subsequent papers [87–90] proposed various interpretations, but all agree that this low-energy structure arises from the rescattering of electrons by the parent ion.

In this work, we develop an intuitive model for understanding strong-field ionization as a simple superposition of plane and spherical photoelectron waves. This approach extends the standard three-step model of strong field ionization that has provided crucial physical insight into strong field ionization [91] and high-harmonic generation [92, 93]. We use this model to show that new interference structures, which we observe in the experimental photoelectron angular distributions generated by mid-IR lasers, are created by electron trajectories that scatter from the parent ion after passing by the ion several times (Figure 3.2). The quantum phase accumulated by the electrons during their oscillatory path between ionization and rescattering is directly imprinted onto the photoelectron angular distribution. Thus, the shape and spacing of the interference structures directly corresponds to the specific number of times the electron re-encounters its parent ion before scattering strongly. Through an analysis of the energy cutoff of these newly observed structures, we show that when an atom is ionized by an intense laser, the electron emerges at a finite distance from its parent ion that corresponds to the far side of the quantum tunneling barrier. Our simple model thus allows us to uncover valuable physical insight into strong-field electron dynamics that is not readily extracted from full quantum simulations.

3.3 Experiment

Ultrashort (30 fs, 785 nm) laser pulses with a maximal per-pulse energy of 7 mJ are derived from a two-stage multipass Ti:sapphire amplifier (KMLabs Red Dragon) operating at 1 kHz. The second harmonic (393 nm, ~ 40 fs) is generated in a beta-barium borate (BBO) crystal (Eksma Optics). The third harmonic (262 nm, ~ 50 fs) is generated with four-wave mixing of the fundamental and second harmonic in a BBO crystal using a collinear geometry (Femtokit FK-800-020, Eksma Optics).

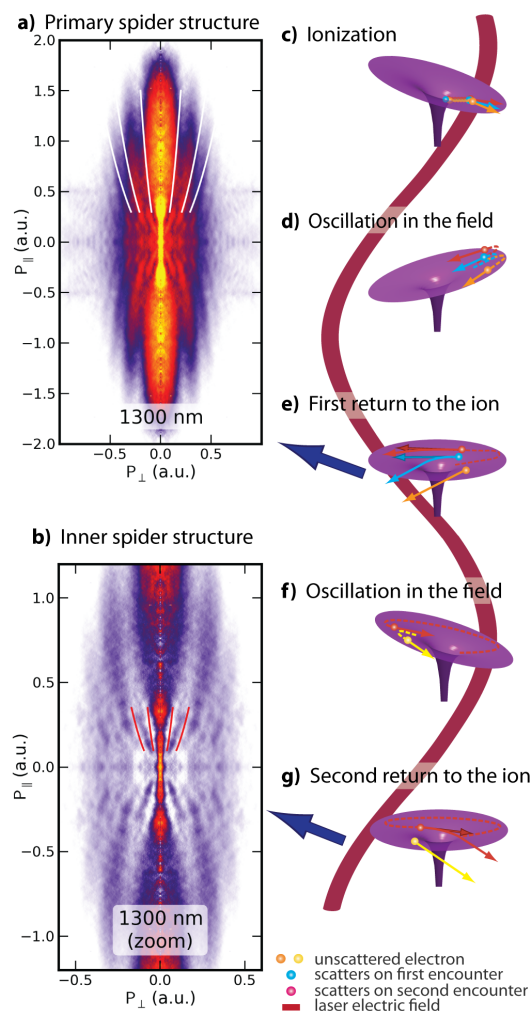


Figure 3.2: **Summary of multiple rescattering.** (a) The photoelectron angular distribution resulting from the ionization of argon gas with a 1300 nm, 7.5×10^{13} W/cm², 40 fs laser pulse. The primary spider structure (minima shown with white lines) results from interferences between directly ionized electrons and those that are driven back to scatter from the Coulomb potential of the ion before reaching the detector. (b) The newly observed inner spider structure (minima shown with red lines) results from electron trajectories that scatter from the Coulomb potential on their second re-encounter with the ion, and the interfere with unscattered trajectories. (c–g) Simple laser-driven electron dynamics during ionization explain the primary and inner spider structures. Artwork by Ellen Keister and Daniel Hickstein. Adapted with permission from Ref. 2. ©2012 American Physical Society

An optical parametric amplifier [44] generates ultrafast pulses at 1300 nm (~ 1.3 mJ) and 2000 nm (~ 0.8 mJ) with pulse durations of ~ 40 fs.

The laser pulses are focused into the velocity map imaging (VMI) spectrometer to achieve peak intensities ranging from 5×10^{13} to 5×10^{14} W/cm². The focused laser beam ionizes gas-phase atoms

or molecules at a target pressure of approximately 10^{-2} Torr. Three electrodes arranged in a VMI geometry [51] drive photoelectrons towards a microchannel-plate-phosphor-screen detection system. A CCD camera (Pike 145b, Allied Vision Technologies) records the image of the phosphor screen, which is then Abel inverted using the BASEX algorithm [64] to obtain a 2D slice of the cylindrically symmetric 3D momentum distribution.

3.4 Photoelectron angular distributions from UV to mid-IR

Photoelectron angular distributions were recorded at various driving laser wavelengths between 262 and 2000 nm, and with intensities ranging from 5×10^{13} to 5×10^{14} W/cm². For driving wavelengths between 393 and 2000 nm, we observe interference structures aligned along the laser polarization axis (Figure 3.2a). These interference structures were observed by Huismans and coworkers [85], and interpreted in terms of the interference between laser-driven electron trajectories that collide with the ion (rescattered electrons) and electron trajectories that proceed directly to the detector (direct electrons). In this paper, we refer to these angular features as “spider structures” due to their resemblance to the body and legs of a spider. For driving laser wavelengths of 1300 and 2000 nm, we observe additional “inner spider” structures (Figure 3.2b) at low final momenta that have more closely spaced fringes. Unlike other low-energy angular structures reported in the literature [94–96] these inner spider structures are clearly visible through a wide range of intensities of the driving laser.

3.5 Plane-spherical wave model

To investigate the origin of both the primary and inner spider structures (Figure 3.2), we apply a simplified model of the electron-ion recollision process that we call the plane-spherical wave (PSW) model (Figure 3.3). In this model, the spider structures in the photoelectron angular distribution are modeled as the interference between a plane-wave electron wavefunction (Figure 3.3a) originating directly from the tunnel ionization of the atom, and a spherical-wave electron wavefunction (Figure 3.3b) that originates from the electron-ion rescattering event. By treating the phase evolu-

tion of the quantum wave function during its propagation semiclassically (the so-called intrinsic or quantum phase studied in high-harmonic generation (HHG) [97]), we can reproduce the outer spider structures (Figures 3.3c, and 3.4).

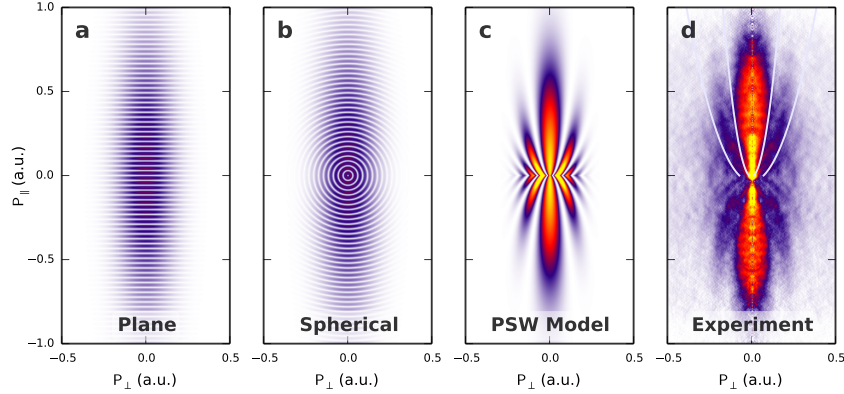


Figure 3.3: **The plane-spherical wave (PSW) model.** The superposition of a plane wave (a) and a spherical wave (b) generates an interference pattern (c) that has the same shape as the spider structures. The phase of the plane wave is given by $\Psi_{\text{plane}} \propto e^{ikP_{\parallel}}$, while the phase of the spherical wave is given by $\Psi_{\text{spherical}} \propto e^{ikP_{\text{total}}}$, where P_{\parallel} is the momentum parallel to the laser polarization, $P_{\text{total}} = \sqrt{P_{\parallel}^2 + P_{\perp}^2}$ is the total momentum, and k is the modulation frequency of the plane and spherical waves. Only the real part of the complex value is shown in panels (a) and (b) while the square of the absolute value is shown in panel (c). (d) The minima of the spider structure calculated using the plane spherical model (white lines) match very well with the experimental data across a broad range of wavelengths and intensities (shown: 1300 nm, 5×10^{13} W/cm², 40 fs driving laser). Adapted with permission from Ref. 2. ©2012 American Physical Society

In addition, by explicitly considering that the electron can pass by the atomic core more than once before rescattering, the PSW model can also explain the origin of our newly observed inner spider structures. These inner-spider structures arise from higher-order electron-ion rescattering events, with a characteristic fringe spacing that depends on the number of electron revisits to the vicinity of the ion before interacting strongly enough to rescatter. Through this interpretation, we can define a series of higher-order recollision cutoff energies that are a generalization of the ponderomotive cutoffs postulated first for HHG [30, 92] and then for strong field ionization [98, 99]. This extremely simple model can reproduce the gross features of our experimental photoelectron angular distributions across a very broad range of wavelengths, providing valuable physical insight into strong-field ionization physics.

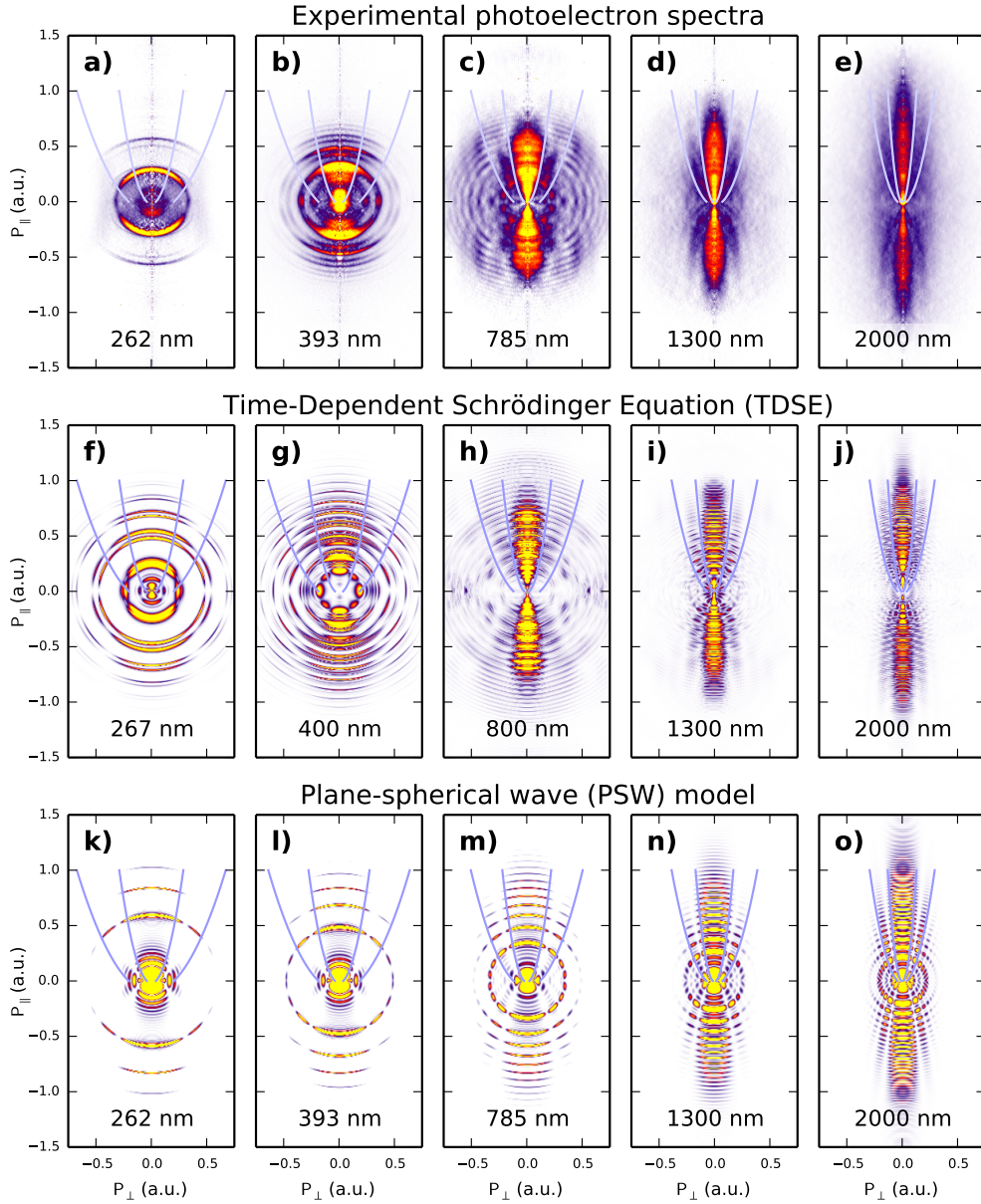


Figure 3.4: **Comparison of experiment, time-dependent Schrödinger equation (TDSE) simulations, and simple PSW theory.** (a-e) The experimental photoelectron angular distributions at $\sim 10^{14}$ W/cm² demonstrate how the ionization process moves from the multiphoton regime at short wavelengths to the tunneling regime at longer wavelengths. The spider structures can be most clearly seen at 1300 nm, though they are also visible at 800 and 2000 nm. (f-j) The spider structures also appear in the numerical TDSE simulations, which also reveal how the alternating nodal structure in the multiphoton-like ionization at 262 and 400 nm morphs into the spider structures at longer wavelengths. (k-o) The spectra simulated using the plane-spherical wave (PSW) model (see Figure 3.3) show remarkable agreement with the TDSE and experiment despite ignoring the effects from the ionization step and simplifying the interaction with the Coulomb potential to a single scattering step. The lines drawn on all of the plots correspond to the minima of the spider structures as predicted by the PSW model.

To develop the PSW model, we begin with the three-step (recollision) model of strong-field HHG, which starts with tunneling ionization of an electron from the neutral atom in the presence of a strong laser field (Figure 3.2c). Next, the electron moves under the influence of the driving field, first being accelerated away from the parent ion and then driven back towards the ion (Figure 3.2d). Depending on the phase of the laser field when the electron tunnels, the electron may return to the vicinity of the parent ion, or it may drift away. Recently it has been shown that the spider structures can be reproduced by completing numerical trajectory simulations assuming that electrons born with low transverse momentum can scatter elastically from the ion (Figure 3.2e), a method referred to as the generalized strong-field approximation (GSFA) [85].

The PSW model (Figure 3.3) further simplifies the computationally intensity GSFA model to by treating the revisiting electrons as a simple plane wave in the final momentum space and treating the rescattered electrons as a spherical wave in the final momentum space. In the PSW model, the only thing that needs to be calculated is the spatial modulation frequency of the plane and spherical waves on the detector, i.e., the dependence of the phase of the electron on the final momentum. In the Lewenstein model [93, 97] the phase of an ionized electron is $e^{-iS/\hbar}$, where S is the semiclassical action, given by

$$S(p, t, t_b) = \int_{t_b}^t \left(\frac{p(t')^2}{2m_e} + I_p \right) dt', \quad (3.1)$$

where I_p is the ionization potential of the atom or molecule, m_e is the mass of the electron, t_b is the time the electron tunnels into the continuum, and $p(t')$ is the momentum. Thus, the probability of observing an electron at some position on the detector can be found by integrating all of the classical trajectories that reach the same final momentum and adding them coherently. In practice, this means that the Equation 3.1 must be integrated up until the time when the electron rescatters from the ion, after which both electrons take identical paths to the detector. In the PSW model, the situation is further simplified because the calculation need only be completed in one dimension: along the component of electron momentum in the direction of the laser polarization direction (P_{\parallel}). This analysis is shown in Figure 3.5b, which plots the action S versus P_{\parallel} , accumulated in the time between ionization and the time at which the electron returns to the ion core at its lowest recollision

velocity v . The slope of this line corresponds to the modulation frequency of the plane and spherical waves in the PSW model, which, in turn, determines the spacing of the interference fringes in the spider structure. To simplify the analysis, we make the approximation that this slope is stepwise constant.

This simple procedure generates interference patterns that quantitatively reproduce the spacing and shape of the spider structures seen in the experimental data. As shown in Figure 3.2a, the predicted minima are in excellent agreement with the experimentally observed interference minima. This agreement is achieved with no fitting parameters – the structures are generated from first principles with minimal computational effort. The calculation requires only the wavelength and intensity of the driving laser and the ionization potential of the atom. This shows that, although the shape and spacing of the spider structures do not depend strongly on the structure of the atom or molecule, the PSW model suggests that structural information will be encoded in the momentum-dependent ratio between the plane wave and the spherical wave.

3.6 Inner spider structures

In addition to reproducing the shape of the primary spider structures, the PSW model also offers a simple explanation for the inner spider structures (Figure 3.2b). By examining Equation 3.1 and Figure 3.3b, it is clear that there is a relationship between the different amounts of time that the various electron trajectories spend in the continuum and the spacing of the spider structures that are generated. Using this relationship, we can explain the experimentally observed inner spider structures as resulting from electrons that spend significantly more time in the continuum before rescattering. More specifically, we conclude that the distinct inner spider structures are created by electrons that re-encounter the ion a specific number of times before scattering from the ion. Electron trajectories that arrive at the detector with low final momenta correspond to electrons that are ionized near the peak of the laser field and can revisit their parent ion more than once (Figure 3.5a). The PSW model allows us to easily compute the spacing of the spider structures that would result from each type of trajectory and compare this spacing to the experimental photoelectron

angular distribution (Figure 3.5f).

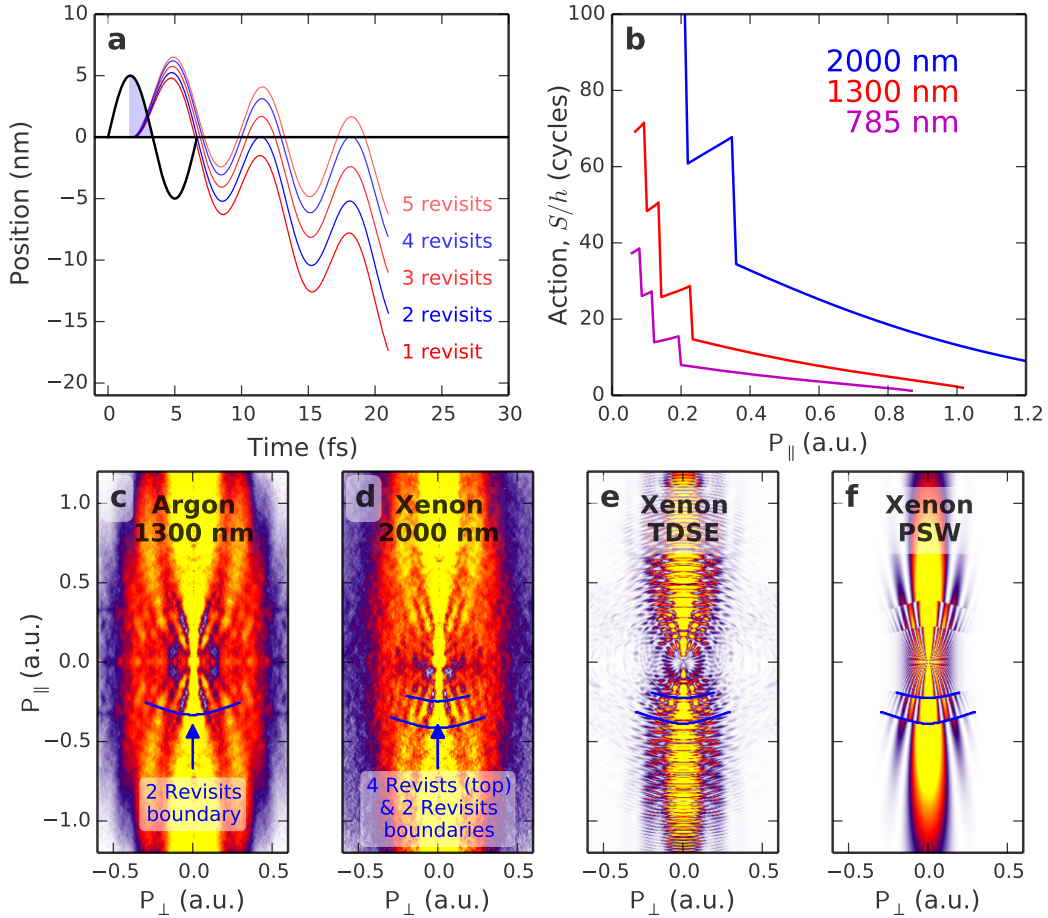


Figure 3.5: **Multiple scattering of the electron with the ion.** (a) Depending on when an electron is born into the continuum, it will be driven past the ion a specific number of times. (b) Quantum phase obtained by integrating each electron trajectory from when it is born to when it revisits the ion for the second-to-last time versus the final momentum parallel to the laser polarization (P_{\parallel}). The frequency of the plane and spherical waves is given by the slope of this graph. The steps at low momenta correspond to regions of multiple rescattering. (c) Experimental photoelectron distribution from argon ionized by a $1.3 \mu\text{m}$, $7.5 \times 10^{13} \text{ W/cm}^2$ laser shows a clear boundary between the high momentum region where only one revisit is possible and the low-momentum region where scattering can take place during a subsequent revisit. (d) Photoelectron distribution from xenon using a $2.0 \mu\text{m}$, $5 \times 10^{13} \text{ W/cm}^2$ laser displays clear boundaries that correspond to the second and fourth revisits. (e) TDSE calculations reproduce the low-momenta structures in xenon. (f) Single-cycle PSW model, including scattering on the first revisit (outer spiders) as well as the second and fourth revisits (inner spider structures). Adapted with permission from Ref. 2. ©2012 American Physical Society

This simple picture provides insight into the physics of the recollision interaction. Simple

classical calculations (Figure 3.5a) show that subsequent revisits of the ionized electron to the core take place with lower velocities. Since slower trajectories will be more influenced by the Coulomb potential, it is reasonable to assume that the main scattering event will take place during one of the final two laser-driven re-encounters with the ion, since these two re-encounters take place with the lowest velocity. The second to last encounter occurs with lower velocity since the oscillation and drift directions are opposite. By carefully measuring the spacing of the inner spider structure in the experimental photoelectron spectra and comparing with the results of the simple PSW model (Figure 3.2g), we can conclude from our data that scattering on the second-to-last re-encounter does indeed play the most significant role. In other words, if an electron makes three passes near the ion in the longitudinal direction, it is most likely to scatter strongly on the second pass. Thus, we can reproduce the experimental spider structures by integrating each electron trajectory from the time that the electron tunnels into the continuum to the time that it re-encounters the ion for the second-to-last time (Figure 3.5b).

For high-final-momenta trajectories, there is no change in the resulting photoelectron distribution, since these trajectories encounter the ion only once. Thus, the main spider structures are preserved at high final momenta, in good agreement with experiment. However, for low-final-momenta trajectories, the spacing of the spider structure becomes narrower in discrete steps that correspond to the classical boundaries between trajectories that are driven past the ion multiple times and scatter on the second-to-last revisit.² The calculated spacing of the spider structure inside the first boundary (Figure 3.5f) is approximately half the frequency of that outside, in good agreement with experiment (Figure 3.5c).

² One might object to the term “multiple rescattering” to describe the process of scattering on a high-order revisit, since it seems to imply that the electron is scattering many times from the ion, while the model proposed above only incorporates one scattering step. However, considering the electron trajectories in a classical model: in order to interact with the Coulomb potential of the ion strongly on a high-order revisit, the electrons *must* undergo a slight angle change on the first revisit so that it may then pass more closely to the ion on a later revisit. Thus, while we model the multiple rescattering process as only involving one strong scattering step, it is necessarily a more complicated process of soft “Coulomb focusing” on low-order revisits followed by strong scattering on subsequent revisit.

3.7 Measurement of the quantum tunnel distance

The cutoff energies for various numbers of revisits can be easily calculated using classical mechanics (Figures 3.1c-f). If we assume that electrons tunnel at $x = 0$ and ignore the effect of the Coulomb potential after ionization, then electrons with kinetic energy greater than $0.09 U_p$ will revisit only once, electrons with energy between 0.09 and $0.06 U_p$ will revisit three times (scattering on the second revisit), and electrons with energy less than $0.06 U_p$ will revisit five or more times (scattering on the forth, or subsequent even-numbered revisit). However, the predicted position of the cutoff is slightly lower than that observed in the experimental photoelectron spectra unless the finite tunnel distance is taken into account.

The tunnel distance results from the fact that electrons will be born into the continuum at a finite distance from the atom, which is dictated by the strength of the electric field and the ionization potential of the species (Figure 3.6a). The tunnel distance varies with the laser electric field, but at the peak of a laser field of intensity 5×10^{13} W/cm², it is on the order of 5 \AA for most atoms. If this finite tunnel distance is considered, the classical boundaries move to slightly higher energies, and are in better agreement with the experimental data (Figures 3.6b and A.3). To our knowledge, this is the first example where the finite tunnel distance inherent in strong-field ionization can be extracted from an experimental observable.

Interestingly, this simple model offers a straightforward explanation for the spike-like low-energy structure (LES) observed in previous time-of-flight studies [86, 87]. The location of the cutoff energy for three revisits matches perfectly with the position of the LES, which was found to scale with the Keldysh parameter $\left(\gamma = \sqrt{\frac{I_p}{2U_p}}\right)$ as $\gamma^{-1.8 \pm 0.1}$. Our simple model provides further insight, showing that, when the tunnel distance is taken into account, the cutoff energy for two revisits (E_{cutoff}) also depends on the ionization potential of the atomic species as

$$E_{\text{cutoff}} \propto 0.06 I_p \gamma^{-1.8}, \quad (3.2)$$

in perfect agreement with the experimental results (Figure 3.6). If we make the incorrect approximation that the electron originates at the position of the ion, then we would predict a γ^2 scaling. Thus,

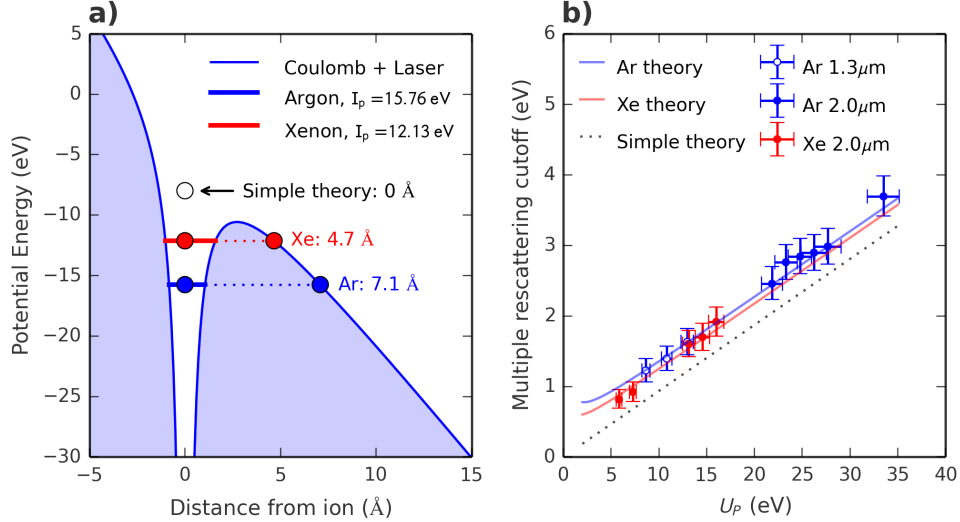


Figure 3.6: **Measurement of the quantum tunnel distance.** (a) In the presence of a strong laser field (5×10^{13} W/cm²), the atomic Coulomb potential is deformed, enabling tunnel ionization, where the tunneling distance is determined by strength of the laser field and the ionization potential of the atom. (b) By examining the classical equations of motion, we plot the theoretical cutoff between trajectories that revisit the ion once and those that rescatter several times (lines). If the tunnel distance is included, the theoretically predicted multiple rescattering cutoffs agree with the experimentally observed cutoffs (points). If the tunneling distance is ignored (simple theory, dashed line), the theory no longer agrees with the data. The experimental intensity was calibrated from the $2U_p$ cutoff and was assumed to be 10%. The error in the energy of the multiple rescattering cutoff was assumed to be 0.02 atomic units of momentum. Adapted with permission from Ref. 2. ©2012 American Physical Society

by observing a deviation from the γ^2 scaling, we observe this tunnel distance distance in our data. Other theoretical work has found that electrons that reach the turning point of their field-driven oscillation while in close proximity to the ion will result in a low-energy spike in the photoelectron distribution [100]. This further supports the notion that our predicted cutoff for the inner spider structures corresponds to the position of the peak in low energy electrons.

3.8 Conclusion

In conclusion, by generalizing the well-known three-step strong field ionization model using a simple plane-spherical wave model, we can intuitively explain the experimental photoelectron angular distributions of atoms ionized in strong laser fields. We show that newly observed low-energy features display clear signatures that an electron can pass by its parent ion more than once before strongly

scattering from it. Furthermore, the data show that when an atom is ionized by an intense laser, the electron emerges at a finite distance from its parent ion that corresponds to the far side of the quantum tunneling barrier. These new observations and physical explanations will inform future studies that seek to extract femtosecond-resolved structural information from strong-field ionization.

Chapter 4

Plasma Explosion Imaging

This chapter is adapted, with permission, from:

- D. D. Hickstein, F. Dollar, J. L. Ellis, K. J. Schnitzenbaumer, K. E. Keister, G. M. Petrov, C. Ding, B. B. Palm, J. A. Gaffney, M. E. Foord, S. B. Libby, G. Dukovic, J. L. Jimenez, H. C. Kapteyn, M. M. Murnane, and W. Xiong. Mapping Nanoscale Absorption of Femtosecond Laser Pulses using Plasma Explosion Imaging. *ACS Nano*, 8 (9), **2014**, 8810. DOI: 10.1021/nm503199v
©2014 American Chemical Society

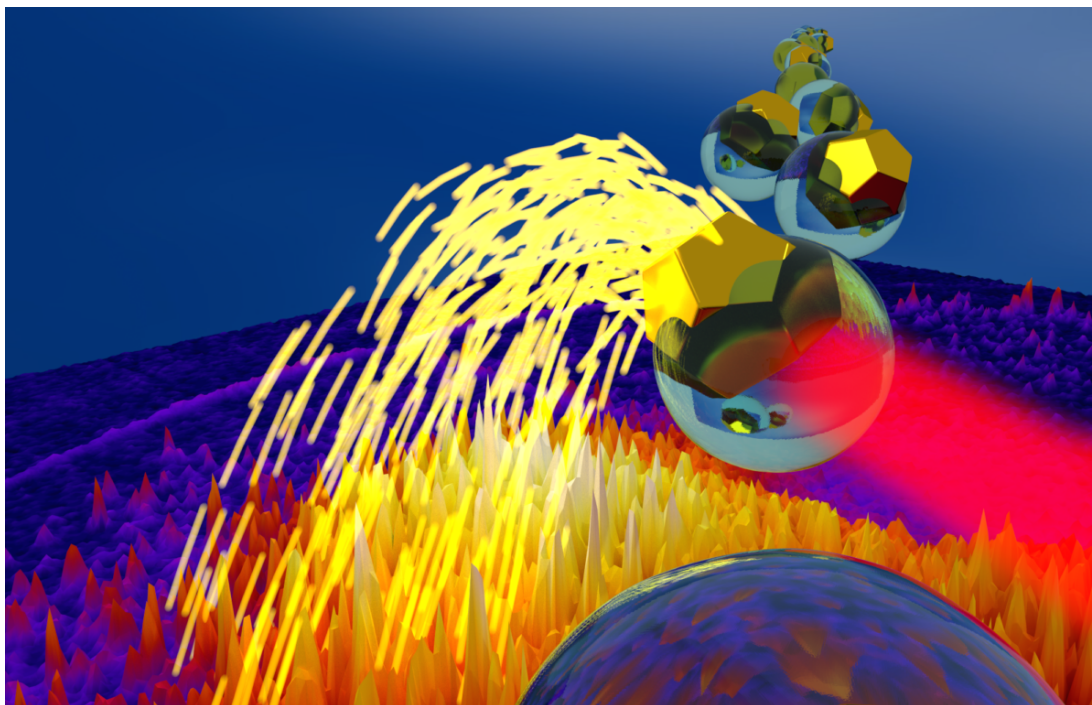


Figure 4.1: **Illustration of plasma explosion imaging (PEI) in a single nanoparticle.** A femtosecond laser pulse interacts with a single gold–dielectric composite nanoparticle, ejecting positive ions, which are recorded by a two-dimensional detector (bottom).

4.1 Abstract

This chapter describes the development of a new technique for investigating the interaction of nanostructures with strong laser fields: plasma explosion imaging (PEI). PEI enables the direct measurement of the highly localized light absorption that takes place in a single nanostructure irradiated by a strong femtosecond laser. By imaging the photoion momentum distribution resulting from plasma formation in a laser-irradiated nanostructure, PEI maps the spatial location of the highly localized plasma and thereby images the light absorption on the nanometer scale. This method probes individual, isolated nanoparticles in vacuum, which allows us to observe how small variations in the composition, shape, and orientation of the nanostructures lead to vastly different light absorption. In this chapter, we study four morphologically and chemically different nanoparticle samples with overall dimensions of ~ 100 nm and find that each sample exhibits distinct light absorption mechanisms despite their similar size. Specifically, we observe the following effects:

- Subwavelength focusing in single NaCl crystals
- Symmetric absorption in TiO₂ aggregates
- Surface enhancement in dielectric particles containing a single gold nanoparticle
- Hot spots in dielectric particles containing multiple smaller gold nanoparticles.

These observations (Figure 4.2) demonstrate how PEI directly reveals the diverse ways in which nanoparticles respond to strong laser fields, a process that is notoriously challenging to model because of the rapid evolution of materials properties that takes place on the femtosecond timescale as a solid nanostructure is transformed into dense plasma.

4.2 Introduction

4.2.1 Background

The interaction of strong ($>10^{13}$ W/cm²) laser fields with bulk materials has widespread applications, including precision machining on the sub-micron scale [101], the “green” synthesis of

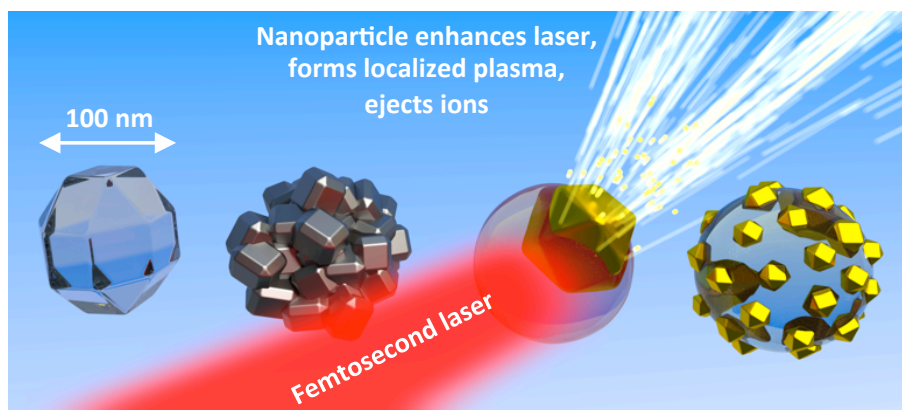


Figure 4.2: **Summary of PEI in four nanostructures.** PEI uses a femtosecond laser pulse to probe nanoparticles of different compositions, shapes, and orientations. Based on the structure of the particle, the electric field of the laser pulse is enhanced in a specific region of the nanoparticle. The location of the light-field enhancement can be deduced based on the direction(s) that ions are ejected. Adapted with permission from Ref. 3. ©2014 American Chemical Society

nanoparticles [102], and the production of high-energy electrons, ions and photons [103]. Nanoscale structures can locally enhance a laser field, often by many orders of magnitude [35], enabling the generation of strong laser fields that are localized on the nanometer scale, thus paving the way for breakthrough techniques and technologies. For example, gold nanoparticles are being designed to seek out cancerous tumors in the body and, when irradiated with a femtosecond laser, produce shock waves that destroy the tumor with minimal damage to nearby tissues [104, 105]. Additionally, several preliminary experiments have demonstrated the ability of laser-irradiated nanostructures to accelerate electrons, suggesting that nanomaterials may enable the fabrication of miniaturized particle accelerators [38, 40, 42, 106]. However, transforming these proof-of-principle concepts into practical technologies requires an advanced understanding of how nanostructures respond to light fields that are near the damage threshold.

For short-pulse laser intensities near and above the damage threshold ($\sim 3 \times 10^{13}$ W/cm² for glass [107], and roughly similar for most other dielectric materials) the interaction of femtosecond laser pulses with bulk materials is a complex process that is extremely challenging to model. The difficulties stem largely from the fact that the laser pulse modifies the optical properties of the material on the femtosecond timescale [108], requiring a model that incorporates the time-dependent

properties of the laser field, the solid material, and the newly formed plasma. Materials that exhibit nanoscale structure present a further challenge because features smaller than the wavelength of the light can enhance the electric field on the nanometer scale, and this effect depends strongly on the exact size, shape, and composition of the particle. For example, past work harnessed the ability of nanostructured targets to efficiently absorb laser light to create bright soft X-ray sources [109], but the detailed mechanisms of this enhancement could not be understood in detail because of the complexity of the interaction. Thus, there is pressing need for a direct measurement technique that can provide clear insight into how nanomaterials interact with laser fields.

4.2.2 Experimental approach

Making direct measurements of nanostructures irradiated with strong laser fields presents several experimental hurdles. First, when exposed to strong laser fields, nanostructures are damaged, and thus a fresh sample is required for each laser shot. Second, nanomaterial samples are rarely homogeneous, often varying widely in size, shape, composition, and surface roughness. Even small variations in the morphology of a nanostructure can have a dramatic effect on how the nanostructure responds to incident light fields. When particles of different sizes and shapes are probed simultaneously, these variations are obscured. Finally, the orientation of asymmetric nanoparticles relative to the laser propagation and polarization can dramatically influence how they interact with the light field.

Here we utilize a method that overcomes the experimental hurdles by imaging the localized nanoscale plasma that is created when an isolated nanostructure is irradiated with a short (40 fs), intense ($\sim 3 \times 10^{13}$ W/cm²) laser pulse (Figure 4.3). Instead of working with nanoparticles suspended in liquid solution or deposited on a surface, we employ a flowing aerosol of nanoparticles (Figure 4.3) that provides a fresh nanoparticle for every laser shot, thereby allowing us to use well-established angle-resolved-photoion-spectroscopy techniques [2, 4, 51]. Despite probing only a single nanoparticle each laser shot, many particles can be probed each second through the use of a high repetition-rate femtosecond laser (1 kHz in this study).

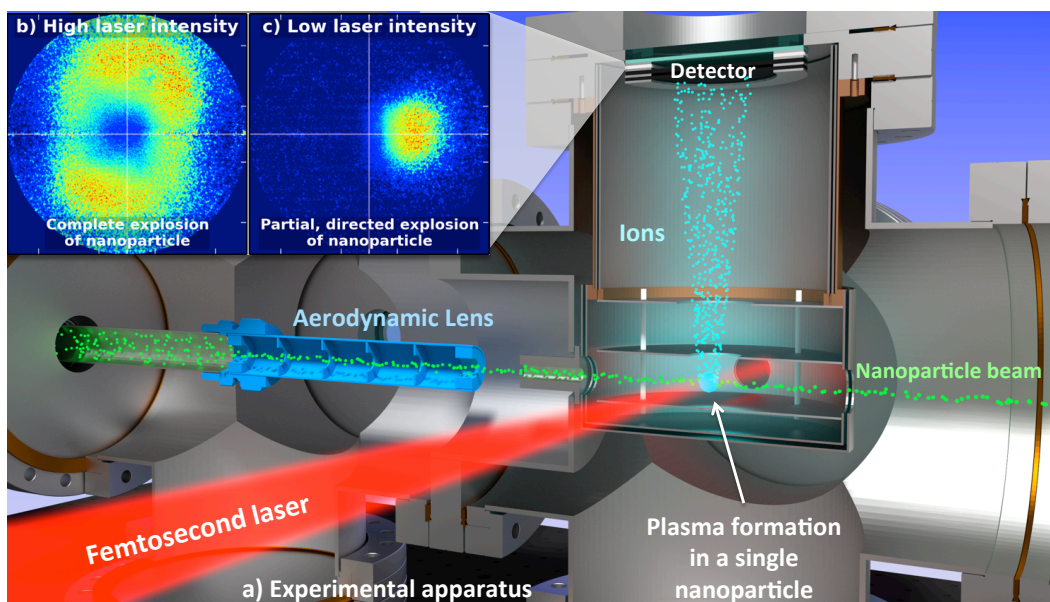


Figure 4.3: **Experimental apparatus for observing PEI in single nanostructures.** (a) The nanoparticle aerosol is introduced into the high-vacuum chamber by an aerodynamic lens that produces a collimated beam of nanoparticles. The nanoparticle beam is crossed with a tightly focused 40 fs laser pulse that interacts with a single nanoparticle. (b) When the nanoparticle encounters a region of high laser intensity ($>10^{14}$ W/cm²), it is completely transformed into a plasma that then ejects ions in all directions. (The apparent lack of ions in the center of the detector is a result of an inhomogeneous detector response.) (c) When the particle encounters a region of low laser intensity, a plasma is formed only in a localized region of the particle, and ions are ejected in a specific direction that depends on the structure, composition, and orientation of the particle. The photoions are collected by a velocity-map-imaging spectrometer and provide information about the localized electric fields in the nanoparticle. Adapted with permission from Ref. 3. ©2014 American Chemical Society

A key aspect of our approach is the use of laser intensities slightly below the plasma formation threshold of the bulk material; this creates a localized nanoplasma only within a specific region of a nanostructure. This method contrasts with previous studies [4, 38], which used laser intensities high enough to field-ionize the entire nanoparticle, creating a uniform plasma throughout the particle. Despite using laser intensities below the bulk plasma formation threshold, we do observe (localized) plasma formation in the nanoparticles. The formation of plasma at sub-threshold laser intensities occurs because of nanoscale field-enhancements, whereby the nanoparticle itself enhances the laser field in localized regions. Thus, while the average laser intensity is below the plasma formation threshold, some regions of the nanoparticle can experience light fields higher than threshold, and a plasma is formed only in these regions of the nanoparticle. The heated plasma is rapidly ejected

outwards from the surface of the nanoparticle, producing ions with momenta that correspond to the location of the plasma in the nanoparticle. Since we record a two-dimensional image of the angular distribution of the ions using an angle-resolved imaging detector, we refer to this technique as “plasma explosion imaging”. In the following examples, we show how PEI can be used to gain insight into the unusual and unintuitive light-absorbing properties of nanomaterials with a range of compositions and morphologies.

4.2.3 Summary of findings

Using this newly developed PEI technique, we observe dramatic differences in how nanoparticles of different compositions and shapes respond to intense laser fields. Specifically, we observe subwavelength focusing in NaCl, symmetrical absorption in aggregates of TiO₂ particles, and highly localized light absorption in gold–dielectric hybrid nanostructures. Surprisingly, we find that we can model light absorption in this strong-field regime using the finite-difference time-domain (FDTD) method, which has seen great success in modeling low-intensity light–nanoparticle interactions. This agreement suggests that many of the useful nanoscale optical effects that exist at low laser intensities (such as subwavelength focusing and plasmonic effects) will extend into the near-damage-threshold regime where they might be expected to breakdown. By demonstrating the nano-optical effects present at laser intensities near and above the material damage threshold, we pave the way for future developments that utilize the unique ability of nanoparticles to absorb, scatter, and focus light in the high-intensity regime.

4.3 Results and Discussion

4.3.1 Overview

A complete description of the sample preparation and experimental apparatus is found in Section B.2 (and Chapter 2) and is briefly summarized here. To perform photoion spectroscopy on isolated nanostructures, we employ an aerodynamic lens [70, 110, 111], which produces a collimated beam of nanoparticles from a nanoparticle aerosol and leaves the carrier gas divergent. A skimmer

then allows us to separate the carrier gas from the high-concentration beam of nanoparticles and thereby maintain high vacuum 1×10^{-6} Torr in the photoion spectrometer. The particle beam is irradiated with tightly focused, intense ($\sim 3 \times 10^{13}$ W/cm²), 785 nm, 40 fs laser pulses. Because of the tight focusing of the laser and the narrow width of the particle beam, the volume of the interaction region is only $\sim 10^{-7}$ cm³ (see Section B.2.1). Since the particle density is $\sim 10^5$ particles/cm³, only one laser shot in ~ 100 will hit a nanoparticle. Statistically, those pulses that do hit a nanoparticle, typically hit only one nanoparticle. The photoions produced from the laser-irradiated nanoparticles are collected by a VMI photoion spectrometer [2, 4, 5, 51, 108], which produces images of the ion momentum distribution.

To develop a broad understanding of how nanostructures of different shape and size interact with laser fields near the damage threshold, we prepared a range of nanoparticle aerosols starting with four different aqueous solutions: NaCl dissolved in water, ~ 5 nm TiO₂ nanoparticles suspended in water, 50 nm gold nanospheres suspended in water, and 17 nm gold nanospheres suspended in water. The nanoparticle aerosols were generated from the aqueous solutions using a compressed-gas atomizer, which produces droplets with an average diameter of ~ 1 μ m. Before entering the vacuum chamber, the droplets evaporate to leave single crystals (when using a salt solution) or aggregated nanostructures (when using a colloidal solution) consisting of one or more nanoparticles. The concentration of the material in solution determines the average diameter of the crystals (or the average number of nanospheres per aggregate).

4.3.2 Electron microscopy

To understand the morphology of the various nanostructures, we performed transmission electron microscopy (TEM) on nonirradiated nanostructures collected at the exact point where they would be probed by the laser. The TEM images reveal that the nanostructures that emerge from the aerodynamic lens are often quite different from the structures that exist in the solution phase (Figure 4.4). The NaCl solution produces particles with an average diameter of ~ 100 nm (Figure 4.4a). Since crystal faces are clearly visible in many of the particles, we conclude that most of

the nanoparticles are single crystals of NaCl, consistent with previous studies of salt aerosols [112]. The TiO₂ particles present as 50–100 nm aggregates of ~5 nm TiO₂ particles (Figure 4.4b). The aggregates form because many ~5 nm TiO₂ crystals are present in a single droplet. As the droplet evaporates, the nanoparticles clump into larger aggregates.

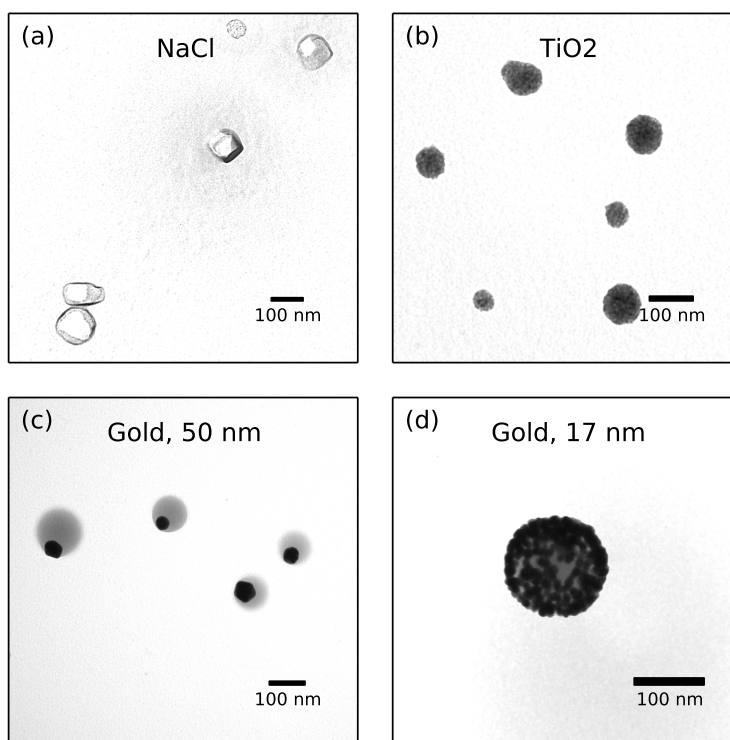


Figure 4.4: **Transmission electron microscopy (TEM) images of nanoparticles collected at the interaction region.** (a) The aqueous NaCl solution evaporates to form single crystals. (b) The solution of TiO₂ nanoparticles produces 50–100 nm diameter aggregates of ~5 nm particles. (c) The solution of 50 nm gold nanoparticles produces hybrid nanostructures consisting of a single gold nanoparticle (dark polygons) residing near the surface of a sphere of polyvinylpyrrolidone (PVP, gray circles). (d) The solution of 17 nm gold nanoparticles also generates hybrid gold–PVP nanostructures, but these nanostructures contain numerous 17 nm gold nanospheres. Adapted with permission from Ref. 3. ©2014 American Chemical Society

The morphology of the aerosol particles generated from the aqueous solutions of gold nanospheres is surprising; heterogeneous nanostructures are clearly seen in the TEM images (Figure 4.4c and d). For the solution of 50 nm gold nanospheres, the aerosol particles typically consist of one 50 nm gold nanosphere embedded near the surface of a ~100 nm sphere of lower-density material. The lower-density material is polyvinylpyrrolidone (PVP), an organic polymer that is added to the solution

by the manufacturer in a similar concentration to that of the nanospheres and serves to keep the nanospheres dispersed in solution.

The solution of 17 nm gold nanospheres also displays a heterogeneous morphology with gold spheres embedded in PVP (Figure 4.4d). However, the number concentration of the gold nanospheres is much higher, and the aerosol particles generated from this solution often contain ten or more gold nanospheres. Thus, while the composition of the 17 nm and 50 nm gold nanospheres samples is similar in aqueous solution, the aerosol particles display starkly different morphologies. Interestingly, for both the 50 nm and 17 nm gold nanosphere samples, the gold nanospheres are almost invariably located towards the outside of the PVP nanosphere.

4.3.3 Photoion spectroscopy

As shown in Figure 4.3, a collimated beam of nanostructures is introduced into the VMI spectrometer via the aerodynamic lens, and individual nanostructures are probed with femtosecond laser pulses. Though the focused laser has a Gaussian intensity profile, the full-width at half-maximum is on the order of 20 μm which is very large compared to the ~ 100 nm dimensions of the nanostructures used in this study and means that each nanoparticle experiences a laser field that is almost perfectly homogeneous over the dimensions of the nanoparticle. When the laser intensity exceeds $\sim 5 \times 10^{13}$ W/cm², the laser delivers enough energy to create a plasma in the entire nanoparticle (Figure 4.3b). In contrast, at intensities near 3×10^{13} W/cm², a plasma is formed only in a small region of the particle (Figure 4.3c). Since it is these localized plasma cases that provide information about the local-field enhancement, they are the focus of this work. Creating primarily localized plasmas is achieved by keeping the laser intensity in a range such that only the most intense regions of the laser focus are capable of creating a plasma in a nanoparticle.

The mechanism for plasma formation in solid-density materials irradiated with femtosecond pulses near the damage threshold is typically described as an avalanche ionization process [113–115]. First, a few free electrons are generated through multiphoton or tunnel ionization of the material (for conductors, free electrons already exist in the material). Next, these free electrons are

driven by the strong laser field and can reach kinetic energies exceeding the ionization threshold. When an electron impacts an atom, it can remove one or more electrons through electron impact ionization. The newly liberated electrons can then cause more ionization in an avalanche process. Both the initial ionization process and the avalanche ionization process scale exponentially with laser intensity [1] and, therefore, a small increase in the laser intensity in certain regions of the nanoparticle can have a very large effect on the ionization rate, and, in turn, determine if complete breakdown of the material will occur.

Given the field-driven avalanche breakdown mechanism, it is conceivable that any ionization within the nanoparticle would create free electrons, which could then ionize neighboring atoms, initiating rapid ignition over the entire nanostructure. However, the excursion distance of a free electron driven by a 785 nm laser field at an intensity of 5×10^{13} W/cm² is only ~ 1 nm. In addition, we estimate the plasma temperature to be approximately 5 eV [4], which does not provide the thermal electrons enough kinetic energy to propagate more than a few nm during the laser pulse. Consequently, the free electrons cannot travel to all regions of a 100 nm nanoparticle during the duration of the laser pulse. Rather, at intensities near the damage threshold, avalanche breakdown stays localized near the region of initial ionization, which is the region that experienced the highest local field. Thus, the physical location of the localized plasma serves as a map of the locally enhanced laser field that caused the avalanche breakdown (Figure 4.5).

After the laser pulse is over (< 0.1 ps), the region of localized plasma rapidly expands on the picosecond timescale, attempting to eject ions in all directions [4]. However, those ions that are launched inwards (towards the undamaged material) cannot penetrate the material (because of their low kinetic energy) and do not reach the detector. We observe only ions that are launched away from the undamaged regions of the nanostructure. As a result, we can interpret the angular features in the photoion momentum distribution as a direct result of spatial location of the localized plasma in the nanostructure. The photoelectrons can provide similar information to the photoions (Section B.3), but with somewhat less resolution due to the increased scattering of the electrons compared to the ions. Thus, we choose to study the photoions primarily. Using mass spectrometry (Section B.4),

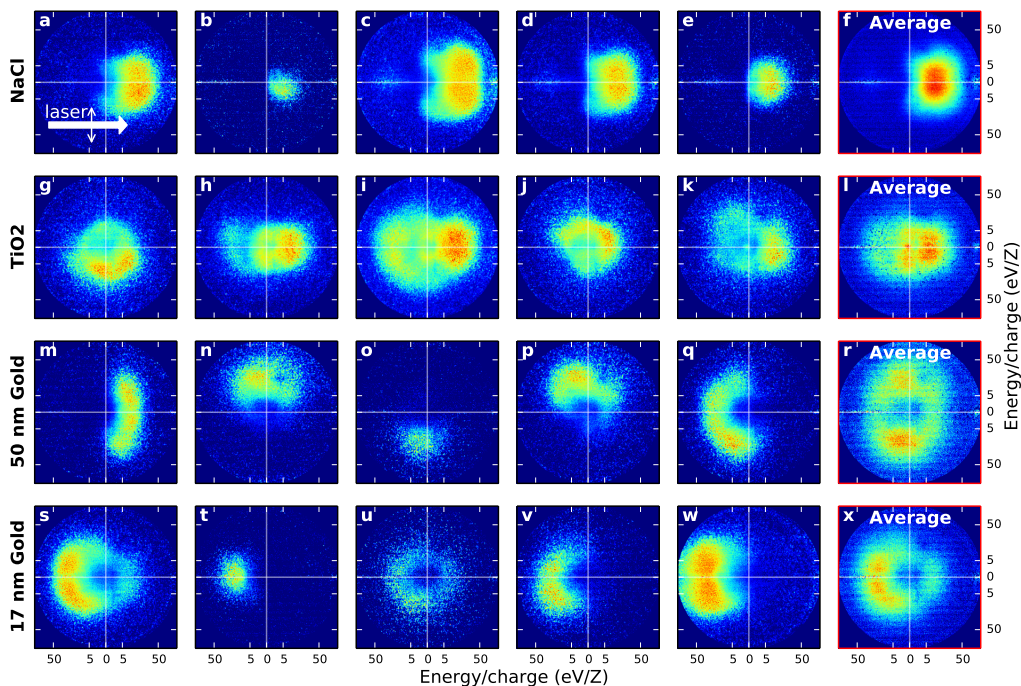


Figure 4.5: **Photoion angular distributions (PADs) from individual nanostructures show ions ejected in different directions.** The laser propagates from left to right and is polarized in the vertical direction, although no polarization dependence is observed in this study. (a–e) The photoions from ~ 100 nm NaCl crystals are ejected in the laser propagation direction, suggesting a focusing effect. (g–k) The ions from TiO_2 aggregates are typically centered around zero kinetic energy, indicating mostly symmetric plasma formation. (m–q) Ions from 50 nm gold nanoparticles embedded in a larger PVP sphere eject ions with directions that depend on the orientation of the nanostructure. (s–w) Photoions from 17 nm gold–PVP nanostructures eject ions in the direction opposite of the laser propagation, indicating absorption of laser energy on the front (illuminated) side of the nanoparticle. The averaged images (f,l,r,x) correspond to 70, 869, 419, and 108 particles respectively, and reveal general trends, but conceal the diversity of the individual particles, especially in the case of the 50 nm gold sample. Adapted with permission from Ref. 3. ©2014 American Chemical Society

we confirm that the photoions that reach the detector are primarily from the nanoparticles and not from other sources, such as the background gas.

For all of the nanostructure samples investigated, we observe considerable hit-to-hit variations in the photoion angular distributions (Figure 4.5), reflecting the differences in the shape, composition, and orientation of the particles. Despite the hit-to-hit variations, we can easily spot general trends in the direction of ion ejection in the four samples presented here. These trends are summarized in Figure 4.5, and confirmed via the center-of-mass distributions presented in Figure 4.6. To understand

the physical origin of the localized light absorption in each nanostructure, FDTD methods were used to simulate the interaction of 785 nm femtosecond pulses with the nanomaterials (Figure 4.7 and Section B.2).

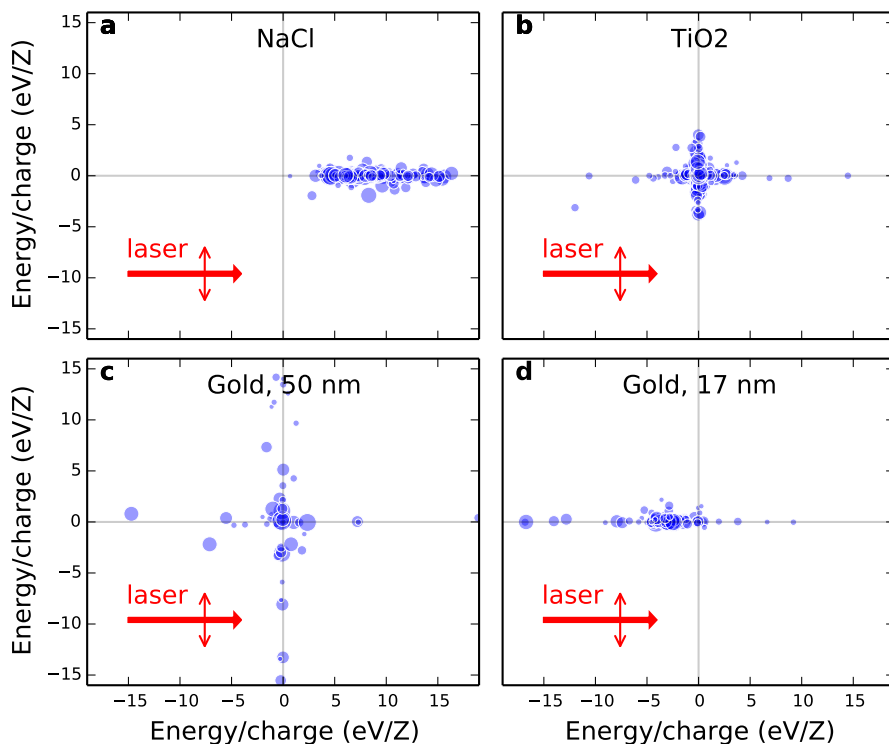


Figure 4.6: **Position of the center of mass (CoM) of each PAD for the various nanoparticle samples.** The position of each dot indicates the CoM of the photoion distributions and larger sizes correspond to higher ion yield. (a) NaCl particles act as lenses, focusing the light onto the backside of the particle and ejecting ions primarily in the laser propagation direction. (b) TiO₂ undergoes plasma formation over the entire particle, generating plasma explosions that are largely symmetric about zero kinetic energy. (c) The 50 nm gold nanosphere samples produces composite nanostructures consisting of gold nanospheres embedded in a dielectric material. A plasma is preferentially formed in the gold nanosphere and explodes outward, ejecting ions in a direction that depends on the orientation of the nanostructure, but not on the laser polarization or propagation directions. (d) The 17 nm gold nanosphere sample forms aggregate nanostructures consisting of many gold nanospheres that absorb mainly on the illuminated face and eject ions opposite the direction of laser propagation. Adapted with permission from Ref. 3. ©2014 American Chemical Society

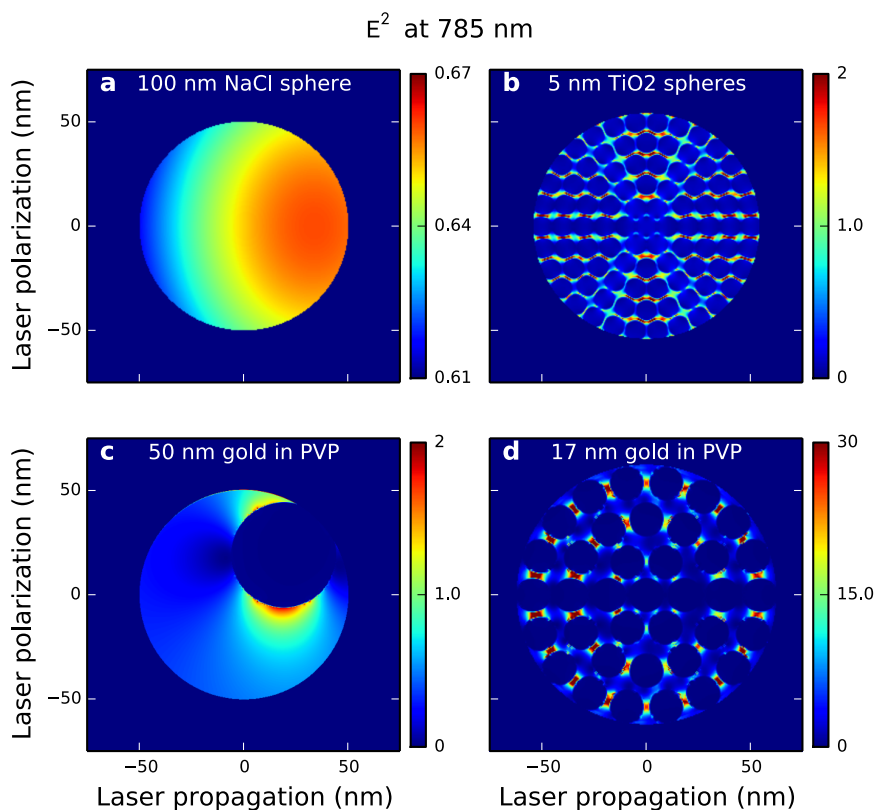


Figure 4.7: **Finite-difference time-domain (FDTD) simulations of the electric field intensity inside of the various nanostructures.** The laser propagates from left to right and the colorscale is in units of the incident field intensity. Plasma formation is most likely to occur near the regions of highest electric field. (a) In the NaCl particles, the laser field is enhanced by approximately 10% on the side opposite of the light source. (b) In the TiO₂ aggregates, the highest electric field is in the regions between the TiO₂ particles and does not have a preference for the laser polarization or laser propagation directions. (c) For the 50-nm-gold-PVP nanostructures, the electric field is enhanced substantially near the surface of the gold nanoparticle, which ignites localized plasma formation in the dielectric material. (d) In the 17-nm-gold-PVP nanostructures, the light field is greatly enhanced in hot spots between the nanospheres, and higher fields are seen on the illuminated side of the nanostructure. Adapted with permission from Ref. 3. ©2014 American Chemical Society

4.4 Case studies of nanoscale light enhancement

4.4.1 NaCl crystals: nanofocusing in dielectric nanomaterials

In the case of the ~ 100 nm NaCl crystals, ion ejection is observed almost exclusively in the forward direction, i.e., the direction of laser propagation (Figures 4.5a and 4.6a). This effect is the opposite of what is expected for an opaque macroscopic object, which would absorb light primarily

on the illuminated side and eject material back towards the laser. It is also different from what is expected at laser intensities well above the damage threshold, where the high electron densities would cause the resulting plasma to act like a metal, again absorbing energy on the surface facing the laser. Instead, we observe that a ~ 100 nm NaCl crystal acts like a lens, focusing the light onto itself and forming a plasma on the back side. Of course, strictly speaking, we cannot apply the term focusing in this case, since geometric optics does not describe the interaction of light with objects smaller than the wavelength. However, numerous studies of photonic nanojets [116–120] have confirmed the ability of nanoparticles to concentrate visible light on length scales far smaller than the wavelength, a phenomenon referred to as subwavelength focusing.

Indeed, our FDTD simulations confirm the subwavelength focusing of the NaCl particles, revealing a $\sim 10\%$ increase of the light intensity on the backside of the particle compared to the front side (Figure 4.7a). While this increase is relatively modest compared to the intense lensing observed in micron-sized dielectric particles [117], our experiment is operated in a regime very close to the threshold for plasma formation, and a small increase in intensity can have dramatic effects on the highly nonlinear plasma formation process.

4.4.2 TiO_2 nanoclusters: light interaction with a particle ensemble

The overall size of the TiO_2 aggregates is similar to the NaCl crystals (both are ~ 100 nm in diameter). However, in contrast to NaCl, the ion ejection from the TiO_2 particles is generally symmetric about zero kinetic energy (Figures 4.5b and 4.6b). This effect cannot be explained by a difference in the material properties, because both TiO_2 and NaCl are transparent materials with a bandgap larger than the photon energy. Given this similarity, one would expect TiO_2 to exhibit the same subwavelength focusing that takes place in NaCl. The different response must then be due to the fact that the large TiO_2 aggregates are composed of many ~ 5 nm crystals instead of a single large crystal. Our FDTD simulations (Figure 4.7b) reveal considerable enhancement of the electric field between the 5 nm TiO_2 nanoparticles, but show no preference for the front or back of the 100 nm aggregate. There are two effects that cause the lack of focusing in the TiO_2 aggregates.

First, the strong enhancement between adjacent ~ 5 nm TiO_2 particles likely overpowers any small focusing effect that is seen within the TiO_2 particles. Second, the TiO_2 particles are significantly smaller than the NaCl nanoparticles (5 nm versus 100 nm diameter) and therefore they are further from the regime of geometric optics and will experience a more homogeneous internal field. Thus, by simply changing from a single crystal to a similarly sized aggregate of smaller particles, we can completely change the light absorption properties of the material, even at a scale much smaller than the wavelength of the light.

4.4.3 50 nm gold nanoparticles: field enhancement at the surface

The gold–nanosphere–dielectric hybrid nanostructures are of particular interest, because the 50 nm and 17 nm gold nanoparticle samples are identical in chemical composition but exhibit vastly different properties because of their different morphologies. For 50 nm gold nanostructures, the ion explosions are directional, but the direction is random with respect to the laser (Figures 4.5c and 4.6c). Explosions were observed in the direction of laser propagation, in the opposite direction, and in orthogonal directions, all with equal probability. Thus, the direction of the explosion is not set by the laser, but by the spatial orientation of the nanostructure.

Gold nanoparticles are well known to enhance the electric field at their surface [116, 121–123], and this enhancement likely ignites the plasma formation process in the vicinity of the gold nanosphere. Additionally, being metal, the gold particles already have conduction band electrons, which are freely driven by the laser and absorb energy through collisions with the ions. Thus, the heating of the gold nanosphere will begin before the laser pulse has reached maximum intensity, in contrast to the PVP, which must be ionized before it can strongly absorb energy from the laser pulse. Both of these effects lead to a strong absorption of laser energy in the immediate vicinity of the gold nanosphere, which leads to a localized plasma formation. This localized plasma creates a directional ion ejection in a direction set by the orientation of the nanostructure. This rationalization is confirmed by the FDTD simulations (Figure 4.7c), which reveal that the laser field is enhanced by more than 200% near the surface of the gold nanoparticle.

4.4.4 17 nm gold nanospheres: asymmetric hot-spots

Interestingly, the 17-nm-gold–PVP hybrid nanostructures display completely different behavior than 50 nm gold nanostructures; for the 17 nm sample, the ions are ejected primarily in the backwards (opposite of the laser propagation) direction (Figures 4.5d and 4.6d). The difference stems from the fact that the 50 nm sample produces nanoparticles that contain only one gold nanosphere, while the 17 nm sample produces PVP nanoparticles that contain numerous 17 nm gold spheres. Since the 17 nm spheres are located in close proximity to one another (Figure 4.3d), the electric field can be enhanced by nearly an order of magnitude in the regions between the gold nanospheres (Figure 4.7d). It is likely that the plasma formation takes place in the PVP in the electric field hot spots [124] between the gold nanoparticles. The FDTD calculations reveal that these hot spots are most pronounced on the illuminated side of the aggregate, suggesting that plasma will preferentially form on this face of the particle. In analogy to geometric optics, it appears that the gold nanoparticles on the illuminated side are blocking the light from reaching the back side of the particle.

4.5 Future directions

In this study we focused on laser intensities near the ablation threshold and, consequently, we were able to successfully simulate the laser ablation process using numerical methods that ignore the changes in the material properties that take place at high laser intensities such as the nonlinear refractive index or the excitation of charge carriers to the conduction band. It is likely that such effects begin to dominate as the laser intensity is increased. Future studies could utilize the plasma explosion imaging technique to search for these nonlinear effects at laser intensities well above the plasma formation threshold. Indeed, a close examination of Figure 4.3b reveals that, while the high-intensity explosion of the nanoparticle ejects ions in all directions, it is not completely homogeneous. Thus, the plasma explosion imaging method can likely provide information about laser–nanoparticle interactions at intensities well above the damage threshold.

4.6 Summary

We have demonstrated a new technique called plasma explosion imaging, where we use strong femtosecond laser fields to create a localized plasma within isolated nanoparticles and use the momentum of the ejected ions to infer the location of this plasma within individual nanoparticles. The location of the plasma indicates where the electric fields are enhanced in the particle and provides a map of the nanoscale light absorption at laser intensities near the damage threshold. We apply this novel method to observing sub-wavelength focusing in NaCl, symmetric plasma formation in TiO₂ clusters, and highly localized plasmaformation in gold–dielectric hybrid nanostructures. Figure 4.8 presents a summary of the different light absorption mechanisms observed in the various nanostructures. In the future, this method can be easily extended to more complex nanostructures and higher laser intensities, providing further insight into the interaction of strong laser fields with nanomaterials.

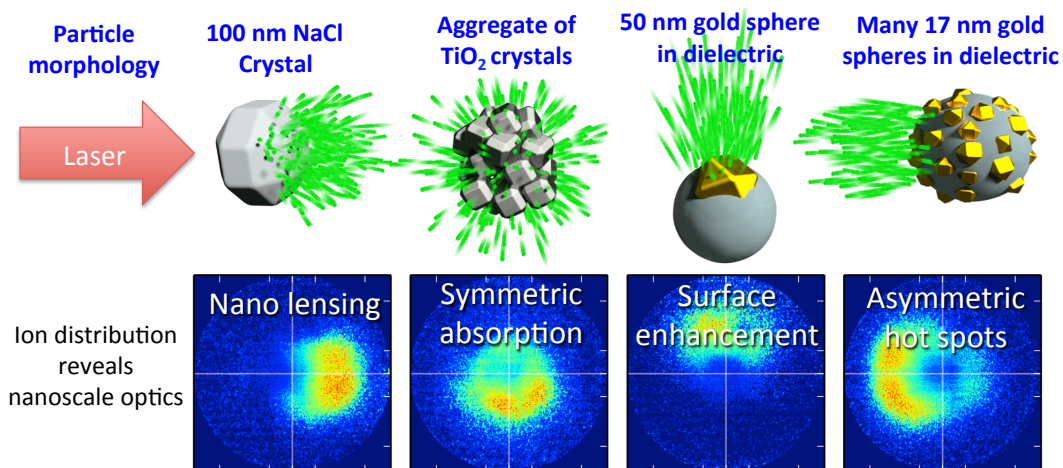


Figure 4.8: **Summary of nanoscale light absorption revealed through PEI.** While all particles presented here have similar diameters (~ 100 nm), they absorb light in different ways, form a localized plasma in different locations, and exhibit different characteristic photoion distributions, which indicate the light absorption mechanism for a single isolated nanoparticle. Adapted with permission from Ref. 3. ©2014 American Chemical Society

Chapter 5

Shock Waves in Nanoplasma

This chapter is adapted, with permission, from:

- D. D. Hickstein, F. Dollar, J. A. Gaffney, M. E. Foord, G. M. Petrov, B. B. Palm, K. E. Keister, J. L. Ellis, C. Ding, S. B. Libby, J. L. Jimenez, H. C. Kapteyn, M. M. Murnane, and W. Xiong. Observation and Control of Shock Waves in Individual Nanoplasmas. *Phys. Rev. Lett.*, 112 (11), **2014**, 115004. DOI: 10.1103/PhysRevLett.112.115004 ©2014 American Physical Society

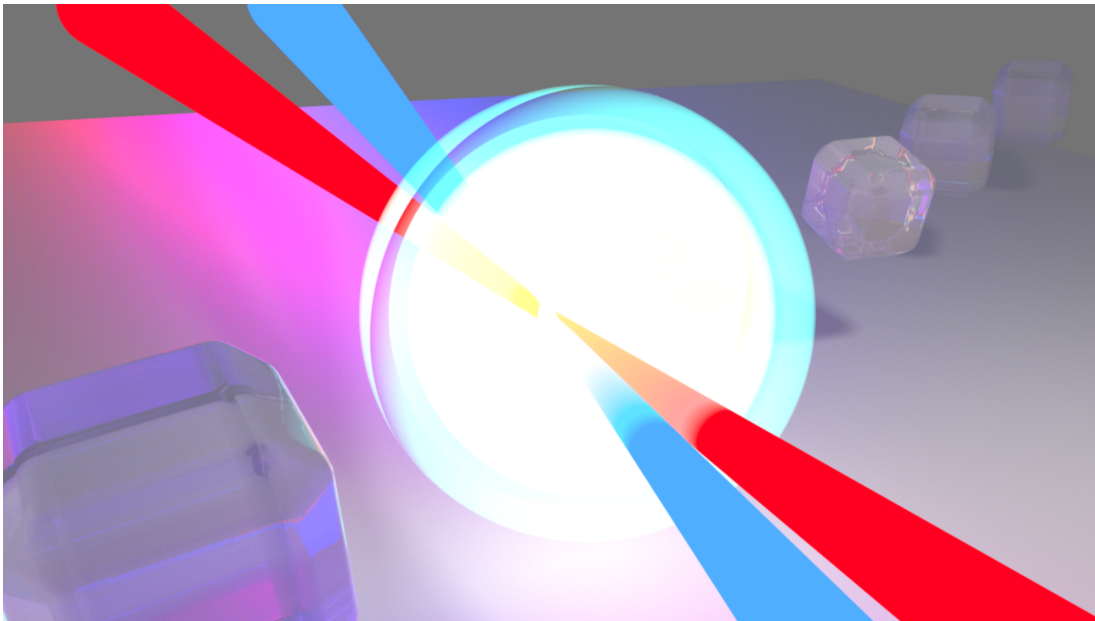


Figure 5.1: **Illustration of laser-driven shock wave in a nanoplasma.** A beam of ~ 100 nm NaCl crystals is crossed by two laser pulses (400 nm and 800 nm). The first pulse forms a nanoplasma and the second drives a shock wave through the nanoplasma.

5.1 Abstract

In a novel experiment that images the momentum distribution of individual, isolated 100-nm-scale plasmas, we make the first experimental observation of shock waves in nanoplasmas. We demonstrate that the introduction of a “heating” pulse prior to the main laser pulse increases the intensity of the shock wave, producing a strong burst of quasi-monochromatic ions with an energy spread of less than 15%. Numerical hydrodynamic calculations confirm the appearance of accelerating shock waves, and provide a mechanism for the generation and control of these shock waves. This observation of distinct shock waves in dense plasmas enables the control, study, and exploitation of nanoscale shock phenomena with tabletop-scale lasers.

5.2 Introduction

Nanoscale plasmas (nanoplasmas) offer enhanced laser absorption compared to solid or gas targets [37], enabling high-energy physics with table-top-scale lasers. Indeed, previous experimental studies have observed the production of high-energy ions [38], and even nuclear fusion [39] in laser-irradiated nanoplasmas. For more than a decade, theoretical studies have predicted that shock waves can be generated in nanoplasmas, and that these nanoplasma shock waves might allow for the practical generation of quasi-monoenergetic high-energy ions, neutrons from fusion processes, or ultrafast X-ray bursts [40–42].

In an analytical study, Kaplan, Dubetsky, and Shkolnikov [40] find that shocks should be a common phenomenon in expanding nanoplasmas, requiring only a plasma density distribution that is highest in the center and decays smoothly towards the edges. Similarly, Peano et al. [41, 125] used numerical simulations to show that the density profile of the precursor nanoplasma would dictate the properties of the shock. In particular, they demonstrated that a weak laser pulse could be used to shape the density profile so that a second, stronger laser pulse could produce more intense shock waves. However, until this work, nanoplasma shock waves have eluded experimental observation.

In contrast to the theoretical studies, which model a single nanoplasma, previous experimental

studies of nanoplasmas [38, 126] used laser focal volumes that contained many particles, thereby simultaneously irradiating nanoparticles of different sizes and with different laser intensities. As we show in this work, the kinetic energy of the shock wave depends on the plasma size and the laser intensity. Thus, studies that probe many nanoparticles simultaneously would create an ensemble of shock waves with different kinetic energies, thereby obscuring their identification as shocks.

In this chapter, by imaging individual laser-irradiated nanoparticles, we remove the size and intensity averaging present in previous studies, which allows us to clearly observe nanoscale plasma shock waves. Furthermore, we demonstrate that these shock waves can be controlled by using a laser pulse to shape the plasma density profile. Finally, we present hydrodynamic simulations that provide a mechanism for the generation and control of shock waves in nanoplasma.

5.3 Experiment

Our observation of shock waves in nanoplasma is enabled by a unique experiment (Figure 5.2) that can detect photoions from the nanoplasma generated from a single laser-irradiated nanoparticle. Nanocrystals of NaCl, KCl, KI, or NH_4NO_3 with diameters of ~ 100 nm are created using a compressed-gas atomizer and introduced into the vacuum chamber using an aerodynamic lens. A plasma is formed via illumination of a particle with a tightly focused 40-fs laser pulse (wavelength of either 400 nm or 800 nm) with an intensity that is adjusted between 3×10^{13} and 4×10^{14} W/cm². The angle-resolved energy distribution of the ions created by the expanding nanoplasma is recorded using a velocity-map-imaging (VMI) photoion spectrometer [2, 5, 51, 127] that records a two-dimensional projection of the photoion angular distribution (PAD).

Because the laser focal spot is small compared to the spacing between the nanoparticles, we probe, on average, one nanoplasma every 40 laser-shots (see Section 2.4.5). In all laser-irradiated nanoparticle experiments, each nanoparticle will experience a different laser intensity depending on where it is located in the laser focus, which leads to intensity averaging effects if each PAD contains ions from many nanoparticles, as was the case in previous nanoplasma studies [38, 114, 128]. However, in this experiment, each PAD corresponds to a single particle and, although the

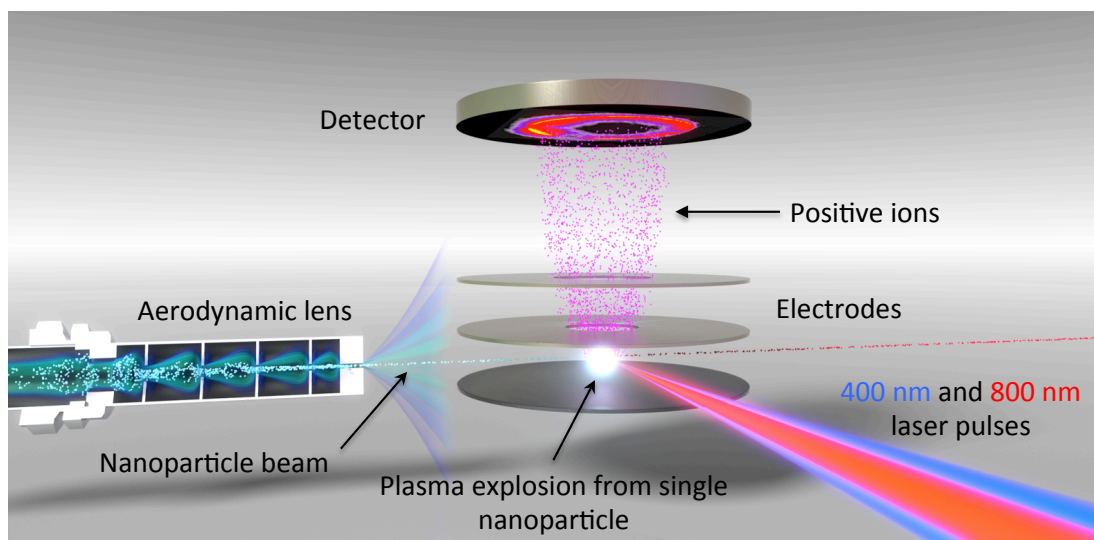


Figure 5.2: **Apparatus for imaging shock waves in individual nanoplasmas.** An aerodynamic lens focuses nanoparticles into a high-vacuum chamber where they are irradiated by a series of two time-delayed laser pulses. The first pulse creates an expanding nanoplasma, while the second pulse further heats the plasma, causing a pressure increase, which leads to shock wave formation. The resulting photoion momentum distribution is projected onto a microchannel-plate detector using three electrodes in a velocity-map-imaging geometry [51]. Art by Brad Baxley, JILA. Adapted with permission from Ref. 4. ©2014 American Physical Society

intensity cannot be precisely controlled for each particle, no intensity averaging takes place within a single PAD. This allows for the observation of previously undiscovered physical processes, even those that are exquisitely sensitive to laser intensity, particle size, or particle composition.

5.4 Results and Discussion

In our experiment, when the peak laser intensity is below $5 \times 10^{13} \text{ W/cm}^2$, the PADs contain only 100 or fewer ions, corresponding to the ionization of the residual N_2 and H_2O gas that flows with the particles through the aerodynamic lens. However, when the laser intensity is increased above $\sim 5 \times 10^{13} \text{ W/cm}^2$, we observe some PADs that contain more than 10^4 ions, indicating plasma formation in a single nanoparticle (Figure C.3). Indeed, in this intensity regime, solid nanoparticles are rapidly ($<1 \text{ ps}$) converted into dense nanoplasmas through the following mechanism [113–115]. First, the strong laser field causes some of the atoms to ionize through tunnel ionization [126], liberating about one electron per atom within a few tens of femtoseconds [1]. These free electrons

are accelerated by the strong laser field and then drive further rapid ionization through electron impact ionization [114]. The electrons continue to be driven by the laser field and absorb energy through collisions with the ions [129], reaching high temperatures.

When the laser intensity is increased above $\sim 1 \times 10^{14}$ W/cm², shock waves appear in approximately 10% of the nanoparticle PADs (Figures 5.3 and C.3). Each shock wave manifests as a sharp ridge on top of a broad photoion distribution. The ion kinetic energy of each shock ranges from 15 eV/Z to 50 eV/Z, where Z is the charge state of the positive ion. However, each individual shock is quasi-monoenergetic, with an energy spread of less than 15% (Figure 5.3b).

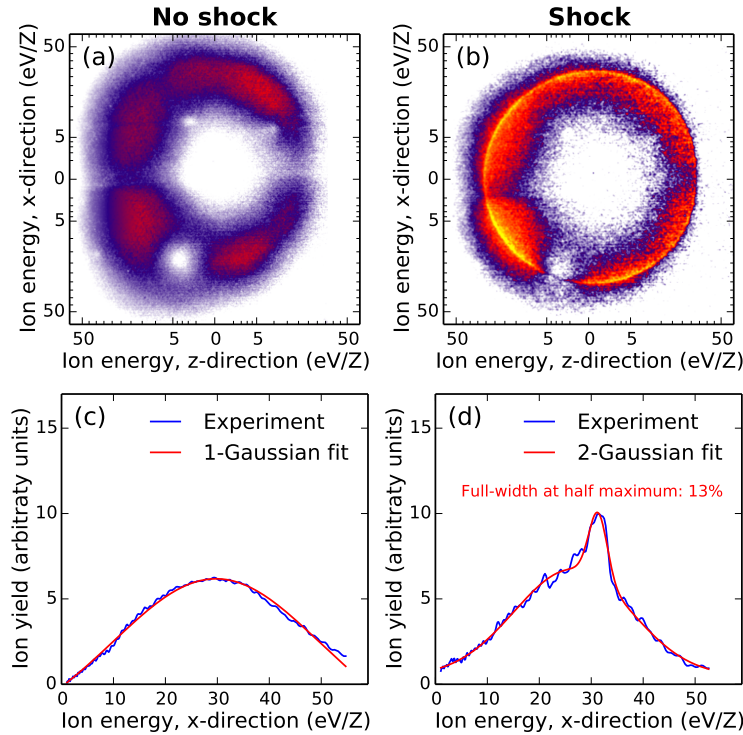


Figure 5.3: Experimental observation of shock waves in individual nanoplasmas. (a) The photoion angular distribution (PAD) from a single NH_4NO_3 nanoparticle irradiated with a pulse of 400 nm light followed by pulse of 800 nm light typically displays a broad ion distribution. Here the laser propagates in the z -direction (right-to-left) and is linearly polarized in the x -direction. The angular features are due to the inhomogeneous response of the imaging detector. (b) If the particle size, laser intensity, and laser pulse time-delay are tuned appropriately, a sharp shock wave (orange and yellow) appears in addition to the broad ion distribution. (c) The radial energy distribution of the typical nanoplasma explosion can be fit by a single broad Gaussian function. (d) The shock wave manifests as an additional sharp peak, which can be fit by a second Gaussian function with a narrow energy spread. Adapted with permission from Ref. 4. ©2014 American Physical Society

The formation of the shock waves is sensitive to both the physical size and chemical composition of the particle. We observe that larger nanoparticles are more likely to create shock waves (Figure C.2), which can be explained by the fact that larger nanoplasmas absorb more energy from the laser field [37]. Using a single laser pulse, shocks are observed in a variety of compounds, including KI, NaCl, and KCl, and the threshold laser intensity required to create shocks scales roughly with the ionization potential of the compounds (Figure C.3), as expected for the onset of tunnel ionization [1], and in agreement with the relative ionization yields observed in single-particle mass spectroscopy experiments [130]. For NH_4NO_3 , the compound with the highest ionization potential in this study, no shocks are observed in the single-pulse experiment (Figure 5.3), making it the ideal example case for demonstrating the two-pulse shock generation scheme.

Two laser pulses with an appropriate relative time delay can be used to create shock waves in all of the nanoparticles investigated in this study, including NH_4NO_3 . The likelihood of shock formation depends critically on the time delay between the first and second pulses. The minimal time delay for shock creation coincides with the peak in the total photoion yield, which occurs around 7 ps (Figure 5.4a). Similarly, the maximum time delay for shock production occurs near 45 ps, corresponding to the end of the enhanced ion yield. Previous studies [128, 131] observed a similar dependence of the photoion yield on time delay during the two-pulse irradiation of nanoparticles (although they did not observe shocks) and attributed this behavior to the increased absorption of the second laser pulse caused by the expansion of the plasma following the first laser pulse.

The expansion of our nanoplasma into the vacuum is significantly slower than previous studies due to the large size of the nanoparticles and can be estimated using the ion sound speed [126]

$$v_{\text{expand}} = \sqrt{\frac{ZkT_e}{m_i}}, \quad (5.1)$$

where Z is the charge of the ions, m_i is the mass of the ions, and kT_e is the electron temperature of the plasma. A 100 nm diameter particle composed of N^+ ions (mass of 14 Da each) with a temperature of 10 eV would double in size in 6 ps, in good agreement with the 7 ps delay for shock wave formation.

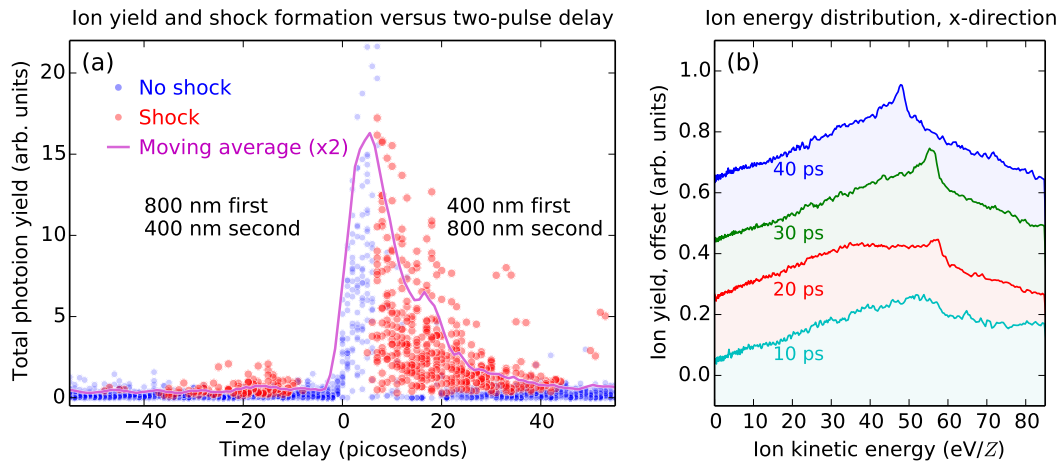


Figure 5.4: **Control of shock wave formation using two laser pulses.** (a) Each dot indicates a single nanoplasma explosion of an individual NH_4NO_3 nanoparticle as a function of the delay between the 400 nm and 800 nm laser pulses. The first pulse forms a slowly expanding nanoplasma, and the second pulse causes a rapid pressure increase inside of the nanoplasma, which leads to the formation of a shock wave. When the delay between the two pulses is greater than 7 ps, shock waves are formed. The ion yield is higher when the 400 nm pulse precedes the 800 nm pulse because the 800 nm pulse is more effective at heating the expanded nanoplasma. (b) As the relative time delay between the laser pulses is increased, the shocks become more pronounced. For comparison purposes, we display shocks with energies ~ 50 eV, though the shocks from different nanoparticles range between ~ 15 and 50 eV. Adapted from [4]. ©2014 American Physical Society

After the nanoparticle is irradiated by the first laser pulse, the resulting plasma expands, and its density assumes a radial profile that decays smoothly into vacuum. Energy absorption peaks when the electron density of the plasma is near the critical density [126, 132], the density at which electrons in the plasma are driven resonantly by the laser field. As the plasma expands, the volume of plasma near the critical density expands, enhancing energy absorption. Eventually, the entire nanoplasma drops below the critical density and light absorption is diminished. Thus, the arrival time of the second pulse relative to the first determines the amount of energy absorbed. The similar timescale of ion yield enhancement and shock formation suggests that the two effects share a common mechanism: the expansion of the plasma between the first and the second pulses is crucial for the formation of shocks in the two-pulse experiment.

The time delay between the laser pulses not only determines the presence of shocks, but also determines the fraction of ions that become part of the shock wave. The shocks produced with time

delays of ~ 10 ps involve a small fraction of the ions, while the shock generated using time delays of >15 ps contain a much larger fraction of the total ions (Figures 5.4b and C.4). This indicates that the first pulse is shaping the plasma density to achieve a density profile that is better optimized for shock wave propagation and generation of quasi-monoenergetic ions. Thus, this demonstrates that it is possible to control shock waves in plasmas by actively sculpting the plasma density profile using a femtosecond laser pulse.

5.5 Hydrodynamic Simulations

To investigate the mechanism for shock formation we employ numerical hydrodynamic simulations using the radiation hydrodynamics code HYDRA [133]. Complete simulation details are discussed in Section C.6. In brief, we simulate the interaction of two time-delayed laser pulses (each with an intensity of 4.9×10^{14} W/cm² with a 100 nm diameter nanoparticle composed of NaCl. A prominent shock wave is observed for time delays between 5 and 35 ps (Figures 5.5 and C.5). In addition, the hydrodynamic simulations accurately reproduce measured ion kinetic energies. The good agreement between simulated and observed ion energies indicates that the hydrodynamic calculations capture the physics of the plasma expansion.

The hydrodynamic calculations suggest a simple mechanism for shock formation (Figure 5.5). After the first pulse expands the cluster, the second laser pulse is absorbed in a relatively thin shell at the critical density (Figure 5.5a). The resultant heating produces a localized pressure increase that drives material away from the absorption region (Figure 5.5b). This shock wave reflects from the center of the plasma, resulting in a population of high-velocity ions at small radius (Figure 5.5b). These ions drive an outward-moving shock (Figure 5.5c), and the associated density increase produces a peak in the ion kinetic energy distribution (Figure 5.5d). The energy of the shock is determined both by the energy imparted by the laser and the work required for the high-velocity ions to accelerate the material ahead of them as they move to large radius. Similar to previous theoretical predictions [40, 42, 134] of shock formation in the Coulomb explosion of small clusters, the shock formation occurs when faster particles towards the interior of the plasma overrun slower

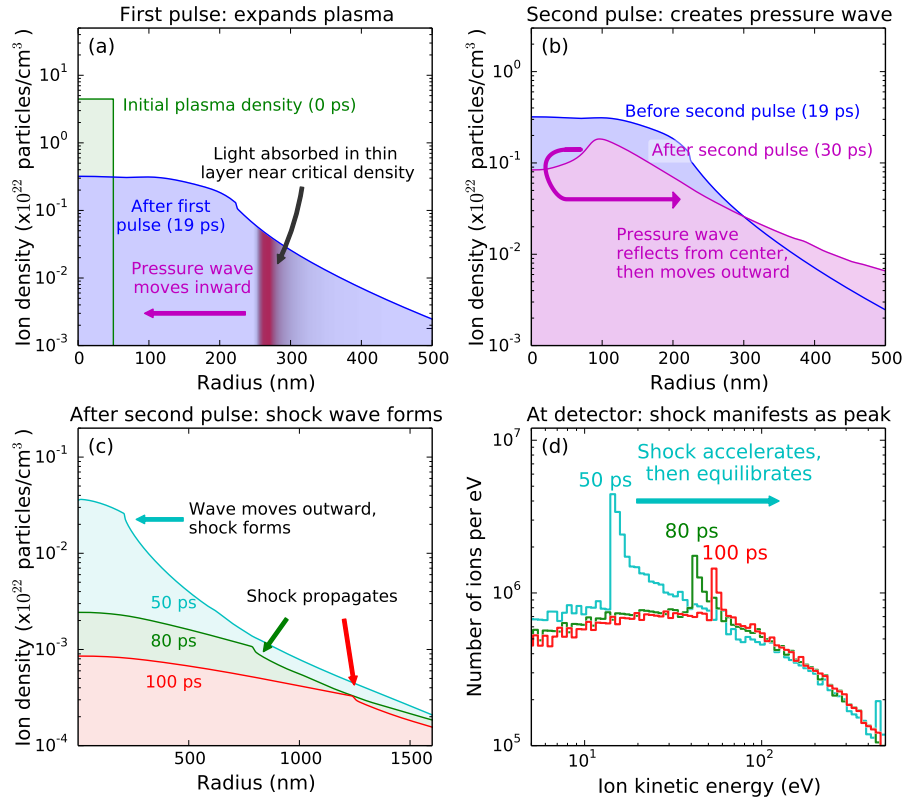


Figure 5.5: **The mechanism for two-pulse shock wave formation, as revealed by numerical hydrodynamics simulations using HYDRA [133].** (a) The first laser pulse creates a plasma, which expands into the surrounding vacuum. A small single-pulse shock wave can be seen near 230 nm. Near 270 nm, energy from the second laser pulse is preferentially absorbed (red shaded region) in a layer just below the critical density ($n_c = 1.7 \times 10^{21} \text{ cm}^{-3}$ at 800 nm). (b) The heating from the second laser pulse creates a pressure wave that moves inwards, reflects from the center, and then moves outwards. (c) The pressure wave moves outwards supersonically and accelerates slower material in front of it, creating a shock wave, which is seen as a small step in the ion density distribution. (d) In the kinetic energy distribution of the ions, the shock wave is a sharp peak which is accelerated by the pressure gradient, eventually settling at a final kinetic energy of a few 10s of eV after ~ 100 ps. It is this asymptotic kinetic energy distribution that is recorded by the spectrometer in the experiment. In this simulation, both laser pulses are modeled as 50 fs, 800 nm pulses with intensities of $4.9 \times 10^{14} \text{ W/cm}^2$. Adapted with permission from Ref. 4. ©2014 American Physical Society

particles in the exterior of the cluster. However, in this case, the velocity differential is caused by the preferential absorption of light near the critical density, which creates a ridge of high pressure. In contrast to studies conducted in the Coulomb explosion regime, where the shock is formed on the timescale of 100 fs, the shocks in these hydrodynamic explosions take ~ 50 ps to form.

Interestingly, the hydrodynamic simulations show a shock wave that accelerates as it moves

outwards (Figure 5.5c), which is most easily seen by the temporal increase in energy of the peak in the ion distribution (Figure 5.5d). In the simulations, the shock velocity increases by more than twofold during this acceleration period. The mechanism for such shock acceleration is well known, and stems from the radially decreasing density profile in the background plasma. In the classic Sedov-Taylor-Waxman-Shvarts [135] analysis of the problem, acceleration is seen for steep density gradients. Simple dimensional analysis scaling laws [136], which describe the asymptotic behavior of the shock, are in good agreement with the simulated shock acceleration once we account for the fact that our plasma density is rapidly decreasing with time. Accelerating shock waves are of great interest in astrophysics and, consequently, experiments have been proposed to investigate such shocks in the laboratory setting [137]. We believe that this study is the first realization of such an experiment and could serve as a versatile platform for studying shocks propagating through customizable density gradients.

5.6 Conclusion

Here we presented the first measurements of individual nanoplasmas, demonstrating a new method for studying laser-plasma interactions, which can be implemented using a tabletop apparatus and at a high repetition rate. By characterizing the momentum distribution of individual nanoplasmas, we make the first observation of plasma shock waves on the nanometer scale, confirming a decade of theoretical predictions [40, 42, 134]. By adjusting the time delay between two laser pulses, the creation and strength of the shock wave was varied in a controllable manner. Furthermore, because these shocks are produced in plasmas with temperatures of just ~ 10 eV, this experiment potentially enables a compact, inexpensive method for studying a relatively unexplored regime of low-temperature nanoplasmas.

Chapter 6

Conclusion and outlook

Science is what we understand well enough to explain to a computer.
Art is everything else we do. –Donald Knuth

6.1 Overview

This section summarizes the work presented in this thesis, provides an outlook for future work that can expand on the presented results, and provides a brief summary of new research directions that will be pursued. First, Section 6.2 summarizes each of the three main experiments and provides ideas for future experiments that could expand upon each of these results. Section 6.3 provides a brief description of several new experiments that are in the process of being constructed and could serve as fruitful avenues for future research.

6.2 Outlook

6.2.1 Strong-field ionization of gas-phase atoms and molecules

Chapter 3 demonstrated how changing the wavelength of the driving laser can provide new insight, even when using a “classic” experimental technique. In the presented study, the mid-IR driving lasers provided a clear picture of electron dynamics in the continuum, in good analogy to the higher-energy HHG that is also enabled with mid-IR driving lasers. The discovery of new physics using mid-IR driving lasers in the VMI suggests that using a VMI to study the strong-field ionization process will continue to yield breakthroughs as long as the parameter space continues to

be expanded.

The most obvious extension of the study would be to increase the wavelength of the driving laser to greater than $2.0 \mu\text{m}$ and see if additional features appear in the photoelectron spectrum. While driving laser wavelengths up to $7 \mu\text{m}$ [85, 138] have been explored, many of these were completed with low laser intensities and with species exhibiting exceptionally low ionization potentials, such as metastable xenon species [85]. Neutral atoms have been probed using driving laser wavelengths up to $3.7 \mu\text{m}$ [86], but only one-dimensional photoelectron spectra have been collected. High-quality angle-resolved photoelectron images using driving laser wavelengths longer than $2.0 \mu\text{m}$ are still lacking. It is possible that in the near future, the high-repetition rate optical parametric chirped pulse amplifier (OPCPA) that is in development in a collaboration between the Kapteyn–Murnane Group and KMLabs will provide sufficient pulse energies for strong-field ionization at $3.0 \mu\text{m}$ [139].

In addition to simply changing the wavelength of the driving laser, the polarization can also be changed to provide insight into different physics. Recently, the generation of circularly polarized XUV light from the HHG process has been accomplished through the mixing of counter-rotating circularly polarized 400 nm and 800 nm laser fields [140–142], thus demonstrating the importance of unusual polarization states of the driving laser for the HHG process. The laser field that results from the mixing of the circularly polarized 400 nm and 800 nm light (Figure 6.1) drives electrons two-dimensional trajectories [140, 143, 144], which opens the exciting possibility that the angle of electron tunneling and the angle of electron rescattering/recombination may be separated, allowing for the extraction of molecular structure using either HHG or SFI. Indeed, in a forthcoming publication [6], we demonstrate that two-color circularly polarized fields can enable electron rescattering when the fields are counter-rotating, but not when the fields are co-rotating.

In addition, more careful collection, analysis, and interpretation of PADs resulting from the strong-field ionization using previously explored wavelengths can continue to yield insight. For example, while Chapter 3 discusses the low energy structure (LES), more recent studies have identified two additional structures: the very low energy structure (VLES) and the zero energy structure (ZES, which is not actually at zero kinetic energy) and attributed them to more complicated processes in-

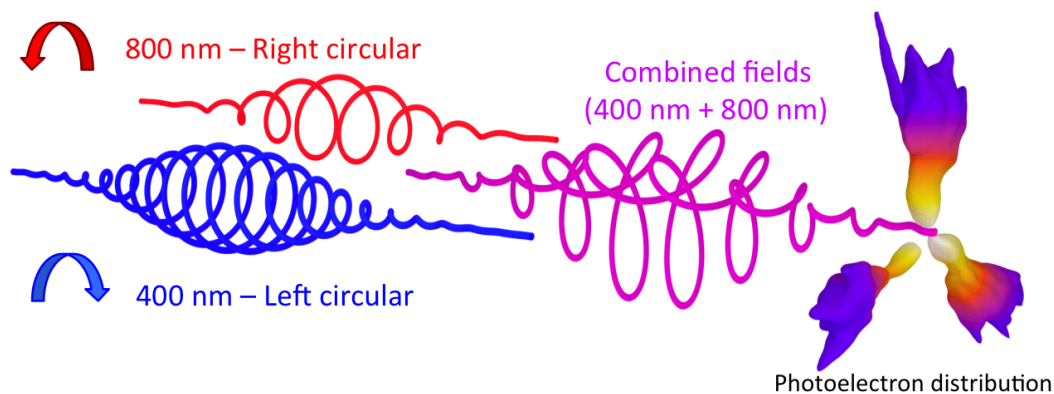


Figure 6.1: **Photoelectrons from circularly polarized driving lasers.** When counter-rotating circularly polarized 400 nm and 800 nm laser fields are mixed, the resulting field takes on a three-leaf clover shape, exhibiting three-fold symmetry. The 3D PAD can be reconstructed by rotating the PAD in the lab frame and collecting 2D projections at different angles.

volving the motion of electrons under the influence of the Coulomb potential of the ion [145–147]. Also, new analysis techniques have revealed that molecular structure information can be extracted even from one-dimensional photoelectron spectra using mid-IR driving lasers [29]. Exciting developments such as these demonstrate that the field of strong field ionization is far from being completely understood and will likely produce exciting insights for many years to come.

6.2.2 Plasma Explosion Imaging

Chapter 4 discusses the development of the Plasma Explosion Imaging (PEI) technique and applies it to four representative nanostructures. The obvious follow-up experiment would be to apply the PEI method to many more nanostructures and see how the results change. Additionally, the experiments could be completed in a time-resolved fashion, where a pump pulse is used to create a change in the geometry of optical properties of the material. This technique could potentially evaluate the evolution of the linear and nonlinear optical properties of the material on the femtosecond timescale.

6.2.3 Shock waves

The primary question posed by the study of shock waves in nanoplasmas presented in Chapter 5 is how the physics would scale with the laser intensity, and if higher intensity lasers could be used to generate very high energy ions, as was seen with smaller nanoplasmas [38] and proposed theoretically [41, 42]. While the laser intensity can easily be increased, the difficulty is that our VMI cannot observe electrons past ~ 100 eV and even the “highest energy” VMI cannot work past 330 eV [148]. Thus, studies that attempt to observe higher energy shock waves from nanoplasmas will need to use other techniques such as time-of-flight. However, time-of-flight provides a different mapping of kinetic energy and ion mass, and it might make the shock wave more difficult to observe.

An alternative method for understanding all manners of phenomena is to probe the plasma with high-energy photons. While visible and even ultraviolet light is generally not high-energy enough to penetrate into a dense plasma, EUV and X-ray photons are above the plasma frequency and can penetrate into a nanoplasmas. A 2014 theory paper by Peltz and coworkers [149] indicates that time-resolved X-ray scattering experiments will provide new insight into nanoplasmas.

Another important question for determining if nanoplasma shock waves will be a practical source of electrons, ions, and photons is if the shock wave can be made directional. In Chapter 5, the shocks are largely spherically symmetric, ejecting ions in all directions. However, some asymmetry is still seen in the directionality of the shock wave, suggesting that it may be possible to control the direction of high-energy ion ejection by controlling the characteristics of the particle from which the plasma is formed. It is possible that the principles that control the directional ion ejection in PEI will carry over to the shock-wave formation regime. For example, it may be possible to use specially shaped micro or nanoscale structures to ensure that a shock wave primarily ejects ions in a specific direction.

6.3 Future Directions

In the following sections I provide an outline of a few of the future experiments that are planned for the VMI spectrometer and the nanoparticle aerosol source.

6.3.1 Extreme ultraviolet probe of nanomaterials

When the idea to study nanoparticles using a VMI at JILA was first conceived, the goal was to attempt to image the exciton orbitals of quantum dots (QDs). These orbitals are called the 1S, 1P, etc. orbitals and there is an open question of what symmetry the photoelectron distribution will have when ionizing from these states. In Ref. 5, we used 400 nm light to excite a 1S exciton in CdSe QDs and 267 nm light to liberate the excited electron. However, in these experiments there was an overwhelming amount of secondary electrons and these obscured the primary photoelectrons, which were also at low kinetic energies. The same problem is encountered in photoemission from surfaces and the solution is to move to higher photon energy light sources, in the EUV. The EUV light does not cut down on secondary electron emission, but it does move the primary electrons to much higher kinetic energies so that they may be distinguished from the secondary electrons. Thus, with the hope of providing a clear picture of the exciton orbitals in quantum dots, we are now using EUV light from HHG as a probe for the photoelectron spectroscopy experiment.

Moving to a HHG source has several disadvantages – the primary one being the low flux – but offers several important advantages that may lead to breakthrough results. First, as mentioned above, XUV light is extremely surface sensitive, since electrons that are excited below the surface will likely scatter and not emerge as primary electrons. This is a curse and a blessing, because it dramatically decreases the photoelectron yield compared to lower photon energies, but it allows us to study processes on surfaces. Most importantly, the light generated using the HHG process constitutes some of the shortest laser pulses ever generated. Generating isolated attosecond pulses typically requires mid-IR driving lasers [32], but at driving laser wavelengths in the visible and near-IR, the attosecond pulse trains are locked to the phase of the driving laser. Due to this phenomena,

sub-femtosecond processes can be studied even when the overall duration of the pulse train is many femtoseconds.

6.3.2 Magnetron sputtering nanoparticle source

As mentioned in Section 2.4.1, The atomizer generates nanoparticles that have a layer of contamination dictated by the purity of the solvent. Even for the most pure solvents available, the nanoparticles are still covered by many atomic layers of contamination at a minimum. Since the EUV light is a surface sensitive probe, it is not meaningful to study atomizer-generated nanoparticles using EUV light. Consequently, we are exploring alternative methods of introducing isolated nanoparticles into the spectrometer. One possible method would be electrospray ionization, where a high voltage is used to atomize a liquid solution of nanoparticles into the vacuum. While electrospray has been highly successful at obtaining high-purity molecules and nanoparticles into a vacuum, the particles are charged, preventing the study of neutral nanoparticles.

Currently, the most promising method for introducing a stream of high-purity nanoparticles in the VMI spectrometer appears to be a Haberland-type [150, 151] magnetron-sputtering nanoparticle source (Figure 6.2). This device utilizes a traditional DC magnetron sputtering target, which produces free atoms from bulk material using a magnetically confined plasma. While a typical magnetron sputtering source produces the atoms directly into a high-vacuum chamber where they are used to produce thin-film coatings, a Haberland-type nanoparticle source places the magnetron source in a chamber with ~ 1 Torr argon gas, which extends for a few inches before incorporating an orifice into a high-vacuum chamber. As the atomic vapor traverses the argon-filled chamber, the atoms aggregate into nanoparticles and the size of the nanoparticles depends on the pressure of gas in the chamber and the length of the interaction region. After exiting into the high vacuum chamber, the aggregation stops and a freely expanding source of ultra-pure nanoparticles is achieved in high-vacuum conditions. Some of the nanoparticles are charged, but a significant fraction are neutral.

The magnetron sputtering source offers several additional advantages in addition to the purity of

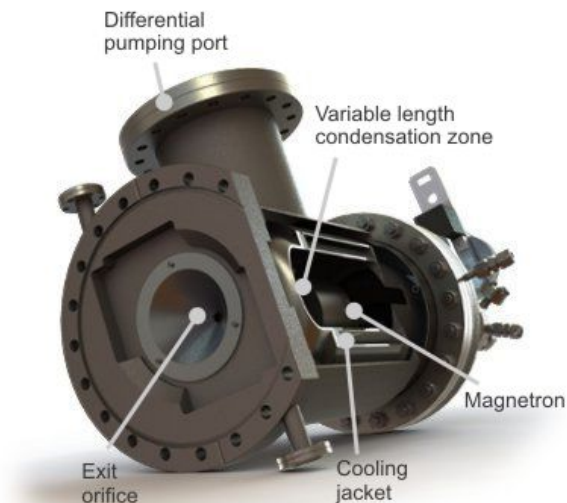


Figure 6.2: **Schematic of the NanoGen50.** The device uses the DC magnetron sputtering technique to transform a pure solid target (semiconductor or metal) into an atomic vapor. As the atoms pass through the condensation zone, they aggregate into nanoparticles, which then pass through the exit orifice and into the VMI spectrometer. ©2014 Mantis Deposition, used with permission.

the nanoparticles. It offers smaller nanoparticles, higher nanoparticle concentrations, better stability, and automated control over the particle size and parameters. Regarding the smaller size of the nanoparticles, the magnetron sputtering nanoparticle source can generate particles with diameters ranging from 2 to 20 nm, in contrast to the atomizer that has difficulty producing nanoparticles below 100 nm without serious contamination issues. The 2 to 20 nm size regime is much more interesting than the 100s of nm size regime because it is in the sizes of a few nm where most materials transition from atomic or cluster-like behavior to bulk behavior. Indeed, most QDs have sizes that are between 2 and 10 nm.

The concentration of the nanoparticle beam is also higher for the magnetron sputtering source, with the caveat that the source is divergent and therefore the particle concentration depends on the distance between the source and the interaction region. We estimate that the particle concentration at the exit of a commercial magnetron sputtering nanoparticle source (NanoGen50, Mantis Deposition, Figure 6.2) is approximately 10^9 particles/cm³ and that the device can be arranged to bring

10^7 particles/cm³ to the interaction region of the VMI spectrometer. It may be possible to couple the magnetron sputtering nanoparticle source to an aerodynamic lens and generate a collimated nanoparticle beam, thereby increasing the particle concentration in the interaction region. However, an aerodynamic lens that is specially designed for the smaller particles generated by the magnetron sputtering source would be required.

6.4 Conclusion

This thesis described how velocity map imaging photoelectron and photoion spectroscopy can be extended to study a wide variety of phenomena, including strong-field electron dynamics in atoms, local field enhancement in single, isolated nanoparticles, and shock wave propagation in nanoplasmas. Specifically, several important developments were highlighted, including

- The first observation of the “inner spider” structures in strong-field ionization. (Chapter 3).
- The development of an intuitive model (the plane-spherical wave model) that can explain the most prominent interference structures observed in the strong-field ionization of atoms and molecules (Chapter 3).
- The realization that a VMI spectrometer can be used to probe individual nanoparticles at a high repetition rate (Chapters 4 and 5).
- The invention of a new technique for observing the local-field enhancement in nanostructures called plasma explosion imaging (Chapter 4).
- The first observation of shock waves in nanoscale plasmas, a discovery that confirmed a decade of theoretical work (Chapter 5).
- The presentation of a clear path towards the experimental observation of attosecond dynamics in isolated, ultrapure metal and semiconductor nanocrystals (Chapter 6).

These results presented in this thesis answered many questions (for instance, they explained the origin of the famous “low energy structure” [86] and confirmed the 2003 prediction of shock

waves in nanoplasmas [40]) but they posed more questions, including the feasibility of utilizing the nanoplasma shock waves to accelerate high-energy ions, the applicability of the PEI technique to other laser-intensity regimes, and the scaling of the inner-spider structures with longer wavelength driving lasers. Future studies at JILA will extend these new techniques to utilize HHG as an XUV light source and use small, ultra-pure nanoparticles generated in vacuum to make the measurements of electron dynamics in nanoparticles on the attosecond timescale.

Appendix A

Multiple Scattering Structures Appendix

This chapter is adapted, with permission, from the Supplemental Material for:

- D. D. Hickstein, P. Ranitovic, S. Witte, X.-M. Tong, Y. Huismans, P. Arpin, X. Zhou, K. E. Keister, C. Hogle, B. Zhang, C. Ding, P. Johnsson, N. Toshima, M. J. J. Vrakking, M. M. Murnane, and H. C. Kapteyn. Direct Visualization of Laser-Driven Electron Multiple Scattering and Tunneling Distance in Strong-Field Ionization. *Phys. Rev. Lett.*, 109, **2012**, 073004. DOI: 10.1103/PhysRevLett.109.073004
©2012 American Physical Society

A.1 Overview

This appendix provides additional details about the multiple scattering structures described in Chapter 3 that result from the strong-field ionization of noble gases with strong femtosecond laser pulses in the mid-IR region. Section A.2 describes the implementation of the PSW model, Section A.3 explains the analysis of the classical trajectories that is used to calculate the modulation frequency of the plane and spherical waves, Section A.4 elaborates on the method used to extract the multiple rescattering cutoffs from the experimental data, and Section A.5 discusses the dependence of the TDSE results on the laser intensity.

A.2 Details of the Plane-Spherical Wave Model

In the plane-spherical wave model, we aim to reproduce the angle and spacing of the spider structures from first principles using a simple superposition of two waves. We represent the part of

the electron wavepacket that does not scatter from the ion as an elliptical Gaussian wavepacket with plane phase (Ψ_{plane}), while the part of the wavepacket that does scatter from the ion is represented as an elliptical Gaussian wavepacket with spherical phase ($\Psi_{\text{spherical}}$). We call these elliptical Gaussian wavepackets the “plane wave” and the “spherical wave” respectively. The plane and spherical waves are written as

$$\Psi_{\text{plane}} = A_{\text{plane}} \exp \left[- \left(\frac{P_{\perp}^2}{2\sigma_{\perp}^2} + \frac{P_{\parallel}^2}{2\sigma_{\parallel}^2} \right) \right] e^{iP_{\parallel} \cdot f}, \quad (\text{A.1})$$

$$\Psi_{\text{spherical}} = A_{\text{spherical}} \exp \left[- \left(\frac{P_{\perp}^2}{2\sigma_{\perp}^2} + \frac{P_{\parallel}^2}{2\sigma_{\parallel}^2} \right) \right] e^{iP_{\text{total}} \cdot f}, \quad (\text{A.2})$$

where A_{plane} and $A_{\text{spherical}}$ are the amplitude of the plane and spherical waves, P_{\perp} and P_{\parallel} are the components of the final momentum perpendicular to and parallel to the laser polarization, P_{total} is the total final momentum and is equal to $\sqrt{P_{\perp}^2 + P_{\parallel}^2}$, σ_{\perp} and σ_{\parallel} determine the width of the wavepacket in the P_{\perp} and P_{\parallel} directions, and f is the modulation frequency of the plane and spherical waves.

The frequency f is not the same as the spacing of the spider structures, but the shape (and frequency) of the spider structures is a function of f . Since we are only concerned with reproducing the interference pattern, σ_{\perp} and σ_{\parallel} are set empirically, to match the width and height of the experimental photoelectron distribution. The observed photoelectron interference pattern is given as the superposition of Ψ_{plane} and $\Psi_{\text{spherical}}$ as

$$\Psi_{\text{total}} = \Psi_{\text{plane}} + \Psi_{\text{spherical}}, \quad (\text{A.3})$$

where both wavefunction are complex.

The above superposition produces interference patterns that look quite similar to the spider structures seen in the experimental photoelectron spectra as well as the TDSE calculations. The only parameters used are the amplitudes of the plane and spherical waves (A_{plane} and $A_{\text{spherical}}$) and the width and height of the wavepackets (σ_{\perp} and σ_{\parallel}), but these only control the overall shape of the generated electron distribution and do not affect the shape or frequency of the spider structures. The modulation frequency waves (f) is determined through a quasi-classical analysis of the electron trajectories. To observe the spider structure interference, f must be the same for the plane wave

and the spherical wave. If f is different for the plane wave and spherical wave, qualitatively different interference patterns are observed.

A.3 Calculating the modulation frequency

In a path-integral approach, we can understand the interference of particles by examining the various trajectories by which a particle can reach a certain point and summing those trajectories coherently (Figure A.1). The amplitude of each trajectory is equal, but the phase of each trajectory is given by $e^{(iS/\hbar)}$, where S is the action given by Equation 3.1. Thus, we can re-create the complete photoelectron angular distribution by integrating all of the trajectories that can reach each point in the final momentum space. Indeed, this is the approach employed in the CCSFA model presented by Huismans and coworkers [85].

In the long-wavelength limit (where the electron wave packet enjoys a long sojourn in the continuum and spreads significantly), only electrons that tunnel with very low transverse momentum return close enough to the ion to be significantly affected by the Coulomb potential. Thus, we make the approximation that the rescattered electrons have zero transverse momentum until they scatter from the Coulomb potential. We also assume that the scattering will be elastic and can occur in any direction with equal probability.

To calculate the action from Equation 3.1, it at first seems necessary to integrate each trajectory from the time that an electron tunnels into the continuum to the time that the electron reaches the detector. However, the situation simplifies because any two electrons that have the same vector momentum at the same point in time will accumulate the same action from that point onward. Once the rescattered trajectory scatters from the Coulomb potential, it now has the same momentum as the corresponding revisiting trajectory and we may stop integrating Equation 3.1. By integrating Equation 3.1 for both the revisiting and rescattered trajectories from the time that the electrons tunnel to the time that the rescattering trajectory reaches the ion and rescatters, Huismans [85] and Bian [152] were able to reproduce the spider structure using this generalized SFA model.

Here we further simplify the generalized SFA model by treating the revisiting electrons as a

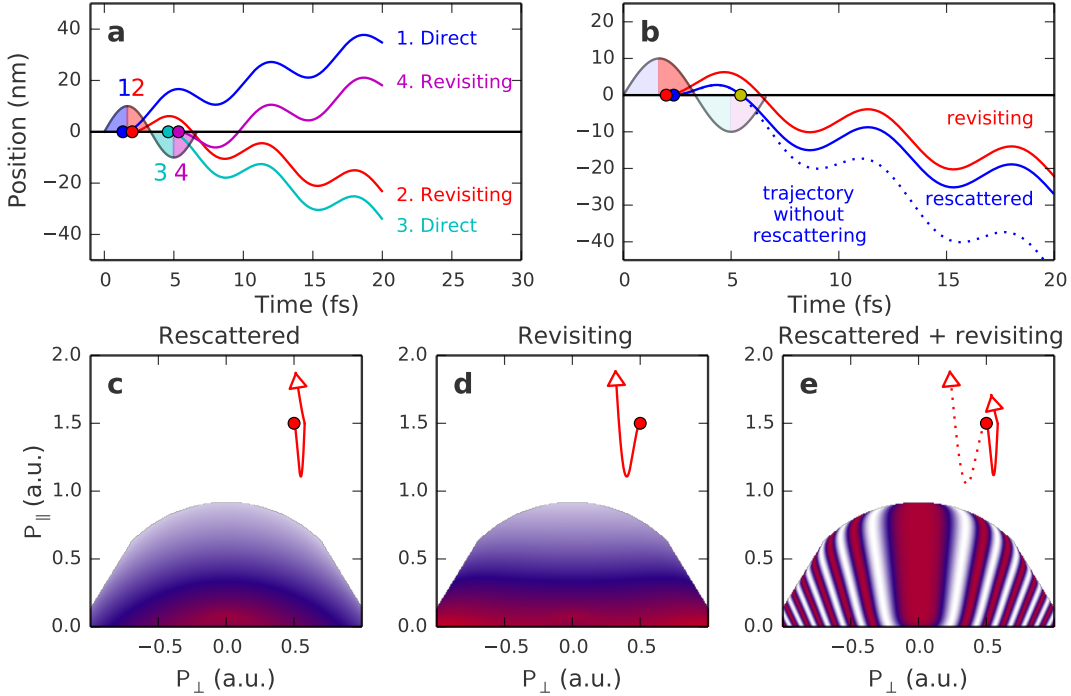


Figure A.1: **Electron trajectories that produce photoelectron interference structures.** (a) Electrons from the 1st and 3rd quarter cycles are driven away from the ion, never to return. Electrons from the 2nd and 4th quarter cycles are first driven away from and then back to the vicinity of the ion. (b) The spider structures result from interferences between trajectories that pass the ion without rescattering and trajectories that pass the ion closely and are scattered by the Coulomb potential. (c) Phase of the rescattered trajectories calculated by integrating Equation 3.1 between tunneling and rescattering events. (d) Phase of the revisiting trajectories calculated by integrating Equation 3.1 between tunneling and rescattering event - the phase accumulated is linear with the longitudinal momentum. (e) Interferences between the rescattering and revisiting trajectories creates the spider structures. (insets in panels c,d,e) Sketches of the 2D trajectories corresponding to the rescattered and revisiting trajectories. Adapted with permission from Ref. 2. ©2012 American Physical Society

simple plane wave in the final momentum space and treating the rescattered electrons as a spherical wave in the final momentum space. The modulation frequency of each wave is related to the action accumulated according to Equation 3.1, as discussed below. Although we are dealing with a scattering problem, this plane-spherical wave approximation is not obvious since we are making the approximation in the final-momentum space as opposed to real space. Initially, it is not clear why the revisiting electrons should resemble a plane wave on the detector and why the rescattered electrons can be treated as a spherical wave. However, after completing a generalized SFA analysis of

the interference patterns (Figure A.1e) and examining the revisiting (Figure A.1d) and rescattered (Figure A.1c) contributions separately, we see that they do indeed resemble a plane wave and a spherical wave. The wavefront curvature that might be expected in the wavefunction for the revisiting electrons has been compensated since the electrons are turned around by the laser field.

To calculate the modulation frequency (f) needed for the plane-spherical wave model, we simply calculate the action (using Equation 3.1) for a range of trajectories that correspond to P_{\parallel} from 0 to $2U_P$. By assuming that trajectories that can rescatter on a subsequent revisit will scatter on the second, fourth, sixth, etc. revisit, we stop integrating Equation 3.1 at different times and obtain the plot shown in Figure 3.5b. Thus, the procedure for creating a complete PSW calculation consists of three steps. First, a series of classical trajectories corresponding to a range of P_{\parallel} are flown and the action is calculated along each one from the time that the electron tunnels into the continuum to the time that the electron returns to the ion. Next, we make a plot of the action versus the final momentum and fit a line to the nearly-linear curve. The slope of this line is the modulation frequency (f) needed for the plane-spherical wave model. Finally, we use Equation A.3 to create the 2D photoelectron momentum distribution, estimating the amplitude and shape of the Gaussian wave packet to best fit the experimental data.

A.4 Extracting the experimental multiple rescattering cutoff

In order to estimate the quantum-mechanical tunneling distance, we measured the position of the multiple rescattering cutoff across a broad range of laser wavelengths and intensities. Though it is reasonably easy to visually estimate the cutoff of the inner spider structures in the 2D photoelectron spectra, a more quantitative definition is desirable to ensure sufficient precision. We identified the cutoff of the inner spider structures by looking closely at the inner spider structure closest to $P_{\parallel} = 0$. That is, we looked at the first set of “spider legs” closest to the central maxima.

Since the colormap and contrast of the 2D image can cause influence the appearance of the 2D photoelectron angular distribution, we took 1D lineouts across the 2D spectra at various values of P_{\perp} (Figure A.2). When the lineout is taken across the inner spider structure, additional maxima and

minima are seen that correspond to the inner spider fringes. The cutoff of the inner spider structure was defined as the value of P_{\perp} where these maxima and minima can no longer be identified. In Figure A.2b, the red line is above the cutoff and the green line is below. Using this method, we can identify the cutoff to the nearest 5 pixels (0.018 atomic units of momentum). For displaying the error range in Figures A.3 and 3.6b, we set the error equal to 0.02 atomic units of momentum. The relative intensity of the experimental photoelectron distributions was measured using a power meter and the absolute intensity was calibrated from the $2U_p$ cutoffs and comparison with the TDSE results (Figure 3.4).

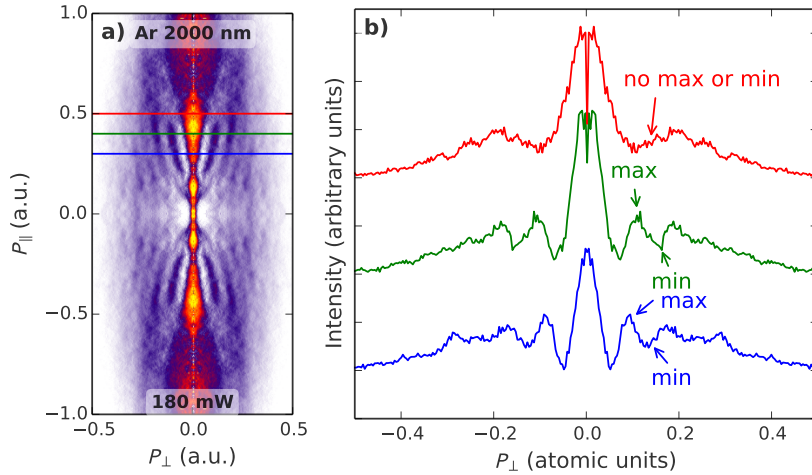


Figure A.2: **The procedure for determining the cutoff of the inner spider structures in the experimental 2D photoelectron momentum distributions.** a) For this PAD, the inner spider structure extends from about $P_{\parallel} = 0.25$ to 0.45 atomic units. The colored lines correspond to the lineouts shown on the right. The lineouts are integrated over 3 pixels (0.01 atomic units of momentum) of P_{\perp} to reduce noise. We are only concerned with the inner spider legs that appear closest to $P_{\parallel} = 0$. Adapted with permission from Ref. 2. ©2012 American Physical Society

A.5 Intensity dependence

The TDSE calculation presented in Figure 3.5e was not averaged over the focal volume of the laser. Fortunately, focal-volume averaging does not dramatically affect the appearance of the main spider structures or the inner spider structures for two reasons. First, as shown in Figure A.4d, the yield from calculations performed at $5.5 \times 10^{13} \text{ W/cm}^2$ is an order of magnitude larger than the yield

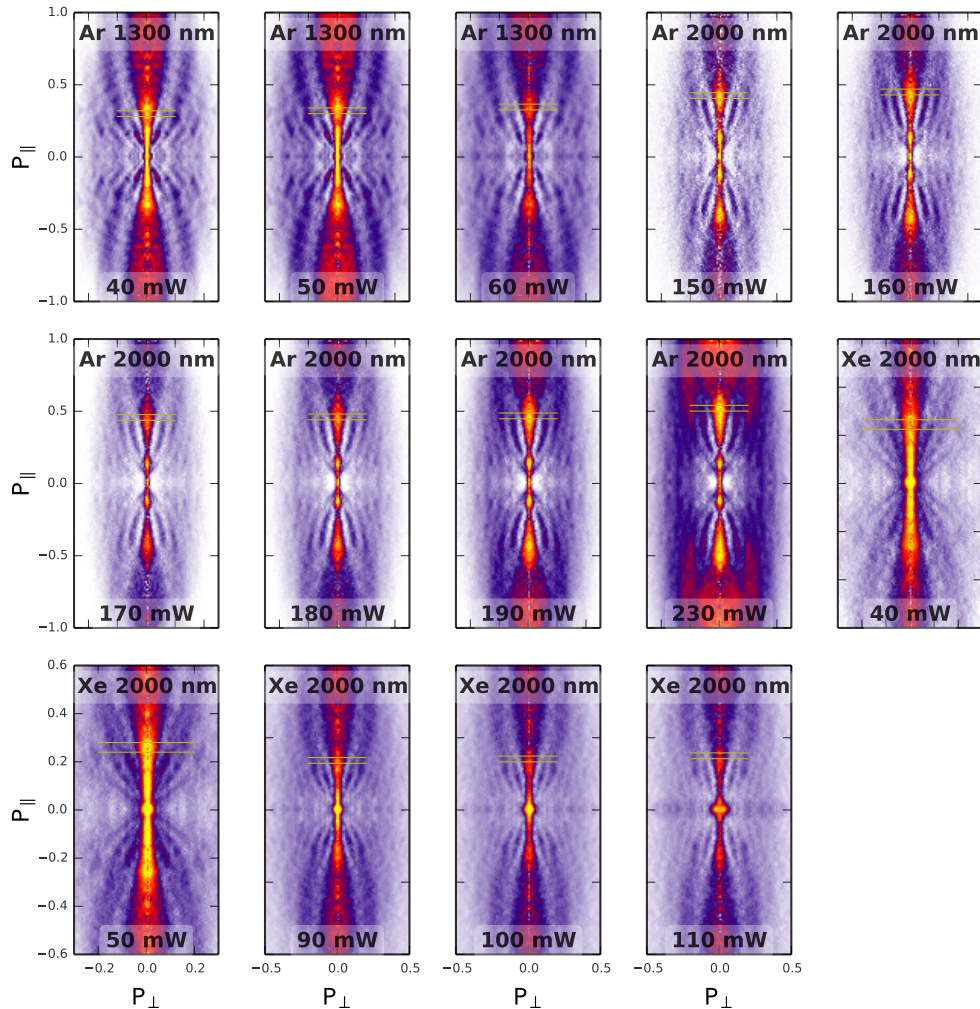


Figure A.3: **The positions of the inner-spider cutoffs.** The high P_{\parallel} cutoff of the inner spider structures was found using the 1D inspection method shown in Figure A.2 and the error was set to be ± 0.02 atomic units of momentum. The upper and lower error-boundaries are shown with yellow lines on the 2D photoelectron momentum distributions shown above. The position of the inner spider cutoff found using the 1D corresponds to the apparent position of the cutoffs in the 2D spectra. The upper and lower bounds (yellow lines) correspond to the upper and lower limits indicated with error bars in Figure 3.6b. Adapted with permission from Ref. 2. ©2012 American Physical Society

from $4.5 \times 10^{13} \text{ W/cm}^2$. This large difference is due to the highly non-linear nature of the strong-field ionization process as well as the fact that the calculations and experiments were performed well below ionization saturation. Additionally, Figures 3.6a–c show that the spider structures do not significantly change shape or angle with a reasonable change in intensity. The inner spider structure

can be clearly seen to extend to higher kinetic energy at higher laser intensity, but the shape of the structure at low energy remains the same. Thus, both the primary and inner spider structures are robust to the focal volume averaging that takes place in the experiment.

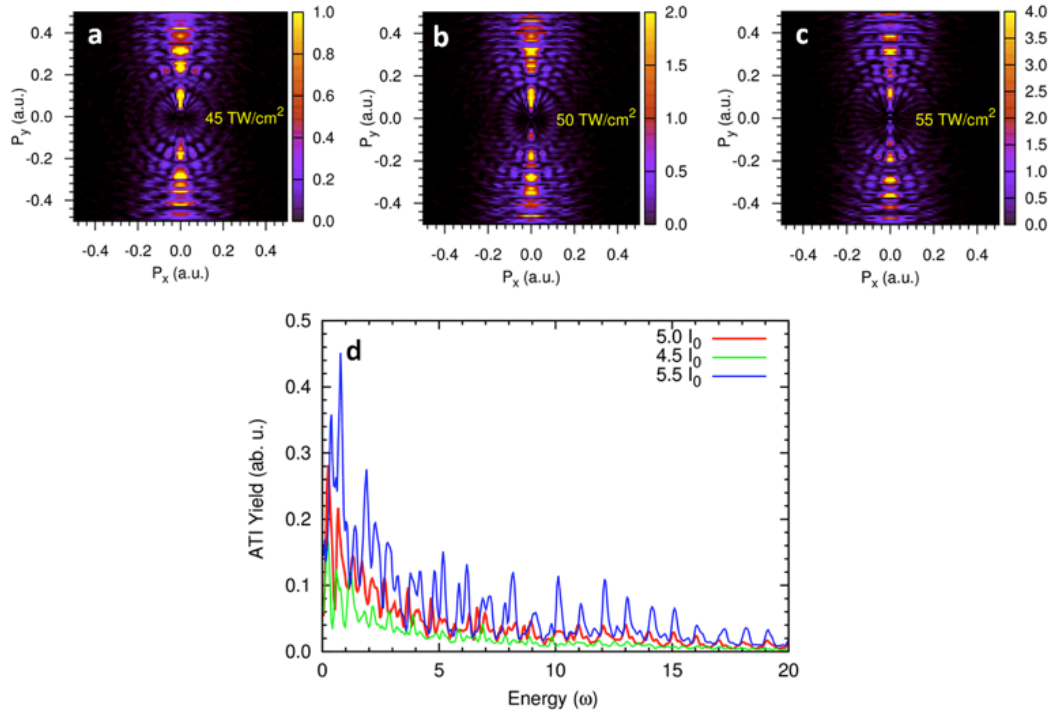


Figure A.4: **Dependence of the inner spider structures on the intensity of the driving laser.** (a-c) The photoelectron angular distributions calculated using TDSE for xenon using a 2000 nm driving laser at various laser intensities. The color scales have been adjusted to show the spider structures. The spider structures extend to higher energies at higher laser intensity, but the shape of the spider structure does not change significantly with intensity. (d) The angle-integrated photoelectron yield plotted on the same scale reveals that the photoelectron yield quickly increases with intensity. Figure by Xiao-Min Tong, Tsukuba University. Adapted with permission from Ref. 2. ©2012 American Physical Society

Appendix B

Plasma Explosion Imaging Appendix

This chapter is adapted, with permission, from the Supporting Information for:

- D. D. Hickstein, F. Dollar, J. L. Ellis, K. J. Schnitzenbaumer, K. E. Keister, G. M. Petrov, C. Ding, B. B. Palm, J. A. Gaffney, M. E. Foord, S. B. Libby, G. Dukovic, J. L. Jimenez, H. C. Kapteyn, M. M. Murnane, and W. Xiong. Mapping Nanoscale Absorption of Femtosecond Laser Pulses using Plasma Explosion Imaging. *ACS Nano*, 8 (9), **2014**, 8810. DOI: 10.1021/nm503199v
©2014 American Chemical Society

B.1 Overview

This appendix provides additional details about the plasma explosion imaging (PEI) technique described in Chapter 4. Section B.2 provides details about the experimental methods, the nanoparticle samples, and the FDTD simulations. Section B.3 compares the photoelectron distributions to the photoion distributions from PEI in single nanoparticles, and Section B.4 describes single nanoparticle mass spectrometry experiments that confirm that the observed ions result from the nanoparticle itself and not from the background gas in the spectrometer chamber.

B.2 Methods

B.2.1 Photoion spectroscopy and aerosol generation

To perform velocity-map-imaging spectroscopy on nanostructures, we first generate a nanoparticle aerosol, consisting of isolated nanoparticles suspended in N₂ gas. The aerosol enters a low-

vacuum chamber through an aerodynamic lens (Aerodyne Research) [70, 111] that collimates the particles into a ~ 0.5 mm beam, but leaves the carrier gas divergent. The collimated particle beam passes through a 1.5 mm skimmer and enters the photoion spectroscopy chamber, which is maintained at 10^{-6} Torr (base pressure 10^{-8} Torr). The particles are then irradiated by an intense ($\sim 3 \times 10^{13}$ W/cm²), 785 nm, 40 fs laser pulse, derived from a Ti:sapphire regenerative amplifier (KMLabs Wyvern HE) operating at 1 kHz.

The laser is focused using a 40 cm lens to reach an approximate diameter of 20 μ m, which – considering the width of the particle beam (0.05 cm) – provides an interaction volume of approximately 10^{-7} cm³. Because the density of the nanoparticles is only $\sim 10^5$ particles/cm³, the hit rate is ~ 0.01 particles per laser shot. The photoions originating from the laser-irradiated nanoparticles are imaged by a velocity-map-imaging (VMI) spectrometer [51], which projects the expanding ion distribution onto an microchannel-plate–phosphor detector. The angular-resolved momentum distribution of the ions is then recorded using a CCD camera (Allied Vision Technologies) operating at ~ 15 Hz. The exposure time of the camera is adjusted to ensure that each frame consists of only one particle hit.

B.2.2 Materials

We obtained pure NaCl from Sigma Aldrich and ~ 5 nm TiO₂ nanoparticles from US Research Nanomaterials. The 50 and 17 nm gold nanospheres were obtained from Nanocomposix, Inc. All samples were used as received, except for dilution in ultrapure (>15 M Ω resistivity) water. The liquid samples are converted into an aerosol using a Collison-type compressed-gas atomizer (TSI) backed with 30 psig of N₂ carrier gas.

B.2.3 Transmission electron microscopy

To characterize the nanoparticles probed by the laser, we performed transmission electron microscopy (TEM) on particles collected in the high vacuum chamber. TEM grids were inserted into the chamber using a magnetically coupled linear actuator (Kurt J. Lesker, Inc.) passing through

an airlock. The TEM grids were positioned at the exact position where the laser crosses that particle beam, and high-velocity particles were collected on the grids for 10 to 30 seconds. TEM images were obtained using a Phillips CM100 Transmission Electron Microscope.

B.2.4 Finite-difference time-domain (FDTD) simulations

To understand the results obtained with photoion spectroscopy, we employed finite difference time domain (FDTD) simulations implemented in the FDTD Solutions [153] software package (Lumerical, Solutions Inc.) to simulate the interaction of the laser field with the nanoparticles. We simulated the interaction of a 40 fs pulses with a central wavelength of 785 nm with several different structures that are representative of the actual geometry of our nanoparticles. The TiO_2 particles were simulated as a collection of 6 layers of 5 nm dielectric spheres with $n = 2.523$ (the refractive index of TiO_2 at 785 nm [154]). The NaCl nanocrystals were simulated as 100 nm diameter dielectric spheres with $n = 1.536$ (the refractive index of NaCl [155] at 785 nm). The gold-PVP heterostructures were simulated as 50 or 17 nm gold spheres embedded in a dielectric sphere with $n = 1.4$ (the approximate index of PVP at near-IR wavelengths [156]). The wavelength-dependent complex refractive index of gold was treated according to the Palik [157] model.

B.3 Photoelectron Distributions

The above analysis focused only on the photoion angular distributions (Figure 4.5). However, the VMI spectrometer can easily collect photoelectron angular distributions simply by applying negative (instead of positive) potentials to the electrodes. Similar to the photoion distributions, the photoelectron distributions from individual nanoparticles are also frequently asymmetric about zero kinetic energy (Figure B.1), with similar directional preferences as the photoion distributions. In contrast, the photoelectron distributions exhibit a peak near zero kinetic energy, which is absent in the photoion distributions. In addition, the asymmetry is typically less pronounced in the photoelectron distributions than in the photoion distributions.

These two qualitative differences between the photoelectron and photoion distributions are

both explained by the large difference in mass between electrons and ions, which has two principal effects. First, because the electrons are significantly lighter than the ions, they undergo significantly more scattering in the expanding plasma and the angular ejection caused by the localized plasma formation is partially obscured. Second, the near-zero energy peak in the photoelectron distribution is a result of atoms left in excited states that are subsequently ionized by the electric field of the spectrometer. A recent study of nanoplasmas formed in xenon clusters with extreme ultraviolet radiation [158] has observed a similar low-energy peak and attributed it to electrons in high-lying atomic Rydberg states that are detached by the electric field on the spectrometer [159].

Initially, it might be assumed that an electric-field-induced separation of weakly bound electron-ion pairs would result in a field-ionized electron angular distribution that is an exact replica of the ion distribution. However, this is not the case due to the differences in masses between the electron and the ion. If we consider an electron-ion pair moving transverse to the detector with kinetic energy E_i , and assume that both the electron and ion will maintain the same transverse velocity when separated, then the energy of the electron is given by

$$E_e = \frac{m_e}{m_i} E_i \quad (\text{B.1})$$

where $\frac{m_e}{m_i}$ is the ratio of the masses of the electron and the ion. For example, if a gold ion is travelling at 80 eV (roughly the edge of the detection range of our VMI) then the field-ionized electron will have a kinetic energy of only 0.0002 eV. Thus, while the ions may have a wide range of kinetic energies, any field-ionized electrons will arrive as part of the low-energy peak.

Photoelectron spectra were not collected for the samples presented above, but photoion and photoelectron spectra were collected under identical conditions for a sample of ~ 25 nm gold nanoparticles prepared via the citrate synthesis as described by McFarland and coworkers [160]. The 25 nm gold nanoparticle sample exhibits directional ion ejection characteristics that are very similar to the 50 nm gold nanoparticle sample described in the manuscript. We infer that the excess sodium citrate from the nanoparticle synthesis is acting in a very similar fashion to the PVP in the case of the 50 nm gold nanoparticle sample. The laser intensity used for the photoelectron/photoion imaging

of the 25 nm gold nanoparticle sample (Figure B.1) is $\sim 3 \times 10^{13}$ W/cm², which is the same as used in Figure 4.5.

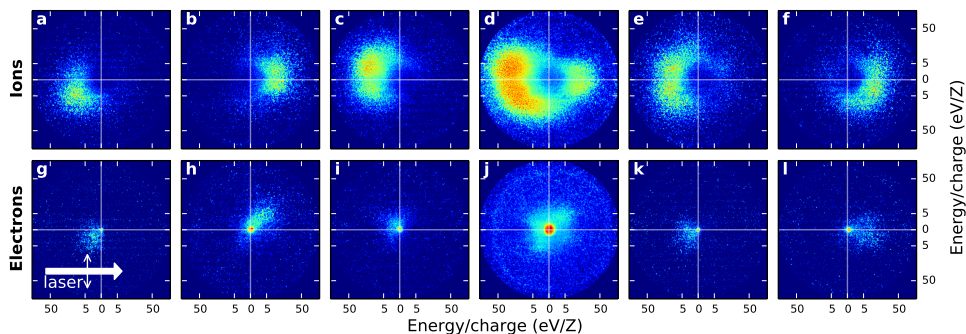


Figure B.1: **Comparison of photoelectron and photoion distributions from single nanoparticles.** Photoions (top) and photoelectrons (bottom) from a sample of 25 nm gold nanoparticles prepared via the citrate synthesis. The photoion and photoelectron distributions were collected separately and do not correspond to the same nanoparticle, but they are plotted next to one another to demonstrate the correspondence of the angular ion ejection. This gold nanoparticle sample behaves similarly to the 50 nm gold nanosphere sample discussed in the Chapter 4, ejecting electrons and ions at a specific, but random, angle due to the random orientation of each nanoparticle. The electrons exhibit the same qualitative behavior to the ions with respect to the angle of ion ejection. However, the electrons are ejected to lower kinetic energies, show somewhat less asymmetry in general, and feature a sharp peak near zero kinetic energy, differences that can be explained in terms of the significant mass difference between the electrons and the ions. Adapted with permission from Ref. 3. ©2014 American Chemical Society

B.4 Plasma Explosion Mass Spectrometry

B.4.1 Mass spectrum of a single nanoparticle

Above, we make the assumption that the ions reaching the detector correspond to atoms that were originally found in the nanoparticle. However, it is conceivable that the plasma formation process would eject numerous electrons that would, in turn, collide with background gas particles (N₂), creating additional ions. A representative mass spectrum corresponding to a nanoplasma formed in a single potassium iodide (KI) nanoparticle (Figure B.2) demonstrates that the majority of the ions observed on the detector correspond to the plasma formation process. The main ion species resulting from the ablation of the KI particles are K⁺, I⁺, C⁺, and H⁺. The predominance of K⁺ and I⁺ is due to the KI sample used in the experiment. The increased relative abundance of

K^+ compared to I^+ is a result of the higher ionization potential of I compared to K.

The observation of H^+ results from a thin film of water that adheres to the nanoparticle sample even after passing through a diffusion dryer and into the vacuum chamber. Indeed, the small, poorly resolved peaks around 16–18 Da may correspond to H_2O^+ (18 Da), OH^+ (17 Da), and O^+ (16 Da). The C^+ peak (12 Da) likely corresponds to the contamination of the sample with a small amount of methanol, which is used to clean the atomizer between samples. Indeed, there is a broad peak near 32 Da which could correspond to CH_3OH^+ .

Most importantly, we do not observe significant ionization of the background gas. The base pressure of the spectrometer chamber when the nanoparticle source is not in use is $\sim 10^{-8}$ Torr and increases to $\sim 10^{-6}$ Torr when the experiment is running, demonstrating that the majority of the background gas during the experiment comes from the nanoparticle source, which used N_2 as a carrier gas. The insignificant role of the background gas is evidenced by the lack of ions with masses corresponding to N^+ (14 Da) or N_2^+ (28 Da). Thus, the mass spectrum of a single KI nanoparticle demonstrates that the ions that reach the detector are due to the atoms in the nanoparticle itself, and not from the background gas.

B.4.2 Time-of-flight experimental details

The mass spectrum was collected using the same MCP-phosphor detector as for the VMI images, except that the voltage drop across the phosphor screen was monitored. Acquiring time-of-flight information on the ions is experimentally challenging, because each plasma explosion can eject more than 10,000 ions, which is far greater than typical mass spectrometry that generally detects just 1 ion per laser shot. Thus, instead of the time-to-digital converter typically used in mass spectrometry, we recorded the mass spectrum using a high-performance digitizer card (Acqiris U1084A, Agilent Technologies) that sampled the voltage drop across the detector at 0.5 ns intervals with 8-bit precision. Still, the data acquisition is complicated due to the low dynamic range of this single-shot sampling method and the severe ringing in the electronics due to the extremely high ion yield. Nevertheless, we are able to observe plasma explosions from single nanoparticles at the full

repetition rate of the laser (1 kHz). We observe many of the same trends seen in the VMI images. For example, there is a large range of photoion yields, which correspond to nanoparticles of different sizes and different intensities in the laser focus.

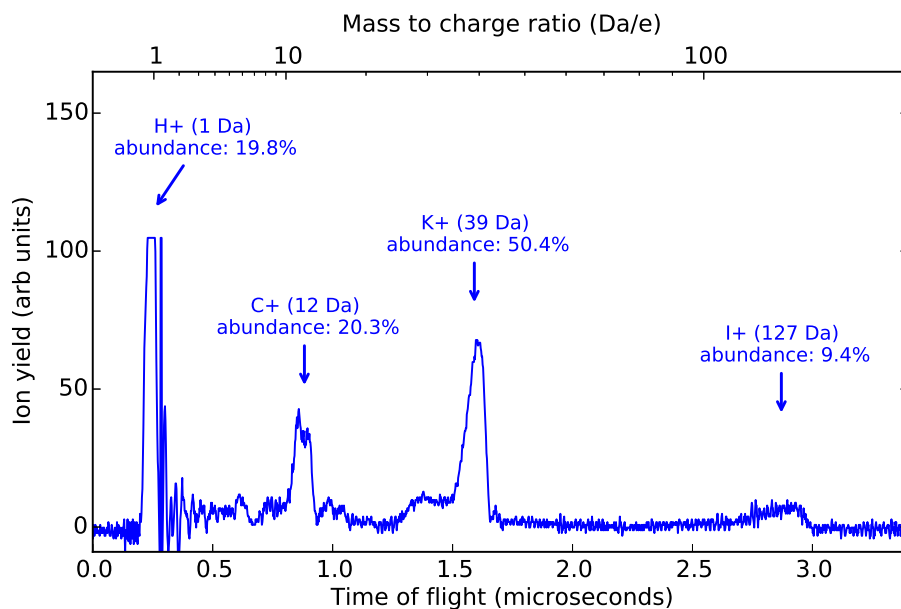


Figure B.2: **Mass spectrum of a single nanoparticle explosion.** The photoion mass spectrum corresponding to plasma formation in a single, representative potassium iodide (KI) nanoparticle demonstrates that the observed ions originate from the nanoparticle itself (K^+ and I^+) and not from the background gas (N_2). The H^+ and C^+ peaks likely correspond to a layer of water and methanol that forms on the surface of the particle. The prominence of the H^+ peak is over-emphasized by the severe electronic ringing that takes place due to the intensity of the ion signal. The relative abundance of each peak is expressed in terms of total identified ions; the labeled peaks account for more than 75% of all positive ions detected. Adapted with permission from Ref. 3. ©2014 American Chemical Society

Appendix C

Shock Waves in Nanoplasmas Appendix

This chapter is adapted, with permission, from the Supplemental Material for:

- D. D. Hickstein, F. Dollar, J. A. Gaffney, M. E. Foord, G. M. Petrov, B. B. Palm, K. E. Keister, J. L. Ellis, C. Ding, S. B. Libby, J. L. Jimenez, H. C. Kapteyn, M. M. Murnane, and W. Xiong. Observation and Control of Shock Waves in Individual Nanoplasmas. *Phys. Rev. Lett.*, 112 (11), **2014**, 115004. DOI: 10.1103/PhysRevLett.112.115004 ©2014 American Physical Society

C.1 Overview

This appendix provides additional details about the observation of nanoplasma shock waves described in Chapter 5. Section C.2 provides a description of the apparatus and techniques used to create and observe the shock waves. Section C.3 presents data showing that larger nanoparticles have a higher likelihood of producing shock waves. Section C.4 discusses the effect of the laser intensity on the total ion yield and the shock formation rate when using a single laser pulse. Section C.5 describes how the time delay between two laser pulses can be used to optimize the shock production rate. Section C.6 presents additional details about the HYDRA hydrodynamics simulations and discusses how the kinetic energy of the shock waves might increase at higher laser intensities. Section C.7 explains why the expansion larger nanoplasmas must be treated as a net-neutral hydrodynamic expansion in contrast to the expansion smaller nanoplasmas which can be understood as a Coulomb explosion.

C.2 Experimental Details

The experimental apparatus consists of a nanoparticle aerosol source coupled to a velocity-map-imaging (VMI) photoion spectrometer [2, 5, 51] as described in Section 2.3. Starting with an aqueous solution, a compressed-gas atomizer (TSI model 3076) generates an aerosol consisting of droplets with an average diameter of approximately $1\ \mu\text{m}$. The water in the droplets then evaporates, leaving behind nanocrystals with a diameter that depends on the sample concentration. The nanocrystals are typically $100\ \text{nm}$ in diameter, and have approximately spherical shape [161]. Samples of NaCl, KI, KCl, and NH_4NO_3 were obtained from Fisher Scientific and diluted in ultrapure ($>18\ \text{M}\Omega$ resistivity) water. The samples were diluted to the same volume concentration (0.12%) to assure that the aerosol particles of different compositions would be the same size. The nanocrystals are focused using an aerodynamic lens (Aerodyne Research) [70], which uses a series of $\sim 2\ \text{mm}$ apertures to collimate the nanocrystal aerosol into a $\sim 0.5\ \text{mm}$ beam.

The collimated aerosol beam passes through a $1.5\ \text{mm}$ diameter skimmer and into the differentially pumped photoionization chamber, which reaches a pressure of 10^{-6} Torr (base pressure 10^{-9} Torr). The nanoparticles are then ionized by an intense ($\sim 10^{14}\ \text{W}/\text{cm}^2$), $800\ \text{nm}$, $40\ \text{fs}$ laser pulse, derived from a Ti:sapphire regenerative amplifier (KMLabs Wyvern HE) operating at $1\ \text{kHz}$. The pre-pulse contrast is greater than 250:1 as measured with a photodiode, and the pulse energies are varied between 5 to $100\ \mu\text{J}$.

The $10\ \text{mm}$ laser beam is focused with a $30\ \text{cm}$ lens to reach an estimated FWHM focal spot diameter of $25\ \mu\text{m}$. The resulting volume of the interaction region (assuming a $0.5\ \text{mm}$ collimated aerosol beam) is $2.5 \times 10^{-7}\ \text{cm}^3$. With an estimated aerosol density of 10^5 particles/ cm^3 , the laser pulse will interact with a particle every ~ 40 laser pulses, for an average of 25 hits per second at a $1\ \text{kHz}$ repetition rate. Thus, even with millisecond exposure times, we can identify the photofragments originating from a single nanocrystal. The actual hit rate observed experimentally depends on the volume of the laser focus that is above the threshold intensity for plasma formation and thus depends on the power of the incident laser beam.

For the two-pulse experiment, a BBO crystal is used to generate ~ 40 fs pulses of 400 nm light. The 400 nm and 800 nm pulses were delayed in time using a computer-controlled motorized delay stage placed in the 800 nm arm of a Mach–Zehnder interferometer. The photoions are accelerated towards the microchannel-plate phosphor detector using three electrodes in a velocity-map-imaging geometry [51], and the photoion distribution is recorded using a CCD camera (Allied Vision Technologies). The data is recorded at ~ 15 Hz. A series of PADs is shown in Figure C.1.

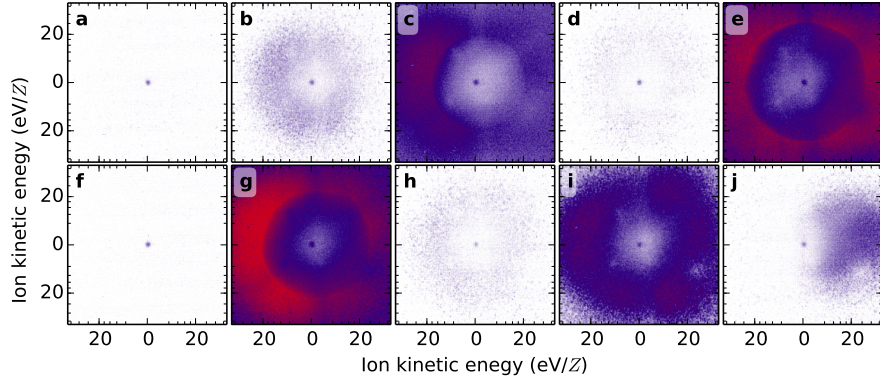


Figure C.1: **Nanoplasma explosions of NaCl nanoparticles with a single 800 nm laser pulse.** Panels a and f show no particles, while panels b, d, h, i, and j show diffuse plasma explosions. Frames c, e, and g display shock waves that were generated from particles subjected to laser intensities sufficient to initiate shock formation. The center of the frame corresponds to ions with zero kinetic energy, and the laser polarization is in the vertical direction. The laser propagates from left to right. Adapted with permission from Ref. 4. ©2014 American Physical Society

C.3 Dependence of shock formation on particle size

For the size-selected experiment, the nanoparticles were passed through a differential mobility analyser (TSI, models 3081 and 3085). To quantify the relative number of particles created by the atomizer, we used a scanning-mobility particle-sizer (SMPS) consisting of the differential mobility analyzer connected to a condensation particle counter (TSI, Model 3775). Figure C.2 presents the results of plasma formation in size-selected nanoparticles, and demonstrates that larger nanoparticles produce shock waves more frequently. The physical mechanism for this is not entirely clear, but may be a simple consequence of the fact that a larger nanoparticle contains more atoms and will therefore have a higher probability of generating enough “seed” electrons to ignite the avalanche breakdown

process. The fact that larger nanoparticles exhibit shock waves while the smaller particles do not, could also be a result of hydrodynamic expansions that takes place for larger particles in contrast with the Coulomb explosion physics that governs the expansion of smaller particles.

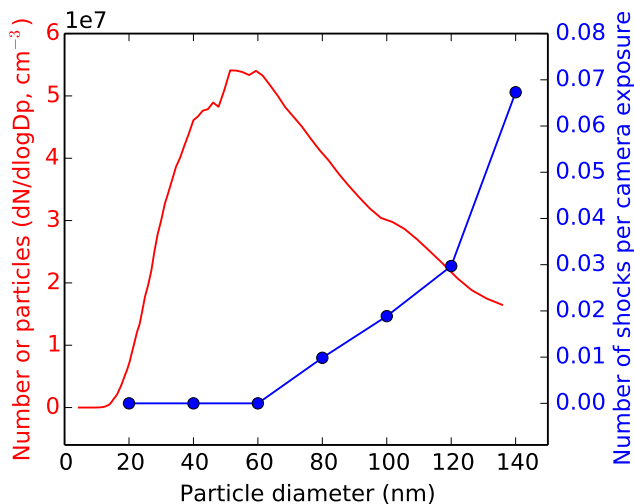


Figure C.2: **Effect of particle diameter of the formation of shock waves.** With a single 800 nm laser pulse with an intensity of $3 \times 10^{14} \text{ W}/\text{cm}^2$, the frequency of creating shocks in NaCl particles increases as the particle diameter becomes larger, even though the concentration of particles is decreasing for particle sizes larger than $\sim 60 \text{ nm}$. Larger nanoparticles absorb more energy per atom and can therefore create shocks throughout a larger region of the laser focal volume. Adapted with permission from Ref. 4. ©2014 American Physical Society

C.4 Effect of laser intensity on nanoplasma formation

Figure C.3 shows the effect of increasing the laser intensity on the total ion yield, the rate of shock wave formation, and the mean energy of the shock waves. The total ion yield shows a rapid increase with laser intensity, relating to the highly nonlinear nature of the avalanche ionization process. The appearance and energy of shock waves follow even steeper relationships with the laser intensity, quickly reaching saturation. Ammonium nitrate has the highest ionization potential of any of the compounds in this study, and the decrease in the ion yield is readily apparent in Figure C.3a. Interestingly, ammonium nitrate never displays shock waves when irradiated with a single laser pulse. However, it is possible that the laser intensity was simply not high enough to create shock

waves in ammonium nitrate.

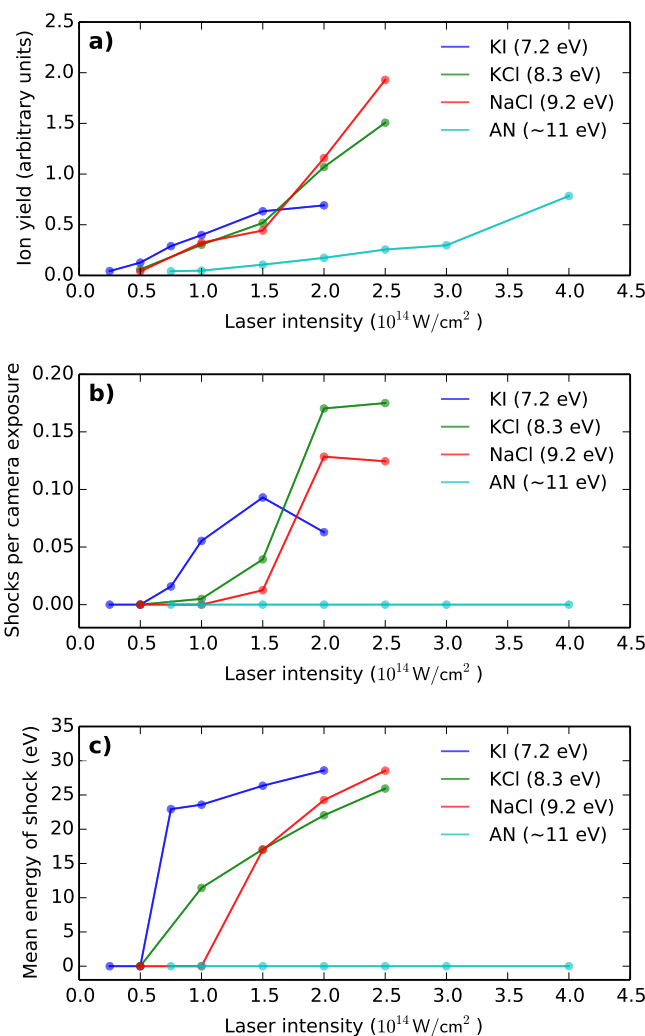


Figure C.3: **Ion yield and shock wave formation versus laser intensity.** (a) The ion yield suddenly increases with laser intensity, which is typical for avalanche ionization [114]. The threshold laser intensity increases with the ionization potential of the species (shown in parenthesis). The ionization potentials were obtained from the NIST webbook [162], except for NH_4NO_3 (ammonium nitrate, AN), which does not have a documented ionization potential, but is expected to have one similar to other compounds featuring a nitrate ($-\text{NO}_3$) moiety: between 11 and 12 eV. (b) The number of shocks generated per camera exposure increases rapidly at a threshold intensity, quickly saturating. (c) The average energy of the shocks increases with laser intensity until reaching an asymptotic value of $\sim 30 \text{ eV}/Z$. Notably, Ammonium nitrate requires higher laser intensity to achieve comparable ion yields and does not show any shocks in this one-pulse experiment. Adapted with permission from Ref. 4. ©2014 American Physical Society

C.5 Time-dependence of shock formation rate

Figure C.4 reveals the rate of shock formation increases rapidly and quickly saturates as the time-delay between the laser pulses is increased. Additionally, the minimum time-delay required to make shocks is slightly longer when the 800 nm laser pulse arrives first. It's likely that the 800 nm pulse does not deposit as much energy into the plasma and causes the plasma to expand more slowly, therefore taking slightly longer to become highly absorbing of the subsequent 400 nm pulse. It's possible that a series of three or more laser pulses can be used to shape the plasma density profile in order to further optimize the rate of shock production.

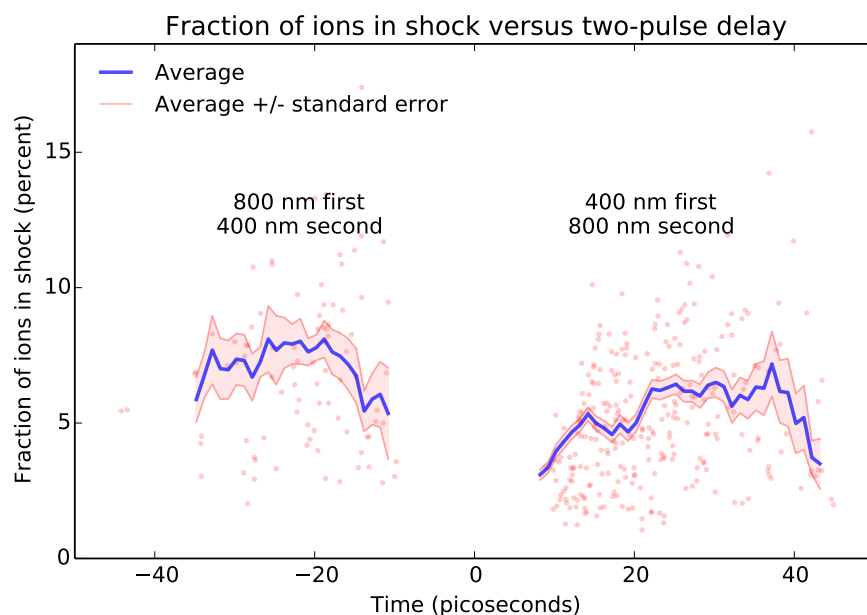


Figure C.4: **The fraction of ions in the shock controlled with two-pulse delay.** Each dot corresponds to a single shock wave generated from a NH_4NO_3 nanoparticle. The relative number of ions in each shock wave compared to the total number of ions is estimated by fitting the ion distribution with two Gaussian functions (Figure 5.3d): one wide Gaussian for the broad “background” ions and a narrow Gaussian for the ions in the shock wave. At time delays of 10 ps, the shock waves do not contain many ions compared to the background. However, the fraction of ions in the shock is enhanced at an optimal time delay around 30 ps. Adapted with permission from Ref. 4. ©2014 American Physical Society

C.6 Hydrodynamic simulations

To investigate the mechanisms for shock wave formation, hydrodynamic simulations were performed using version 9.0 of the HYDRA radiation-hydrodynamics code [133] for NaCl nanoparticles of 100 nm radius. These simulations were completed by Dr. Jim Gaffney at Lawrence Livermore National Laboratory. The HYDRA calculations were performed in 1D, by assuming spherical symmetry, using the 3D version of HYDRA. We note that this version of HYDRA, which uses finite elements methods (rather than finite difference methods) for transport calculations, is more appropriate for these plasmas. Simulations used an adaptive one (radial) dimensional Lagrangian mesh, which uses a smaller grid zones near regions of rapidly changing plasma density. Thus, the calculations give a reliable description of sharp spatial features (such as shock waves). Furthermore, the calculations include models for laser energy deposition via inverse bremsstrahlung (IB) along with accurate equation of state and thermal transport quantities.

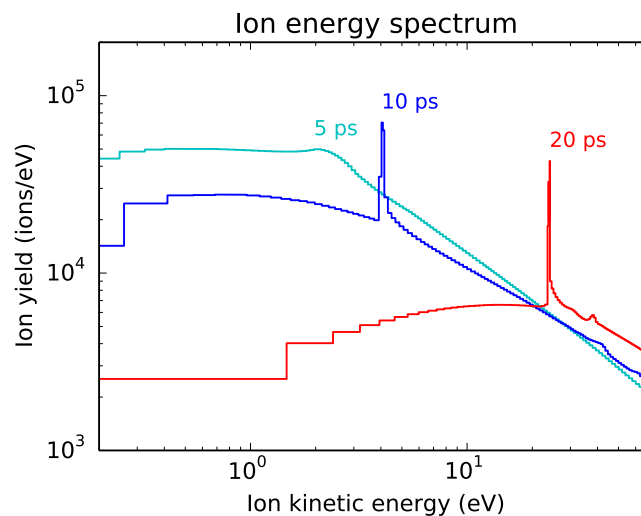


Figure C.5: **HYDRA simulations at various two-pulse delays.** Hydrodynamic simulations completed using the HYDRA [133] radiation-hydrodynamics code reveal that two time-delayed 800 nm laser pulses, both with intensities of 4.9×10^{14} W/cm², will generate quasi-monoenergetic shocks in the ion kinetic-energy spectrum only when the time delay is less than ~ 35 ps. The shock does not show up as a sharp peak for the time delay of 5 ps, but when the time delay is increased to 10 ps, the shock displays as a sharp peak, in agreement with experimental findings. Adapted with permission from Ref. 4. ©2014 American Physical Society

The hydrodynamic calculations confirm that a shock wave is produced in the expanding nanoplasma and that this shock manifests as a step in the plasma density as well as a spike in the ion kinetic energy distribution (Figures 5.5, C.5, and C.6). The simulations indicate that the simulated spike in the ion kinetic energy distribution is quite sensitive to the parameters of the laser pulse; in this work we have chosen intensities to match the experimentally observed ion energy of ~ 20 eV with the 20 ps delay between the two laser pulses. This results in a simulated laser intensity of 5×10^{14} W/cm² which is consistent with the estimated experimental laser intensity.

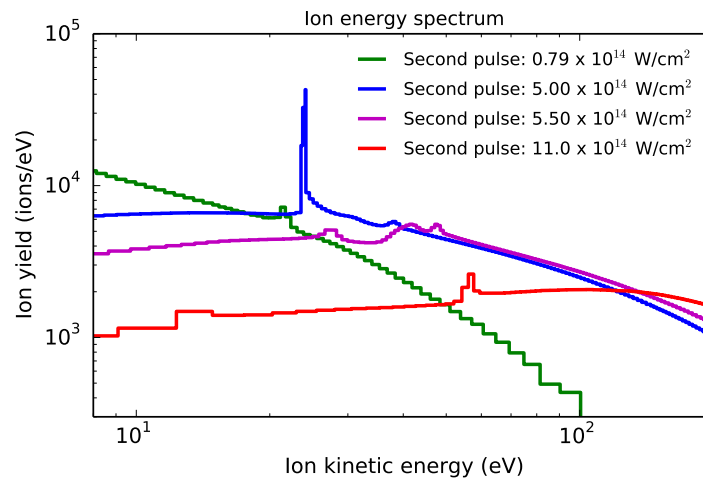


Figure C.6: **Scaling of the shock with laser intensity using HYDRA.** The ion kinetic energy distribution from two laser pulses delayed by 20 ps as calculated by hydrodynamic simulations using the HYDRA software [133]. The intensity of the first pulse is 4.9×10^{14} W/cm². Increasing the intensity of the second pulse from 0.79×10^{14} W/cm² to 1.1×10^{15} W/cm² increases the energy of the quasi-monoenergetic ions produced by the shock wave by about 5 times. However, the shape of the peak in the ion distribution is extremely sensitive to the laser intensity, with $\sim 10\%$ changes in the laser intensity transforming a single sharp peak into three broad peaks. Adapted with permission from Ref. 4. ©2014 American Physical Society

The simulations start with a +1 ionized plasma, making the approximation that the initial ionization of cold material occurs very rapidly. Using the Ammosov, Delone, and Krainov (ADK) ionization model [1] we calculate that for our laser parameters, initial ionization of the particle occurs well before the peak of the laser pulse, after which IB becomes the dominant process and the HYDRA will model the plasma adequately. The small size of the nanoparticles combined with the relatively high temperatures created by the second laser pulse mean that the thermal electron mean

free path is larger than the spatial mesh zone size, making non-local energy transport important. A model for non-local energy transport is implemented in HYDRA [163], and we include this in the presented simulations.

The HYDRA calculations make two additional approximations: 1) that the net charge of the plasma is small and 2) that the electron energy distribution can be described by a Maxwellian distribution. Both of these approximations are valid in the regime of the large nanoparticles and sub-picosecond laser pulses used in this study. Regarding the first approximation, we show (Section C.7) that due to the low laser intensities used in this study, only a small fraction of the electrons will be able to leave the plasma during the laser pulse. Therefore, the plasma is nearly net-neutral and can be modeled as a hydrodynamic expansion. The second approximation, that the electrons energy distribution can be described as Maxwellian, is valid because the excited electrons will thermalize on a very rapid timescale compared to the picosecond timescale of the HYDRA simulations. The electron thermalization time can be estimated from the electron-electron energy exchange rate [164]:

$$\tau = 3.44 \times 10^5 \frac{T_e^{3/2}}{N_e \lambda} \text{ seconds}, \quad (\text{C.1})$$

where T_e is the electron temperature, N_e is the density of the electrons, and $\lambda \approx 3$ is the Coulomb Logarithm [164]. Electron thermalization will be the slowest at the time of the second pulse, when electron temperatures are high and the plasma is lower density than during the first pulse. In the region of high-pressure that drives the observed shock, typical simulated conditions are $T_e = 20$ eV and $N_e = 5 \times 10^{21} \text{ cm}^{-3}$. The timescale for electron thermalization is then ~ 0.6 fs, very fast compared to the hydrodynamic motion of interest in this study.

Consistency between the simulated velocity distribution and the experimentally recorded velocity distribution has been checked by numerically propagating the velocity distribution towards a “detector” using a simulated electric field. This analysis used the simulated velocity profile taken 80 ps after the second laser pulse, the point at which we estimate the VMI field separates electron and ion clouds, allowing the ions to propagate to the detector without further interactions. The true process of image formation is complex, and has not yet been modeled, however we have confirmed

that sharp structures in VMI images correspond to peaks in the kinetic energy distribution. That is, the VMI works the way it usually does, even for expanding plasmas.

C.7 Plasma quasi-neutrality

In contrast to most previous studies of nanoplasmas [38, 41, 114, 125, 128, 134], this study uses ~ 100 nm nanoparticles (containing on the order of 10^7 atoms) versus < 10 nm noble gas clusters (containing on the order of 10^3 or 10^4 atoms). One important effect of this size difference is that the most of the electrons in these larger plasmas cannot escape the plasma, producing a nanoplasma that has a small charge imbalance (a quasi-neutral plasma). There are several reasons for this difference. First, the excursion distance for laser-field-driven electrons is comparatively smaller for larger nanoplasmas – much less than the cluster radius – preventing the majority of electrons from being driven outside of the ion cloud by the laser field. Second, even if a very small fraction of the electrons leave the plasma, a massive charge builds up, preventing the majority of the electrons from escaping the nanoplasma.

Here we estimate the fraction of electrons that can leave the nanoplasma $\Delta N_e/N_e$, based on energy considerations. When free electrons are driven out of the cluster by the laser electric field, the charge imbalance creates a potential well. If too many electrons leave the cluster, the potential energy E_{pot} due to excess charge will become larger than the kinetic energy of the escaping electrons E_{kin} , which will prevent further electron escape. One can estimate $\Delta N_e/N_e$ by equating E_{pot} to E_{kin} , assuming that the excess charge is uniformly distributed within the cluster. Since the potential energy is given by

$$E_{\text{pot}} = \frac{N e^2}{4\pi\epsilon_0 R} \frac{\Delta N_e}{N_e}, \quad (\text{C.2})$$

and taking

$$E_{\text{kin}} = 4 \frac{e^2}{4\pi\epsilon_0 a_{\text{Bohr}}} \approx 100 \text{ eV}, \quad (\text{C.3})$$

we get

$$\frac{\Delta N_e}{N_e} = \frac{4R}{N a_{\text{Bohr}}} = \frac{4R[\text{a.u.}]}{N} = 10^{-3}, \quad (\text{C.4})$$

which corresponds to 0.1% of the electrons leaving the cluster. It should be noted that the small kinetic energy of the electrons (~ 100 eV, due to the low laser intensity) plays an important role for keeping the electrons inside the cluster. The electrons are simply not energetic enough to overcome the potential barrier, which arises due to charge imbalance.

The predicted 0.1% ionization for large clusters is in sharp contrast to small noble gas clusters used in previous studies. As an example, for $R = 5$ nm (94 a.u.), $N = 10^4$, and $E_{\text{kin}} \approx 1$ KeV, we get

$$\frac{\Delta N_e}{N_e} = \frac{40R}{Na_{\text{Bohr}}} \approx \frac{(40)(94)}{10^4} \approx 0.4, \quad (\text{C.5})$$

i.e. $\sim 40\%$ of the electrons leave the cluster. This analysis reveals why small clusters become highly charged and undergo fast Coulomb explosion while larger clusters remain quasi-neutral and undergo a slow hydrodynamic expansion.

References

- [1] M. V. Ammosov, N. B. Delone, and V. P. Krainov. Tunnel ionization of complex atoms and of atomic ions in an alternating electromagnetic field. *Sov. Phys. JETP*, 64, **1986**, 1191–1194. URL: http://www.jetp.ac.ru/cgi-bin/dn/e/_064/_06/_1191.pdf (cited on pages i, 54, 65, 67, 103).
- [2] D. D. Hickstein, P. Ranitovic, S. Witte, X.-M. Tong, Y. Huismans, P. Arpin, X. Zhou, K. E. Keister, C. Hogle, B. Zhang, C. Ding, P. Johnsson, N. Toshima, M. J. J. Vrakking, M. M. Murnane, and H. C. Kapteyn. Direct Visualization of Laser-Driven Electron Multiple Scattering and Tunneling Distance in Strong-Field Ionization. *Phys. Rev. Lett.*, 109, **2012**, 073004. DOI: 10.1103/PhysRevLett.109.073004 (cited on pages iii, 30, 34, 36, 40, 43, 48, 51, 64, 81, 84, 86–88, 97).
- [3] D. D. Hickstein, F. Dollar, J. L. Ellis, K. J. Schnitzenbaumer, K. E. Keister, G. M. Petrov, C. Ding, B. B. Palm, J. A. Gaffney, M. E. Foord, S. B. Libby, G. Dukovic, J. L. Jimenez, H. C. Kapteyn, M. M. Murnane, and W. Xiong. Mapping Nanoscale Absorption of Femtosecond Laser Pulses using Plasma Explosion Imaging. *ACS Nano*, 8 (9), **2014**, 8810. DOI: 10.1021/nm503199v (cited on pages iii, 45, 47, 49, 52, 55–57, 61, 89, 93, 95).
- [4] D. D. Hickstein, F. Dollar, J. A. Gaffney, M. E. Foord, G. M. Petrov, B. B. Palm, K. E. Keister, J. L. Ellis, C. Ding, S. B. Libby, J. L. Jimenez, H. C. Kapteyn, M. M. Murnane, and W. Xiong. Observation and Control of Shock Waves in Individual Nanoplasmas. *Phys. Rev. Lett.*, 112 (11), **2014**, 115004. DOI: 10.1103/PhysRevLett.112.115004 (cited on pages iii, 48, 49, 51, 54, 62, 65, 66, 68, 70, 96, 98–103).
- [5] W. Xiong, D. D. Hickstein, K. J. Schnitzenbaumer, J. L. Ellis, B. B. Palm, K. E. Keister, C. Ding, L. Miaja-Avila, G. Dukovic, J. L. Jimenez, M. M. Murnane, and H. C. Kapteyn. Photoelectron Spectroscopy of CdSe Nanocrystals in the Gas Phase: A Direct Measure of the Evanescent Electron Wave Function of Quantum Dots. *Nano Lett.*, 13, **2013**, 2924. DOI: 10.1021/nl401309z (cited on pages iv, 51, 64, 76, 97).
- [6] C. Mancuso, D. D. Hickstein, P. Grychtol, O. Kfir, X.-M. Tong, R. Knut, F. Dollar, D. Zusin, M. Gopalakrishnan, C. Gentry, E. Turgut, J. L. Ellis, M.-C. Chen, A. Fleischer, O. Cohen, H. C. Kapteyn, and M. M. Murnane. Strong Field Ionization Tomography with Two-color Circularly Polarized Femtosecond Laser Fields. *Submitted*, **2014** (cited on pages iv, 73).

- [7] J. L. Ellis, D. D. Hickstein, K. J. Schnitzenbaumer, M. B. Wilker, B. B. Palm, J. L. Jimenez, G. Dukovic, H. C. Kapteyn, M. M. Murnane, and W. Xiong. Electron transfer dynamics in gas-phase and solvated quantum dots. *In preparation*, **2014** (cited on page iv).
- [8] Z. Han, S. Niu, C. Shang, Z. Liu, and L. Ren. Light trapping structures in wing scales of butterfly *Trogonoptera brookiana*. *Nanoscale*, 4 (9), **2012**, 2879. DOI: 10.1039/c2nr12059c (cited on page 1).
- [9] H. E. Edgerton. **Bullet Through Apple**. Edgerton Digital Archives, MIT Museum, Cambridge MA, 1964. URL: <http://edgerton-digital-collections.org> (cited on page 2).
- [10] A. McPherson, G. Gibson, H. Jara, U. Johann, T. S. Luk, I. A. McIntyre, K. Boyer, and C. K. Rhodes. Studies of multiphoton production of vacuum-ultraviolet radiation in the rare gases. *J. Opt. Soc. Am. B*, 4 (4), **1987**, 595–601. DOI: 10.1364/JOSAB.4.000595 (cited on pages 3, 7, 32).
- [11] C. G. Durfee, A. R. Rundquist, S. Backus, C. Herne, M. M. Murnane, and H. C. Kapteyn. Phase Matching of High-Order Harmonics in Hollow Waveguides. *Phys. Rev. Lett.*, 83 (11), **1999**, 2187. DOI: 10.1103/PhysRevLett.83.2187 (cited on pages 3, 7).
- [12] T. Popmintchev, M.-C. Chen, P. Arpin, M. M. Murnane, and H. C. Kapteyn. The attosecond nonlinear optics of bright coherent X-ray generation. *Nature Phot.*, 4 (12), **2010**, 822–832. DOI: 10.1038/nphoton.2010.256 (cited on pages 3, 7, 9, 14).
- [13] L. Miaja-Avila, J. Yin, S. Backus, G. Saathoff, M. Aeschlimann, M. Murnane, and H. Kapteyn. Ultrafast studies of electronic processes at surfaces using the laser-assisted photoelectric effect with long-wavelength dressing light. *Phys. Rev. A*, 79, **2009**, 030901. DOI: 10.1103/PhysRevA.79.030901 (cited on page 6).
- [14] Z. Xie, T. Z. Markus, G. Gotesman, Z. Deutsch, D. Oran, and R. Naaman. How Isolated Are the Electronic States of the Core in Core/Shell Nanoparticles? *ACS Nano*, 5 (2), **2011**, 863–869. DOI: 10.1021/nn102002x (cited on page 6).
- [15] H. Borchert, D. V. Talapin, C. McGinley, S. Adam, A. Lobo, A. R. B. de Castro, T. Moller, and H. Weller. High resolution photoemission study of CdSe and CdSe/ZnS core-shell nanocrystals. *J. Chem. Phys.*, 119 (3), **2003**, 1800–1807. DOI: 10.1063/1.1580096 (cited on page 6).
- [16] P. Agostini, F. Fabre, G. Mainfray, G. Petite, and N. Rahman. Free-Free Transitions Following Six-Photon Ionization of Xenon Atoms. *Phys. Rev. Lett.*, 42 (17), **1979**, 1127–1130. DOI: 10.1103/PhysRevLett.42.1127 (cited on pages 7, 32).
- [17] R. A. Bartels, A. Paul, H. Green, H. C. Kapteyn, M. M. Murnane, S. Backus, I. P. Christov, Y. Liu, D. Attwood, and C. Jacobsen. Generation of spatially coherent light at extreme ultraviolet wavelengths. *Science*, 297, **2002**, 376. DOI: 10.1126/science.1071718 (cited on page 7).
- [18] A. Rundquist, C. G. Durfee, Z. Chang, C. Herne, S. Backus, M. M. Murnane, and H. C. Kapteyn. Phase-Matched Generation of Coherent Soft X-rays. *Science*, 280, **1998**, 1412. DOI: 10.1126/science.280.5368.1412 (cited on page 7).

- [19] T. Popmintchev, M.-C. Chen, D. Popmintchev, P. Arpin, S. Brown, S. Alisauskas, G. Andriukaitis, T. Balciunas, O. D. Mücke, A. Pugzlys, A. Baltuska, B. Shim, S. E. Schrauth, A. Gaeta, C. Hernández-García, L. Plaja, A. Becker, A. Jaron-Becker, M. M. Murnane, and H. C. Kapteyn. Bright coherent ultrahigh harmonics in the keV X-ray regime from mid-infrared femtosecond lasers. *Science*, 336, **2012**, 1287. DOI: 10.1126/science.1218497 (cited on pages 7, 9, 15).
- [20] E. Gagnon, P. Ranitovic, X.-M. Tong, C. L. Cocke, M. M. Murnane, H. C. Kapteyn, and A. S. Sandhu. Soft X-ray-driven femtosecond molecular dynamics. *Science*, 317, **2007**, 1374–8. DOI: 10.1126/science.1144920 (cited on page 7).
- [21] W. Li, X. Zhou, R. Lock, and S. Patchkovskii. Time-Resolved Dynamics in N₂O₄ Probed Using High Harmonic Generation. *Science*, 322, **2008**, 1207–1211. DOI: 10.1126/science.1163077 (cited on page 7).
- [22] X. Zhou, P. Ranitovic, C. W. Hogle, J. H. D. Eland, H. C. Kapteyn, and M. M. Murnane. Probing and controlling non-BornOppenheimer dynamics in highly excited molecular ions. *Nature Phys.*, 8 (3), **2012**, 232–237. DOI: 10.1038/nphys2211 (cited on page 7).
- [23] K. Hoogeboom-Pot, D. Nardi, J. N. Hernandez-Charpak, E. Anderson, X. Gu, R. Yang, H. Kapteyn, and M. Murnane. A New Regime of Nanoscale Thermal Transport: Collective Diffusion Counteracts Dissipation Inefficiency. *ArXiv preprint*, **2014**, 1407.0658. DOI: 10.1364/UP.2014.10.Thu.E.1 (cited on page 7).
- [24] C. La-O-Vorakiat, E. Turgut, C. A. Teale, H. C. Kapteyn, M. M. Murnane, S. Mathias, M. Aeschlimann, C. M. Schneider, J. M. Shaw, H. T. Nembach, and T. J. Silva. Ultrafast Demagnetization Measurements Using Extreme Ultraviolet Light: Comparison of Electronic and Magnetic Contributions. *Phys. Rev. X*, 2 (1), **2012**, 011005. DOI: 10.1103/PhysRevX.2.011005 (cited on page 7).
- [25] R. Sandberg, A. Paul, D. Raymondson, S. Hädrich, D. Gaudiosi, J. Holtsnider, R. Tobey, O. Cohen, M. Murnane, H. Kapteyn, C. Song, J. Miao, Y. Liu, and F. Salmassi. Lensless Diffractive Imaging Using Tabletop Coherent High-Harmonic Soft-X-Ray Beams. *Phys. Rev. Lett.*, 99 (9), **2007**, 098103. DOI: 10.1103/PhysRevLett.99.098103 (cited on page 7).
- [26] M. D. Seaberg, D. E. Adams, E. L. Townsend, D. a. Raymondson, W. F. Schlotter, Y. Liu, C. S. Menoni, L. Rong, C.-C. Chen, J. Miao, H. C. Kapteyn, and M. M. Murnane. Ultrahigh 22 nm resolution coherent diffractive imaging using a desktop 13 nm high harmonic source. *Opt. Express*, 19 (23), **2011**, 22470–9. DOI: 10.1364/OE.19.022470 (cited on page 7).
- [27] C. I. Blaga, J. Xu, A. D. DiChiara, E. Sistrunk, K. Zhang, P. Agostini, T. A. Miller, L. F. DiMauro, and C. D. Lin. Imaging ultrafast molecular dynamics with laser-induced electron diffraction. *Nature*, 483 (7388), **2012**, 194–197. DOI: 10.1038/nature10820 (cited on pages 7, 32).
- [28] J. Xu, Z. Chen, A.-T. Le, and C. D. Lin. Self-imaging of molecules from diffraction spectra by laser-induced rescattering electrons. *Phys. Rev. A*, 82 (3), **2010**, 033403. DOI: 10.1103/PhysRevA.82.033403 (cited on pages 7, 32).

- [29] J. Xu, C. I. Blaga, K. Zhang, Y. H. Lai, C. D. Lin, T. a. Miller, P. Agostini, and L. F. DiMauro. Diffraction using laser-driven broadband electron wave packets. *Nature Comm.*, 5, **2014**, 4635. DOI: 10.1038/ncomms5635 (cited on pages 7, 32, 74).
- [30] P. B. Corkum. Plasma perspective on strong field multiphoton ionization. *Phys. Rev. Lett.*, 71 (13), **1993**, 1994–1997. DOI: 10.1103/PhysRevLett.71.1994 (cited on pages 8, 9, 32, 36).
- [31] D. L. Andrews and A. A. Demidov. **An Introduction to Laser Spectroscopy**. 2nd. Springer Science and Business Media, 2002, p. 281 (cited on page 9).
- [32] M. C. Chen, C. Hernández-García, C. Mancuso, F. Dollar, B. Galloway, D. Popmintchev, P. C. Huang, B. Walker, L. Plaja, A. Jaron-Becker, A. Becker, T. Popmintchev, M. M. Murnane, and H. C. Kapteyn. Generation of Bright Isolated Attosecond Soft X-Ray Pulses Driven by Multi-Cycle Mid-Infrared Lasers. *Proc. Natl. Acad. Sci.*, **2014**, E2361–E2367. DOI: 10.1073/pnas.1407421111. arXiv: 1401.0240 (cited on pages 9, 15, 76).
- [33] C. Hernández-García, J. A. Pérez-Hernández, T. Popmintchev, M. M. Murnane, H. C. Kapteyn, A. Jaron-Becker, A. Becker, and L. Plaja. Zeptosecond High Harmonic keV X-Ray Waveforms Driven by Midinfrared Laser Pulses. *Phys. Rev. Lett.*, 111 (3), **2013**, 033002. DOI: 10.1103/PhysRevLett.111.033002 (cited on pages 9, 31).
- [34] N. Felidj, J. Aubard, G. Levi, J. R. Krenn, A. Hohenau, G. Schider, A. Leitner, and F. R. Aussenegg. Optimized surface-enhanced Raman scattering on gold nanoparticle arrays. *Appl. Phys. Lett.*, 82 (18), **2003**, 3095. DOI: 10.1063/1.1571979 (cited on page 10).
- [35] E. C. L. Ru, E. Blackie, M. Meyer, and P. G. Etchegoin. Surface Enhanced Raman Scattering Enhancement Factors : A Comprehensive Study. *J. Phys. Chem. C*, 111, **2007**, 13794–13803. DOI: 10.1021/jp0687908 (cited on pages 10, 47).
- [36] V. K. Valev, D. Denkova, X. Zheng, A. I. Kuznetsov, C. Reinhardt, B. N. Chichkov, G. Tsutsumanova, E. J. Osley, V. Petkov, B. De Clercq, A. V. Silhanek, Y. Jeyaram, V. Volskiy, P. a. Warburton, G. a. E. Vandenbosch, S. Russev, O. a. Aktsipetrov, M. Ameloot, V. V. Moshchalkov, and T. Verbiest. Plasmon-enhanced sub-wavelength laser ablation: plasmonic nanojets. *Adv. Opt. Mat.*, 24 (10), **2012**, OP29–35. DOI: 10.1002/adma.201103807 (cited on page 10).
- [37] G. M. Petrov, J. Davis, A. L. Velikovich, P. Kepple, A. Dasgupta, and R. W. Clark. Dynamics of a Xe cluster plasma produced by an intense ultrashort pulse KrF laser. *Phys. Plasmas*, 12 (6), **2005**, 063103. DOI: 10.1063/1.1928367 (cited on pages 11, 63, 67).
- [38] T. Ditmire, J. W. G. Tisch, E. Springate, M. B. Mason, N. Hay, J. P. Marangos, and M. H. R. Hutchinson. High Energy Ion Explosion of Atomic Clusters: Transition from Molecular to Plasma Behavior. *Phys. Rev. Lett.*, 78, **1997**, 2732. DOI: 10.1103/PhysRevLett.78.2732 (cited on pages 11, 47, 49, 63, 64, 75, 105).
- [39] T. Ditmire, J. Zweiback, V. P. Yanovsky, T. E. Cowan, and G. Hays. Nuclear fusion from explosions of femtosecond laser-heated deuterium clusters. *Nature*, 398, **1999**, 489–492. DOI: 10.1038/19037 (cited on pages 11, 63).

- [40] A. E. Kaplan, B. Y. Dubetsky, and P. L. Shkolnikov. Shock Shells in Coulomb Explosions of Nanoclusters. *Phys. Rev. Lett.*, 91 (14), **2003**, 143401. DOI: 10.1103/PhysRevLett.91.143401 (cited on pages 11, 47, 63, 69, 71, 80).
- [41] F. Peano, R. A. Fonseca, J. L. Martins, and L. O. Silva. Controlled shock shells and intra-cluster fusion reactions in the explosion of large clusters. *Phys. Rev. A*, 73 (5), **2006**, 053202. DOI: 10.1103/PhysRevA.73.053202 (cited on pages 11, 63, 75, 105).
- [42] F. Peano, R. A. Fonseca, and L. O. Silva. Dynamics and Control of Shock Shells in the Coulomb Explosion of Very Large Deuterium Clusters. *Phys. Rev. Lett.*, 94 (3), **2005**, 033401. DOI: 10.1103/PhysRevLett.94.033401 (cited on pages 11, 47, 63, 69, 71, 75).
- [43] S. Backus, C. G. Durfee, M. M. Murnane, and H. C. Kapteyn. High power ultrafast lasers. *Rev. Sci. Instrum.*, 69 (3), **1998**, 1207. DOI: 10.1063/1.1148795 (cited on page 13).
- [44] C. Ding, W. Xiong, T. Fan, D. D. Hickstein, T. Popmintchev, X. Zhang, M. Walls, M. M. Murnane, and H. C. Kapteyn. High flux coherent super-continuum soft X-ray source driven by a single-stage, 10mJ, Ti:sapphire amplifier-pumped OPA. *Opt. Express*, 22 (5), **2014**, 6194. DOI: 10.1364/OE.22.006194 (cited on pages 13, 14, 34).
- [45] C. Ding. Bright Coherent Ultrafast Tabletop Light Sources Development and the Application on EUV to Soft X-Ray Absorption Spectroscopy. *University of Colorado PhD Thesis*, **2014**. URL: <http://jila.colorado.edu/publications/theses> (cited on pages 13, 14).
- [46] G. Cerullo and S. De Silvestri. Ultrafast optical parametric amplifiers. *Rev. Sci. Instrum.*, 74, **2003**, 0034–6748. DOI: 10.1063/1.1523642 (cited on page 14).
- [47] M.-C. Chen, P. Arpin, T. Popmintchev, M. Gerrity, B. Zhang, M. Seaberg, D. Popmintchev, M. M. Murnane, and H. C. Kapteyn. Bright, Coherent, Ultrafast Soft X-Ray Harmonics Spanning the Water Window from a Tabletop Light Source. *Phys. Rev. Lett.*, 105, **2010**, 173901. DOI: 10.1103/PhysRevLett.105.173901 (cited on pages 14, 15).
- [48] D. W. Chandler and P. L. Houston. Two-dimensional imaging of state-selected photodissociation products detected by multiphoton ionization. *J. Chem. Phys.*, 87 (2), **1987**, 1445. DOI: 10.1063/1.453276 (cited on pages 16, 17).
- [49] H. Helm, N. Bjerre, M. J. Dyer, D. L. Huestis, and M. Saeed. Images of Photoelectron Formed in Intense Laser Fields. *Phys. Rev. Lett.*, 70 (21), **1993**, 3221. DOI: 10.1103/PhysRevLett.70.3221 (cited on page 16).
- [50] C Bordas, M. Dyer, T Fairfield, H Helm, and K. Kulander. Unexpected product fine-structure distributions in (3+1)-photon ionization of xenon. *Phys. Rev. A*, 51 (5), **1995**, 3726. DOI: 10.1103/PhysRevA.51.3726 (cited on page 16).
- [51] A. T. J. B. Eppink and D. H. Parker. Velocity map imaging of ions and electrons using electrostatic lenses: Application in photoelectron and photofragment ion imaging of molecular oxygen. en. *Rev. Sci. Instrum.*, 68 (9), **1997**, 3477–3484. DOI: 10.1063/1.1148310 (cited on pages 17–19, 32, 35, 48, 51, 64, 65, 90, 97, 98).

- [52] B. J. Whitaker. **Imaging in Molecular Dynamics: Technology and Applications (A User's Guide)**. Cambridge, UK: Cambridge University Press, 2003 (cited on pages 17, 18, 24).
- [53] P. Johnsson, A. Rouzée, W. Siu, Y. Huismans, F. Lépine, T. Marchenko, S. Düsterer, F. Tavella, N. Stojanovic, H. Redlin, A. Azima, and M. J. J. Vrakking. Characterization of a two-color pump-probe setup at FLASH using a velocity map imaging spectrometer. *Optics Lett.*, 35 (24), **2010**, 4163. DOI: 10.1364/OL.35.004163 (cited on page 17).
- [54] M. Stei, J. von Vangerow, R. Otto, A. H. Kelkar, E. Carrascosa, T. Best, and R. Wester. High resolution spatial map imaging of a gaseous target. *J. Chem. Phys.*, 138 (21), **2013**, 214201. DOI: 10.1063/1.4807482 (cited on page 17).
- [55] S. Thorin. Design and construction of a velocity map imaging spectrometer. PhD thesis. Lund, 2004. URL: http://old-atto.fysik.lth.se/publications/master/Thorin_LRAP-327.pdf (cited on pages 17, 18).
- [56] D. Manura and D. Dahl. **SIMION 8.0**. Ringoes, NJ: Scientific Instrument Services, Inc., 2008. URL: <http://simion.com/manual/> (cited on page 18).
- [57] C. L. Adams, H. Schneider, K. M. Ervin, and J. M. Weber. Low-energy photoelectron imaging spectroscopy of nitromethane anions: Electron affinity, vibrational features, anisotropies, and the dipole-bound state. *J. Chem. Phys.*, 130 (7), **2009**, 074307. DOI: 10.1063/1.3076892 (cited on page 19).
- [58] A. Sanov and W. C. Lineberger. Dynamics of cluster anions: a detailed look at condensed-phase interactions. *PhysChemComm*, 5 (25), **2002**, 165. DOI: 10.1039/b209239e (cited on page 19).
- [59] A. Sanov and W. C. Lineberger. Cluster anions: Structure, interactions, and dynamics in the sub-nanoscale regime. *Phys. Chem. Chem. Phys.*, 6 (9), **2004**, 2018. DOI: 10.1039/b400524d (cited on page 19).
- [60] R. V. Latham. **High Voltage Vacuum Insulation**. Academic Press, 1995. DOI: 10.1016/B978-012437175-0/50000-2 (cited on page 20).
- [61] Beam Dynamics Skimmer Specification Sheet. In: **Beam Dynamics, Inc.** Beam Dynamics, Inc. URL: www.beamdynamicsinc.com/skimmer_specs2.htm (cited on page 21).
- [62] **Phosphor Specifications Chart**. Beam Imaging Solutions, 2012. URL: <http://www.beamimaging.com/pscreen.html> (cited on page 23).
- [63] D. Townsend, S. Kyoung Lee, and A. G. Suits. Orbital polarization from DC slice imaging: S(1D2) alignment in the photodissociation of ethylene sulfide. *Chem. Phys.*, 301, **2004**, 197–208. DOI: 10.1016/j.chemphys.2003.10.020 (cited on page 24).
- [64] V. Dribinski, A. Ossadtchi, V. A. Mandelshtam, and H. Reisler. Reconstruction of Abel-transformable images: The Gaussian basis-set expansion Abel transform method. *Rev. Sci. Instrum.*, 73 (7), **2002**, 2634–2642. DOI: 10.1063/1.1482156 (cited on pages 24, 35).

- [65] M. J. J. Vrakking. An iterative procedure for the inversion of two-dimensional ion/photoelectron imaging experiments. *Rev. Sci. Instrum.*, 72, **2001**, 4084. DOI: 10.1063/1.1406923 (cited on page 24).
- [66] G. M. Roberts, J. L. Nixon, J. Lecointre, E. Wrede, and J. R. R. Verlet. Toward real-time charged-particle image reconstruction using polar onion-peeling. *Rev. Sci. Instrum.*, 80 (5), **2009**, 053104. DOI: 10.1063/1.3126527 (cited on page 24).
- [67] K. R. May. The Collison nebulizer: description, performance and application. *Aerosol Sci.*, 4 (3), **1973**, 235. DOI: 10.1016/0021-8502(73)90006-2 (cited on page 25).
- [68] P. Liu, P. J. Ziemann, and D. B. Kittelson. Aerosol Science and Technology Generating Particle Beams of Controlled Dimensions and Divergence: I . Theory of Particle Motion in Aerodynamic Lenses and Nozzle Expansions. *Aerosol Sci. and Tech.*, 22, **1995**, 293–313. DOI: 10.1080/02786829408959748 (cited on page 27).
- [69] P. Liu, P. J. Ziemann, D. B. Kittelson, and P. H. McMurry. Generating Particle Beams of Controlled Dimensions and Divergence: II. Experimental Evaluation of Particle Motion in Aerodynamic Lenses and Nozzle Expansions. *Aerosol Sci. and Tech.*, 22 (3), **1995**, 314–324. DOI: 10.1080/02786829408959749 (cited on page 27).
- [70] P. S. K. Liu, R. Deng, K. A. Smith, L. R. Williams, J. T. Jayne, M. R. Canagaratna, K. Moore, T. B. Onasch, D. R. Worsnop, and T. Deshler. Transmission Efficiency of an Aerodynamic Focusing Lens System: Comparison of Model Calculations and Laboratory Measurements for the Aerodyne Aerosol Mass Spectrometer. *Aerosol Sci. and Tech.*, 41, **2007**, 721–733. DOI: 10.1080/02786820701422278 (cited on pages 28, 50, 90, 97).
- [71] M. Ferray, A. L’Huillier, X. F. Li, L. A. Lompre, G. Maunfray, and C. Manus. Multiple-harmonic conversion of 1064 nm radiation in rare gases. *J. Phys. B*, 21, **1988**, L31–L35. DOI: 10.1088/0953-4075/21/3/001 (cited on page 32).
- [72] C. T. L. Smeenk, L. Arissian, A. V. Sokolov, M. Spanner, K. F. Lee, A. Staudte, D. M. Villeneuve, and P. B. Corkum. Alignment Dependent Enhancement of the Photoelectron Cutoff for Multiphoton Ionization of Molecules. *Phys. Rev. Lett.*, 112 (25), **2014**, 253001. DOI: 10.1103/PhysRevLett.112.253001 (cited on page 32).
- [73] S. K. Lee, Y. F. Lin, L. Yan, and W. Li. Laser-induced low energy electron diffraction in aligned molecules. *J. Phys. Chem. A*, 116 (8), **2012**, 1950. DOI: 10.1021/jp210798c (cited on page 32).
- [74] J. Mauritsson, T. Remetter, M. Swoboda, K. Klünder, A. L’Huillier, K. J. Schafer, O. Ghafur, F. Kelkensberg, W. Siu, P. Johnsson, M. J. J. Vrakking, I. Znakovskaya, T. Uphues, S. Zherebtsov, M. Kling, F. Lépine, E. Benedetti, F. Ferrari, G. Sansone, and M. Nisoli. Attosecond Electron Spectroscopy Using a Novel Interferometric Pump-Probe Technique. *Phys. Rev. Lett.*, 105, **2010**, 053001. DOI: 10.1103/PhysRevLett.105.053001 (cited on page 32).
- [75] M. Meckel, A. Staudte, S. Patchkovskii, D. M. Villeneuve, P. B. Corkum, R. Dörner, and M. Spanner. Signatures of the continuum electron phase in molecular strong-field photoelectron holography. *Nature Phys.*, 10 (8), **2014**, 594. DOI: 10.1038/nphys3010 (cited on page 32).

- [76] G. Sansone, F. Kelkensberg, J. F. Pérez-Torres, F. Morales, M. F. Kling, W. Siu, O. Ghafur, P. Johnsson, M. Swoboda, E. Benedetti, F. Ferrari, F. Lépine, J. L. Sanz-Vicario, S. Zherebtsov, I. Znakovskaya, A. L’Huillier, M. Y. Ivanov, M. Nisoli, F. Martín, and M. J. J. Vrakking. Electron localization following attosecond molecular photoionization. *Nature*, 465 (7299), **2010**, 763–766. DOI: 10.1038/nature09084 (cited on page 32).
- [77] A. Gazibegović-Busuladžić, E. Hasović, M. Busuladžić, D. Milošević, F. Kelkensberg, W. Siu, M. Vrakking, F. Lépine, G. Sansone, M. Nisoli, I. Znakovskaya, and M. Kling. Above-threshold ionization of diatomic molecules by few-cycle laser pulses. *Phys. Rev. A*, 84 (4), **2011**, 1–8. DOI: 10.1103/PhysRevA.84.043426 (cited on page 32).
- [78] W. Becker, A. Lohr, and M. Kleber. Effects of rescattering on above-threshold ionization. *J. Phys. B*, 27, **1994**, L325–L332. DOI: 10.1088/0953-4075/27/14/005 (cited on page 32).
- [79] D. Milošević and F. Ehlotzky. Coulomb and rescattering effects in above-threshold ionization. *Phys. Rev. A*, 58 (4), **1998**, 3124. DOI: 10.1103/PhysRevA.58.3124 (cited on page 32).
- [80] G. G. Paulus, F. Grasbon, H. Walther, R. Kopold, and W. Becker. Identification and Application of Quantum Trajectories in Above-Threshold Ionization. *Laser Phys.*, 12 (2), **2002**, 262–267. URL: http://www.maik.ru/full/lasphys_archive/02/2/lasphys2_02p262full.pdf (cited on page 32).
- [81] P. Salières, B. Carré, L. Le Déroff, F. Grasbon, G. G. Paulus, H. Walther, R. Kopold, W. Becker, D. B. Milosević, A. Sanpera, and M. Lewenstein. Feynman’s path-integral approach for intense-laser-atom interactions. *Science*, 292, **2001**, 902–5. DOI: 10.1126/science.108836 (cited on page 32).
- [82] G. Andriukaitis, T. Balciunas, S. Alisauskas, A. Pugzlys, A. Baltuska, T. Popmintchev, M.-C. Chen, M. M. Murnane, and H. C. Kapteyn. 90 GW peak power few-cycle mid-infrared pulses from an optical parametric amplifier. *Opt. Lett.*, 36 (15), **2011**, 2755–2757. DOI: 10.1364/OL.36.002755 (cited on page 32).
- [83] T. Morishita, A.-T. Le, Z. Chen, and C. D. Lin. Accurate Retrieval of Structural Information from Laser-Induced Photoelectron and High-Order Harmonic Spectra by Few-Cycle Laser Pulses. *Phys. Rev. Lett.*, 100, **2008**, 013903. DOI: 10.1103/PhysRevLett.100.013903 (cited on page 32).
- [84] Y. Wu, H. Ye, and J. Zhang. Extracting the information of scattering potential using angular distributions of rescattered photoelectrons. *Phys. Rev. A*, 84 (4), **2011**, 043418. DOI: 10.1103/PhysRevA.84.043418 (cited on page 32).
- [85] Y. Huismans, A. Rouzée, A. Gijsbertsen, J. H. Jungmann, A. S. Smolkowska, P. S. W. M. Logman, F. Lépine, C. Cauchy, S. Zamith, T. Marchenko, J. M. Bakker, G. Berden, B. Redlich, A. F. G. van der Meer, H. G. Muller, W. Vermin, K. J. Schafer, M. Spanner, M. Y. Ivanov, O. Smirnova, D. Bauer, S. V. Popruzhenko, and M. J. J. Vrakking. Time-resolved holography with photoelectrons. *Science*, 331 (6013), **2011**, 61. DOI: 10.1126/science.1198450 (cited on pages 32, 35, 38, 73, 83).

- [86] C. I. Blaga, F. Catoire, P. Colosimo, G. G. Paulus, H. G. Muller, P. Agostini, and L. F. DiMauro. Strong-field photoionization revisited. *Nature Phys.*, 5 (5), **2009**, 335–338. DOI: 10.1038/nphys1228 (cited on pages 33, 42, 73, 79).
- [87] F. H. M. Faisal. Strong-field physics: Ionization surprise. *Nature Phys.*, 5 (5), **2009**, 319–320. DOI: 10.1038/nphys1264 (cited on pages 33, 42).
- [88] C. Liu and K. Z. Hatsagortsyan. Origin of Unexpected Low Energy Structure in Photoelectron Spectra Induced by Midinfrared Strong Laser Fields. *Phys. Rev. Lett.*, 105, **2010**, 113003. DOI: 10.1103/PhysRevLett.105.113003 (cited on page 33).
- [89] C. Liu and K. Z. Hatsagortsyan. Wavelength and intensity dependence of multiple forward scattering of electrons at above-threshold ionization in mid-infrared strong laser fields. *J. Phys. B*, 44, **2011**, 095402. DOI: 10.1088/0953-4075/44/9/095402 (cited on page 33).
- [90] T.-M. Yan, S. Popruzhenko, M. J. J. Vrakking, and D. Bauer. Low-Energy Structures in Strong Field Ionization Revealed by Quantum Orbits. *Phys. Rev. Lett.*, 105, **2010**, 253002. DOI: 10.1103/PhysRevLett.105.253002 (cited on page 33).
- [91] M. Y. Kuchiev. Atomic antenna. *JETP Lett.*, 45 (7), **1987**, 404–406. URL: http://www.jetpletters.ac.ru/ps/1240/article__18763.pdf (cited on page 33).
- [92] K. C. Kulander, K. J. Schafer, and J. L. Krause. Super-intense laser-atom physics. In: **Vol. 316 NATO Adv. Sci. Inst. Series**. Ed. by J. Piraux, A. L’Huillier, and K. Rzazewski. New York: Plenum Press, 1993, pp. 95–110 (cited on pages 33, 36).
- [93] M. Lewenstein, P. Balcou, M. Y. Ivanov, A. L’Huillier, and P. B. Corkum. Theory of high-harmonic generation by low-frequency laser fields. *Phys. Rev. A*, 49 (3), **1994**, 2117–2132. DOI: 10.1103/PhysRevA.49.2117 (cited on pages 33, 38).
- [94] D. G. Arbó, S. Yoshida, E. Persson, K. Dimitriou, and J. Burgdörfer. Interference Oscillations in the Angular Distribution of Laser-Ionized Electrons near Ionization Threshold. *Phys. Rev. Lett.*, 96, **2006**, 143003. DOI: 10.1103/PhysRevLett.96.143003 (cited on page 35).
- [95] T Marchenko, H. G. Muller, K. J. Schafer, and M. J. J. Vrakking. Electron angular distributions in near-threshold atomic ionization. *J. Phys. B*, 43 (9), **2010**, 095601. DOI: 10.1088/0953-4075/43/9/095601 (cited on page 35).
- [96] A. Rudenko, K. Zrost, C. D. Schröter, V. L. B. de Jesus, B. Feuerstein, R. Moshhammer, and J. Ullrich. Resonant structures in the low-energy electron continuum for single ionization of atoms in the tunnelling regime. *J. Phys. B*, 37 (24), **2004**, L407–L413. DOI: 10.1088/0953-4075/37/24/L03 (cited on page 35).
- [97] Z. Chang, A. Rundquist, H. Wang, I. Christov, H. C. Kapteyn, and M. M. Murnane. Temporal phase control of soft-x-ray harmonic emission. *Phys. Rev. A*, 58 (1), **1998**, R30–R33. DOI: 10.1103/PhysRevA.58.R30 (cited on pages 36, 38).
- [98] G. G. Paulus, W. Nicklich, H. Xu, P. Lambropoulos, and H. Walther. Plateau in Above Threshold Ionization Spectra. *Phys. Rev. Lett.*, 72 (18), **1994**, 2851–2855. DOI: 10.1103/PhysRevLett.72.2851 (cited on page 36).

- [99] B. Yang, K. J. Schafer, B. Walker, K. C. Kulander, P. Agostini, and L. F. DiMauro. Intensity-Dependent Scattering Rings in High Order Above-Threshold Ionization. *Phys. Rev. Lett.*, 71 (23), **1993**, 3370–4. DOI: 10.1103/PhysRevLett.71.3770 (cited on page 36).
- [100] C. Lemell, K. Dimitriou, X.-M. Tong, S. Nagele, D. Kartashov, J. Burgdörfer, and S. Gräfe. Low-energy peak structure in strong-field ionization by midinfrared laser pulses: Two-dimensional focusing by the atomic potential. *Phys. Rev. A*, 85 (1), **2012**, 011403(R). DOI: 10.1103/PhysRevA.85.011403 (cited on page 43).
- [101] P. P. Pronko, S. K. Dutta, J. Squier, and J. V. Rudd. Machining of sub-micron holes using a femtosecond laser at 800 nm. *Optics Comm.*, 114, **1995**, 106–110. DOI: 10.1016/0030-4018(94)00585-I (cited on page 46).
- [102] V. Amendola and M. Meneghetti. Laser ablation synthesis in solution and size manipulation of noble metal nanoparticles. *Phys. Chem. Chem. Phys.*, 11 (20), **2009**, 3805. DOI: 10.1039/b900654k (cited on page 47).
- [103] S. P. Hatchett, C. G. Brown, T. E. Cowan, E. A. Henry, J. S. Johnson, M. H. Key, J. A. Koch, A. B. Langdon, B. F. Lasinski, R. W. Lee, A. J. Mackinnon, D. M. Pennington, M. D. Perry, T. W. Phillips, M. Roth, T. C. Sangster, M. S. Singh, R. A. Snavely, M. A. Stoyer, S. C. Wilks, and K. Yasuike. Electron, photon, and ion beams from the relativistic interaction of Petawatt laser pulses with solid targets. *Phys. Plasmas*, 7 (5), **2000**, 2076–2082. DOI: 10.1063/1.874030 (cited on page 47).
- [104] R. Lachaine, E. Boulais, and M. Meunier. From Thermo- to Plasma-Mediated Ultrafast Laser-Induced Plasmonic Nanobubbles. *ACS Phot.*, 1 (4), **2014**, 331–336. DOI: 10.1021/ph400018s (cited on page 47).
- [105] V. Pustovalov, A. Smetannikov, and V. Zharov. Photothermal and accompanied phenomena of selective nanophotothermolysis with gold nanoparticles and laser pulses. *Laser Phys. Lett.*, 5 (11), **2008**, 775–792. DOI: 10.1002/lapl.200810072 (cited on page 47).
- [106] E. A. Peralta, K. Soong, R. J. England, E. R. Colby, Z. Wu, B. Montazeri, C. McGuinness, J. McNeur, K. J. Leedle, D. Walz, E. B. Sozer, B. Cowan, B. Schwartz, G. Travish, and R. L. Byer. Demonstration of electron acceleration in a laser-driven dielectric microstructure. *Nature*, 503, **2013**, 91–94. DOI: 10.1038/nature12664 (cited on page 47).
- [107] C. B. Schaffer, A. Brodeur, J. F. García, and E. Mazur. Micromachining bulk glass by use of femtosecond laser pulses with nanojoule energy. *Opt. Lett.*, 26 (2), **2001**, 93–5. DOI: 10.1364/OL.26.000093 (cited on page 47).
- [108] M. Durach, A. Rusina, M. F. Kling, and M. I. Stockman. Predicted Ultrafast Dynamic Metallization of Dielectric Nanofilms by Strong Single-Cycle Optical Fields. *Phys. Rev. Lett.*, 107 (8), **2011**, 086602. DOI: 10.1103/PhysRevLett.107.086602 (cited on pages 47, 51).
- [109] M. M. Murnane, H. C. Kapteyn, S. P. Gordon, J. Bokor, E. N. Glytsis, and R. W. Falcone. Efficient coupling of high-intensity subpicosecond laser pulses into solids. *Appl. Phys. Lett.*, 62 (10), **1993**, 1068–1070. DOI: 10.1063/1.108797 (cited on page 48).

- [110] K. R. Wilson, S. Zou, J. Shu, E. Ru, S. R. Leone, G. C. Schatz, and M. Ahmed. Size-Dependent Angular Distributions of Low-Energy Photoelectrons Emitted from NaCl Nanoparticles. *Nano Lett.*, 7 (7), **2007**, 2014–2019. DOI: 10.1021/nl070834g (cited on page 50).
- [111] X. Zhang, K. A. Smith, D. R. Worsnop, J. L. Jimenez, J. T. Jayne, C. E. Kolb, J. Morris, and P. Davidovits. Numerical Characterization of Particle Beam Collimation: Part II Integrated Aerodynamic-Lens/Nozzle System. *Aerosol Sci. and Tech.*, 38 (6), **2004**, 619–638. DOI: 10.1080/02786820490479833 (cited on pages 50, 90).
- [112] A. Zelenyuk, Y. Cai, and D. Imre. From Agglomerates of Spheres to Irregularly Shaped Particles: Determination of Dynamic Shape Factors from Measurements of Mobility and Vacuum Aerodynamic Diameters. *Aerosol Sci. and Tech.*, 40 (3), **2006**, 197–217. DOI: 10.1080/02786820500529406 (cited on page 52).
- [113] T. M. Antonsen, T. Taguchi, A. Gupta, J. Palastro, and H. M. Milchberg. Resonant heating of a cluster plasma by intense laser light. *Phys. Plasmas*, 12, **2005**, 056703. DOI: 10.1063/1.1869500 (cited on pages 53, 65).
- [114] T. Döppner, J. P. Müller, A. Przystawik, S. Göde, J. Tiggesbäumker, K.-H. Meiwes-Broer, C. Varin, L. Ramunno, T. Brabec, and T. Fennel. Steplike Intensity Threshold Behavior of Extreme Ionization in Laser-Driven Xenon Clusters. *Phys. Rev. Lett.*, 105, **2010**, 053401. DOI: 10.1103/PhysRevLett.105.053401 (cited on pages 53, 64–66, 100, 105).
- [115] M. Lezius and S. Dobosz. Hot nanoplasmas from intense laser irradiation of argon clusters. *J. Phys. B*, 30, **1997**, L251–L258. DOI: 10.1088/0953-4075/30/7/003 (cited on pages 53, 65).
- [116] W. L. Barnes, A. Dereux, and T. W. Ebbesen. Surface plasmon subwavelength optics. *Nature*, 424, **2003**, 824–830. DOI: 10.1038/nature01937 (cited on pages 58, 59).
- [117] Z. Chen, A. Tafflove, and V. Backman. Photonic nanojet enhancement of backscattering of light by nanoparticles: a potential novel visible-light ultramicroscopy technique. *Opt. Express*, 12 (7), **2004**, 1214–20. DOI: 10.1364/OPEX.12.001214 (cited on page 58).
- [118] P. Ferrand, A. Devilez, M. Pianta, B. Stout, N. Bonod, E. Popov, and H. Rigneault. Direct imaging of photonic nanojets. *Opt. Express*, 16 (10), **2008**, 209–215. DOI: 10.1364/OE.16.006930 (cited on page 58).
- [119] H. Guo, Y. Han, X. Weng, Y. Zhao, G. Sui, Y. Wang, and S. Zhuang. Near-field focusing of the dielectric microsphere with wavelength scale radius. *Opt. Express*, 21 (2), **2013**, 2434–43. DOI: 10.1364/OE.21.002434 (cited on page 58).
- [120] D. Ju, H. Pei, Y. Jiang, and X. Sun. Controllable and enhanced nanojet effects excited by surface plasmon polariton. *Appl. Phys. Lett.*, 102 (17), **2013**, 171109. DOI: 10.1063/1.4802958 (cited on page 58).
- [121] E. J. Blackie, E. C. Le Ru, and P. G. Etchegoin. Single-molecule surface-enhanced Raman spectroscopy of nonresonant molecules. *J. Am. Chem. Soc.*, 131 (40), **2009**, 14466–14472. DOI: 10.1021/ja905319w (cited on page 59).

- [122] P. Das, T. K. Chini, and J. Pond. Probing Higher Order Surface Plasmon Modes on Individual Truncated Tetrahedral Gold Nanoparticle Using Cathodoluminescence Imaging and Spectroscopy Combined with FDTD Simulations. *J. Phys. Chem. C*, 116 (29), **2012**, 15610–15619. DOI: 10.1021/jp3047533 (cited on page 59).
- [123] A. Grubisic, E. Ringe, C. M. Cobley, Y. Xia, L. D. Marks, R. P. Van Duyne, and D. J. Nesbitt. Plasmonic near-electric field enhancement effects in ultrafast photoelectron emission: correlated spatial and laser polarization microscopy studies of individual Ag nanocubes. *Nano Lett.*, 12 (9), **2012**, 4823–4829. DOI: 10.1021/nl302271u (cited on page 59).
- [124] B. Lahiri, G. Holland, V. Aksyuk, and A. Centrone. Nanoscale imaging of plasmonic hot spots and dark modes with the photothermal-induced resonance technique. *Nano Lett.*, 13 (7), **2013**, 3218–24. DOI: 10.1021/nl401284m (cited on page 60).
- [125] F. Peano, J. L. Martins, R. A. Fonseca, L. O. Silva, G. Coppa, F. Peinetti, and R. Mulas. Dynamics and control of the expansion of finite-size plasmas produced in ultraintense laser-matter interactions. *Phys. Plasmas*, 14 (5), **2007**, 056704. DOI: 10.1063/1.2436855 (cited on pages 63, 105).
- [126] T. Ditmire, T. Donnelly, A. M. Rubenchik, R. W. Falcone, and M. D. Perry. Interaction of intense laser pulses with atomic clusters. *Phys. Rev. A*, 53 (5), **1996**, 3379–3402. DOI: 10.1103/PhysRevA.53.3379 (cited on pages 64, 65, 67, 68).
- [127] S. Zherebtsov, T. Fennel, J. Plenge, E. Antonsson, I. Znakovskaya, A. Wirth, O. Herrwerth, F. Süßmann, C. Peltz, I. Ahmad, S. A. Trushin, V. Pervak, S. Karsch, M. J. J. Vrakking, B. Langer, C. Graf, M. I. Stockman, F. Krausz, E. Rühl, and M. F. Kling. Controlled near-field enhanced electron acceleration from dielectric nanospheres with intense few-cycle laser fields. *Nature Phys.*, 7 (8), **2011**, 656–662. DOI: 10.1038/nphys1983 (cited on page 64).
- [128] T. Döppner, T. Fennel, T. Diederich, J. Tiggesbäumker, and K. H. Meiwes-Broer. Controlling the Coulomb Explosion of Silver Clusters by Femtosecond Dual-Pulse Laser Excitation. *Phys. Rev. Lett.*, 94 (1), **2005**, 013401. DOI: 10.1103/PhysRevLett.94.013401 (cited on pages 64, 67, 105).
- [129] J. Dawson and C. Oberman. High-Frequency Conductivity and the Emission and Absorption Coefficients of a Fully Ionized Plasma. *Phys. Fluids*, 5 (5), **1962**, 517–524. DOI: 10.1063/1.1706652 (cited on page 66).
- [130] D. S. Gross, M. E. Gälli, P. J. Silva, and K. A. Prather. Relative sensitivity factors for alkali metal and ammonium cations in single-particle aerosol time-of-flight mass spectra. *Anal. Chem.*, 72, **2000**, 416–22. DOI: 10.1021/ac990434g (cited on page 67).
- [131] T. Döppner, T. Fennel, P. Radcliffe, J. Tiggesbäumker, and K.-H. Meiwes-Broer. Ion and electron emission from silver nanoparticles in intense laser fields. *Phys. Rev. A*, 73, **2006**, 031202(R). DOI: 10.1103/PhysRevA.73.031202 (cited on page 67).
- [132] A. Kawabata and R. Kubo. Electronic properties of fine metal particles II. Plasma resonance absorption. *J. Phys. Soc. Jpn.*, 21 (9), **1966**, 1765–1772. DOI: 10.1143/JPSJ.21.1765 (cited on page 68).

- [133] M. M. Marinak, G. D. Kerbel, N. A. Gentile, O. Jones, D. Munro, S. Pollaine, T. R. Dittrich, and S. W. Haan. Three-dimensional HYDRA simulations of National Ignition Facility targets. *Phys. Plasmas*, 8 (5), **2001**, 2275. DOI: 10.1063/1.1356740 (cited on pages 69, 70, 102, 103).
- [134] A. Heidenreich, J. Jortner, and I. Last. Cluster dynamics transcending chemical dynamics toward nuclear fusion. *Proc. Natl. Acad. Sci.*, 103 (28), **2006**, 10589–10593. DOI: 10.1073/pnas.0508622103 (cited on pages 69, 71, 105).
- [135] E. Waxman and D. Shvarts. Second-type self-similar solutions to the strong explosion problem. *Phys. Fluids A*, 5 (4), **1993**, 1035–1046. DOI: 10.1063/1.858668 (cited on page 71).
- [136] Y. B. Zel’dovich and Y. P. Raizer. **Physics of shock waves and high-temperature hydrodynamic phenomena**. Ed. by W. D. Hayes and R. F. Probstein. New York, NY, USA: Dover, 2002 (cited on page 71).
- [137] R. Teyssier, D. Ryutov, and B. Remington. Accelerating shock waves in a laser-produced density gradient. *Astrophys. J.*, 127, **2000**, 503–508. DOI: 10.1086/313338 (cited on page 71).
- [138] Y. Huismans, A. Gijsbertsen, A. Smolkowska, J. Jungmann, A. Rouzée, P. Logman, F. Lépine, C. Cauchy, S. Zamith, T. Marchenko, J. Bakker, G. Berden, B. Redlich, A. van der Meer, M. Ivanov, T.-M. Yan, D. Bauer, O. Smirnova, and M. Vrakking. Scaling Laws for Photoelectron Holography in the Midinfrared Wavelength Regime. *Phys. Rev. Lett.*, 109 (1), **2012**, 1–5. DOI: 10.1103/PhysRevLett.109.013002 (cited on page 73).
- [139] M. Gerrity, S. Brown, T. Popmintchev, M. M. Murnane, H. C. Kapteyn, and S. Backus. High Repetition Rate, mJ-Level, mid-IR OPCPA System. *CLEO: Science and Innovations*, **2014**, STh4E.8. DOI: 10.1364/CLEO_SI.2014.STh4E.8 (cited on page 73).
- [140] A. Fleischer, O. Kfir, T. Diskin, P. Sidorenko, and O. Cohen. Spin angular momentum and tunable polarization in high-harmonic generation. *Nature Phot.*, 8 (7), **2014**, 543–549. DOI: 10.1038/nphoton.2014.108 (cited on page 73).
- [141] O. Kfir, P. Grychtol, E. Turgut, R. Knut, D. Zusin, D. Popmintchev, T. Popmintchev, H. Nembach, J. Shaw, A. Fleischer, H. Kapteyn, M. Murnane, and O. Cohen. Generation of bright circularly-polarized extreme ultraviolet high harmonics for magnetic circular dichroism spectroscopy. *Arxiv preprint arXiv:1401.4101*, **2014**, 12. URL: <http://arxiv.org/abs/1401.4101>. arXiv: 1401.4101 (cited on page 73).
- [142] M. Ivanov and E. Pisanty. High-harmonic generation: Taking control of polarization. *Nature Phot.*, 8 (7), **2014**, 501–503. DOI: 10.1038/nphoton.2014.141 (cited on page 73).
- [143] W. Becker and D. B. Milos. Attosecond pulse trains with unusual nonlinear polarization. *Phys. Rev. A*, 62, **2000**, 011403(R). DOI: 10.1103/PhysRevA.62.011403 (cited on page 73).
- [144] W. Becker, R. Kopold, and D. B. Milos. Generation of circularly polarized high-order harmonics by two-color coplanar field mixing. *Phys. Rev. A*, 61, **2000**, 0. DOI: 10.1103/PhysRevA.61.063403 (cited on page 73).

- [145] M. G. Pullen, J. Dura, B. Wolter, M. Baudisch, M. Hemmer, N. Camus, A. Senftleben, C. D. Schroeter, R. Moshhammer, J. Ullrich, and J. Biegert. Kinematically complete measurements of strong field ionization with mid-IR pulses. *J. Phys. B*, 47 (20), **2014**, 204010. DOI: 10.1088/0953-4075/47/20/204010 (cited on page 74).
- [146] W. Becker, S. P. Goreslavski, D. B. Milošević, and G. G. Paulus. Low-energy electron rescattering in laser-induced ionization. *J. Phys. B*, 47 (20), **2014**, 204022. DOI: 10.1088/0953-4075/47/20/204022 (cited on page 74).
- [147] Q. Li, X.-M. Tong, T. Morishita, C. Jin, H. Wei, and C. D. Lin. Rydberg states in the strong field ionization of hydrogen by 800, 1200 and 1600 nm lasers. *J. Phys. B*, 47 (20), **2014**, 204019. DOI: 10.1088/0953-4075/47/20/204019 (cited on page 74).
- [148] N. G. Kling, D. Paul, A. Gura, G. Laurent, S. De, H. Li, Z. Wang, B. Ahn, C. H. Kim, T. K. Kim, I. V. Litvinyuk, C. L. Cocke, I. Ben-Itzhak, D. Kim, and M. F. Kling. Thick-lens velocity-map imaging spectrometer with high resolution for high-energy charged particles. *I. Inst.*, 9 (05), **2014**, P05005–P05005. DOI: 10.1088/1748-0221/9/05/P05005 (cited on page 75).
- [149] C. Peltz, C. Varin, T. Brabec, and T. Fennel. Time-Resolved X-Ray Imaging of Anisotropic Nanoplasma Expansion. *Phys. Rev. Lett.*, 113, **2014**, 133401. DOI: 10.1103/PhysRevLett.113.133401 (cited on page 75).
- [150] H. Haberland. Thin films from energetic cluster impact: A feasibility study. *J. Vac. Sci. and Tech. A*, 10 (5), **1992**, 3266. DOI: 10.1116/1.577853 (cited on page 77).
- [151] J. Kousal, O. Polonskyi, O. Kylián, A. Choukourov, A. Atremenko, J. Pesicka, D. Slavinska, and H. Biederman. Characterization of nanoparticle flow produced by gas aggregation source. *Vacuum*, 96, **2013**, 32–38. URL: <http://www.sciencedirect.com/science/article/pii/S0042207X13000675> (cited on page 77).
- [152] X.-B. Bian, Y. Huismans, O. Smirnova, K.-J. Yuan, M. J. J. Vrakking, and A. Bandrauk. Subcycle interference dynamics of time-resolved photoelectron holography with midinfrared laser pulses. *Phys. Rev. A*, 84, **2011**, 043420. DOI: 10.1103/PhysRevA.84.043420 (cited on page 83).
- [153] **FDTD Solutions**. Lumerical Solutions, Inc. URL: <http://www.lumerical.com/tcad-products/fdtd/> (cited on page 91).
- [154] J. R. DeVore. Refractive Indices of Rutile and Sphalerite. *J. Opt. Soc. Am.*, 42 (6), **1951**, 416–419. DOI: 10.1364/JOSA.41.000416 (cited on page 91).
- [155] **Handbook of Optics, Vol. 4**. 3rd. McGraw-Hill, 2009 (cited on page 91).
- [156] A. Salabat and M. Alinoori. Viscosity, Density, and Refractive Index of Poly(vinylpyrrolidone) + 1-Propanol and + 2-Propanol at 298.15 K. *J. Chem. Eng. Data*, 54 (3), **2009**, 1073. DOI: 10.1021/je800670w (cited on page 91).
- [157] E. D. Palik. **Handbook of Optical Constants of Solids**. Boston: Academic Press, 1985 (cited on page 91).

- [158] B. Schütte, M. Arbeiter, T. Fennel, M. J. J. Vrakking, and A. Rouzée. Rare-Gas Clusters in Intense Extreme-Ultraviolet Pulses from a High-Order Harmonic Source. *Phys. Rev. Lett.*, 112 (7), **2014**, 073003. DOI: 10.1103/PhysRevLett.112.073003 (cited on page 92).
- [159] C. T. L. Smeenk, L. Arissian, B. Zhou, A. Mysyrowicz, D. M. Villeneuve, A. Staudte, and P. B. Corkum. Partitioning of the Linear Photon Momentum in Multiphoton Ionization. *Phys. Rev. Lett.*, 106, **2011**, 193002. DOI: 10.1103/PhysRevLett.106.193002 (cited on page 92).
- [160] A. D. McFarland and C. L. Haynes. Color my nanoworld. *J. Chem. Edu.*, 81 (4), **2004**, 544A–544B. DOI: 10.1021/ed081p544A (cited on page 92).
- [161] J. A. Huffman, J. T. Jayne, F. Drewnick, A. C. Aiken, T. Onasch, D. R. Worsnop, and J. L. Jimenez. Design, Modeling, Optimization, and Experimental Tests of a Particle Beam Width Probe for the Aerodyne Aerosol Mass Spectrometer. *Aerosol Sci. and Tech.*, 39, **2005**, 1143–1163. DOI: 10.1080/02786820500423782 (cited on page 97).
- [162] S. G. Lias, E. J. Bartmess, J. F. Liebman, J. L. Holmes, R. D. Levin, and W. G. Mallard. Ion Energetics Data. In: **NIST Chemistry WebBook, NIST Standard Reference Database Number 69**. Ed. by Linstrom P J and G. W. Mallard. National Institute of Standards and Technology, Gaithersburg MD, 20899. URL: <http://webbook.nist.gov> (cited on page 100).
- [163] G. P. Schurtz, P. D. Nicolai, and M. Busquet. A nonlocal electron conduction model for multidimensional radiation hydrodynamics codes. *Phys. Plasmas*, 7, **2000**, 4238. DOI: 10.1063/1.1289512 (cited on page 104).
- [164] J. D. Huba. NRL Plasma Formulary. *Office of Naval Research*, **2011**, 1–71. URL: <http://www.nrl.navy.mil/ppd/content/nrl-plasma-formulary> (cited on page 104).